

## ABSTRACT

Title of Thesis: SEPARATION OF AN ELLIPSOIDAL BODY  
FROM A TWO-DIMENSIONAL RAMP IN  
HYPERSONIC FLOW WITH KESTREL  
VALIDATION

Denikka Lynette Brent,  
Master of Science, 2022

Thesis Directed By: Associate Professor Stuart Laurence  
Department of Aerospace Engineering

This study investigated the separation dynamics of an ellipsoidal body shedding from a two-dimensional ramp using experimental and computational methods. The main objective was to assess the fidelity of computational simulations of a complex, interacting flow configuration via comparison with experimental data. Experimental data was generated by the HyperTERP shock tunnel at the University of Maryland. Ellipsoids were stationed on a  $10^\circ$  ramp with varying initial positions and were then exposed to Mach 6 flow, allowing them to fly freely in response to the aerodynamic forces experienced. Experimental results revealed three trajectory behaviors that were dependent upon the initial shock impingement location: expulsion to surfing, surfing, and direct entrainment. These behaviors were consistent with earlier sphere experiments, but the introduction of pitch resulted in somewhat more complex dynamics. Numerical simulations were performed with CREATE-AV Kestrel, the fixed-wing multiphysics tool developed by the Computational

Research and Engineering Acquisition Tools and Environments (CREATE) Program. Computational results exhibited discrepancies primarily in terms of the velocity and acceleration values when compared to the experimental results. The sensitivity of the initial conditions caused unsteadiness at the start of the solution, and potentially propagated errors in velocity and acceleration downstream. Despite these initial errors, however, the computational simulations showed a comparable trajectory to those of the experimental results.

SEPARATION OF AN ELLIPSOIDAL BODY FROM A TWO-DIMENSIONAL  
RAMP IN HYPERSONIC FLOW WITH KESTREL VALIDATION

by

Denikka Lynette Brent

Thesis submitted to the Faculty of the Graduate School of the  
University of Maryland, College Park, in partial fulfillment  
of the requirements for the degree of  
Master of Science  
2022

Advisory committee:  
Professor Stuart Laurence, Chair  
Professor Kenneth Yu  
Professor Christopher Cadou  
Dr. William Tyson

© Copyright by  
Denikka Lynette Brent  
2022

## Dedication

I'd like to dedicate this work to my Lord and Savior, Jesus Christ. Without You, I certainly could not have reached this point in my academic and professional career. All that I am is because of You.

*“Thou hast also given me the shield of thy salvation: and thy right hand hath holden me up, and thy gentleness hath made me great.”*

Psalm 18:35

## Acknowledgements

Firstly, I'd like to acknowledge my research advisor, Dr. Laurence. Your patience, understanding and willingness to educate has certainly aided in my growth as an engineer. I enjoyed our technical discussions and look forward to many more. Many thanks to Dr. Wenbo Zhu and my fellow researchers for your input and ideas that helped complete this work. I'd also like to acknowledge my professional advisors Dr. William Tyson and Mr. Jacob Allen for your guidance in completing the computational simulations. Thank you for your patience as I was introduced to the intricate details of the modeling world. Thank you to the other two members of my advisory committee, Dr. Yu and Dr. Cadou.

I'd like to thank the NAVAIR NISE program for providing the opportunity and resources to complete this work. Thank you for trusting me to provide solutions to the Department of Defense. Thank you to my supervisor Chandira McNeill and fellow coworkers for your encouragement and push. You all truly understood the mental pressure that comes with a body of work such as this. You all assured me every time that although the work is challenging, it is not impossible.

I would like to thank all my family and friends who prayed, encouraged, uplifted, and motivated me as I strove toward completing this work. Finally, thank you to my mother and father, Medina and David Brent for instilling in me ambition, reminding me to never settle for less, and to reach past any limitation society places on an African American female.

# Table of Contents

Dedication .....	ii
Acknowledgements .....	vi
Table of Contents .....	iv
List of Tables .....	vi
List of Figures.....	vii
List of Abbreviations .....	xiv
Chapter 1: Introduction .....	1
1.1 Motivation and Background.....	1
1.2.1 Shock-Wave Surfing .....	3
1.2.2 Review of the Previous Study: Dynamics of a spherical body shedding from a hypersonic ramp .....	5
1.3 Scope and Outline .....	8
Chapter 2: Experimental Methods .....	10
2.1 Experimental Approach.....	10
2.1.1 HyperTERP .....	10
2.1.2 Shadowgraph Imaging .....	12
2.1.3 Test Articles .....	13
2.2 Optical Tracking Routine .....	15
2.2.1 Image Edge Point Detection .....	15
2.2.2 CAD model of ellipsoid .....	17
2.2.3 Silhouette Generation .....	19
2.2.4 Error Characterization and Iteration Scheme.....	21
Chapter 3: Computational Methods .....	26
3.1 Computational Approach .....	26
3.1.1 Grid Generation .....	27
3.1.2 Kestrel: Hypersonic Flow Solver .....	30
Chapter 4: Experimental Results .....	35
4.1 Experimental Variables .....	35
4.1.1 Ellipsoid Geometry.....	35
4.1.2 Initial Configuration .....	37
4.2 Ellipsoid Trajectories.....	38
4.3 Ellipsoid Dynamics.....	46
Chapter 5: Computational Results .....	51
5.1 Computational Parameters .....	51
5.1.1 Grid Refinement Study .....	52
5.1.2 Sensitivity Analysis.....	57
5.2 Kestrel Comparison .....	59
5.2.1 Physical Data Validation.....	59
Chapter 6: Summary and Conclusion .....	66
6.1 Summary and Conclusions.....	66

6.1.1 Summary of Experimental Results .....	66
6.1.2 Summary of Computational Results .....	67
6.2 Academic and Technical Contributions .....	70
6.3 Recommendation for Future Work .....	70
Appendices .....	72
A1: Shadowgraph images of Ellipsoids Trajectories .....	72
A2: Displacement Analysis of Experimental Results .....	79
A3: Hadamard Regularization Analysis of Velocity and Acceleration .....	86
A4: Dynamics Results of Various Grid Level Refinement .....	93
A5: Calculation of normalization variable $\mathbf{r}$ .....	99
Bibliography .....	100

## List of Tables

<b>Table 2.1:</b> HyperTERP freestream conditions .....	12
<b>Table 3.1:</b> Initial global sizing for computational grids. All unit lengths are in meters .....	28
<b>Table 3.2:</b> Comparison of the computational and experimental freestream conditions .....	33
<b>Table 4.1:</b> Dimensional Matrix of the Ellipsoids .....	35
<b>Table 4.2:</b> Ellipsoids studied with optical tracking routine and their corresponding configurations .....	36
<b>Table 4.3:</b> Experimental results of ellipsoid initial position and corresponding shock impingements .....	38
<b>Table 4.4:</b> Trajectory behaviors exhibited by each shot .....	40
<b>Table 5.1:</b> Cell count of the Cartesian overset for each grid level in the refinement study .....	53
<b>Table 5.2:</b> Total faces on the unstructured grids for each grid level in the refinement study .....	53
<b>Table 5.3:</b> Total volume cells on the unstructured grids for each grid level in the refinement study .....	54
<b>Table 5.4:</b> Total faces and cells for the extra coarse grid .....	57
<b>Table 5.5:</b> Computational domain sizing for the medium Grid .....	59

## List of Figures

<b>Figure 1.1:</b> (Left) The Columbia just before the detached foam impacted the leading edge. Right: Moments just after the detached foam impacted the leading edge (picture courtesy of CBS news).....	2
<b>Figure 1.2:</b> (Left) Ratio of lift to drag for sphere/oblique shock interactions, with wedge angles of 5, 10, 20, and 30° (dark to light). The horizontal dashed line for each shade indicates the tangent of the corresponding shock angle. (Right) The maximum L/D value versus the tangent of the shock angle for Mach numbers of (dark through light) 6, 8, 10, and 25. The dashed line corresponds to $(LD)_{max} = \tan\beta$ [31].....	5
<b>Figure 1.3:</b> Shadowgraph images of the 9.53-mm sphere as it travelled downstream the ramp-generated shock [6] .....	6
<b>Figure 1.4:</b> Numerical visualizations from the viscous sphere/boundary-layer simulations: (top) 6-mm diameter sphere and (bottom) 8-mm diameter sphere [6] .....	7
<b>Figure 2.1:</b> HyperTERP located at the University of Maryland. ....	11
<b>Figure 2.2:</b> Schematic of shock tunnel used to perform the experimental testing .....	11
<b>Figure 2.3:</b> A shadowgraph of a single frame recorded during experimental testing. ....	13
<b>Figure 2.4:</b> Schematic of the prolate ellipsoids (top). Schematic of oblate ellipsoids (bottom). ....	14
<b>Figure 2.5:</b> Edges detected without subpixel localization correction (left). Edges detected with subpixel localization correction (right). ....	16
<b>Figure 2.6:</b> Binary image of edge points traced in pixel space (left). Traced edge points projected in image space to verify edge points detection (right) .....	17
<b>Figure 2.7:</b> (Left) RMS convergence of pose parameter with poor initial guess. (Right) RMS derivative magnitude of pose parameter. ....	25
<b>Figure 3.1</b> XZ plane view of ellipsoid (top left) and ramp (bottom left) grid with cut plane view of the untrimmed volumetric boundary layer. Orthogonal view of ellipsoid (top right) and ramp (bottom right) grid. ....	30
<b>Figure 3.2:</b> Trimmed no slip boundary condition of the ellipsoid (left) and ramp (right) with a trim distance of .0015 m and .005 m, respectively. ....	33
<b>Figure 4.2:</b> Shock-wave surfing trajectory (left 3 images). Expulsion to surfing (center 3 images). Direct entrainment (right 3 images) .....	40
<b>Figure 4.3:</b> Comparable trajectories with similar shock impingements .....	41
<b>Figure 4.4:</b> Experimental shadowgraph images of Configuration E2 (left) and Configuration E1 (right) .....	42
<b>Figure 4.5:</b> 3.18 mm spherical trajectories from previous study (top left). Comparison of all ellipsoidal trajectories (top right). Trajectories of ellipsoids with Configuration D (bottom left) and E (bottom right).....	43
<b>Figure 4.6:</b> Normalized distance from shock center for Configuration D (Top Left) and E (Top Right). Pitch values of Configuration D (Bottom Left) and E (Bottom Right) .....	44

<b>Figure 4.7:</b> Shock surfing of an ellipsoid (left) and spherical (right) body .....	45
<b>Figure 4.8:</b> Horizontal displacement values derived from the optical tracking code of shots in Configuration D (left) and E (right) .....	47
<b>Figure 4.9:</b> Horizontal velocity of Configuration D (top left) and E (top right). Horizontal acceleration of Configuration D (bottom left) and E (bottom right) .....	48
<b>Figure 4.10:</b> Near-ramp boundary layer interaction on Configuration D4 ellipsoid ..	49
<b>Figure 4.11:</b> Comparison of convergence of velocity (Top) and acceleration (Bottom) values between E1 and E2 .....	50
<b>Figure 5.1:</b> Visualization of the ellipsoid and ramp positioned in simulation before release.....	52
<b>Figure 5.2:</b> Coarse (top), Medium (middle), and Fine (bottom) unstructured grids produced from grid refinement study.....	54
<b>Figure 5.3:</b> Orthogonal view of the starting position of the ellipsoid for the computational Fine grid .....	55
<b>Figure 5.4:</b> Comparison of coefficients of Lift (top) and Drag (bottom) between the Coarse, Medium, and Fine grid .....	56
<b>Figure 5.5:</b> Comparison of coefficients of Lift (top) and Drag (bottom) between with differing start-up iterations .....	58
<b>Figure 5.6:</b> (Left) Total domain view of Medium computational grid. (Right) Adaptive grid/mesh refinement around ramp generated shock. ....	59
<b>Figure 5.7:</b> XZ plane (left) and orthogonal view (right) of the initial shock impingement on the ellipsoid from the numerical simulation. ....	60
<b>Figure 5.8:</b> Flow visualization of the ramp generated shock and ellipsoid bow shock .....	61
<b>Figure 5.9:</b> Resulting trajectory from an initial shock impingement below the semi-major axis of the ellipsoid for the computational case (left images) and the experimental results for Configuration D3 (right images). ....	62
<b>Figure 5.10:</b> Displacement (left) and pitch (right) of the computational case compared to the ellipsoids of Configuration D. ....	63
<b>Figure 5.11:</b> Horizontal displacement (left) and Horizontal velocity (right) comparison of the numerical simulation and experimental results Configuration D ellipsoids. ....	64
<b>Figure 5.12:</b> Horizontal acceleration (left) and forces (right) comparison of the numerical simulation and experimental results Configuration D ellipsoids. ....	65
<b>Figure A1.1:</b> Shadowgraph images of Configuration D1 .....	72
<b>Figure A1.2:</b> Shadowgraph images of Configuration D2 .....	73
<b>Figure A1.3:</b> Shadowgraph images of Configuration D3 .....	74
<b>Figure A1.4:</b> Shadowgraph images of Configuration D4 .....	75
<b>Figure A1.5:</b> Shadowgraph images of Configuration E1 .....	76
<b>Figure A1.6:</b> Shadowgraph images of Configuration E2 .....	77
<b>Figure A1.7:</b> Shadowgraph images of Configuration E3 .....	78

<b>Figure A2.1:</b> Horizontal Displacement (top left), Vertical Displacement (top right) of Configuration D1. Absolute (bottom left) and relative (bottom right) x versus y displacement of Configuration D1. ....	79
<b>Figure A2.2:</b> Horizontal Displacement (top left), Vertical Displacement (top right) of Configuration D2. Absolute (bottom left) and relative (bottom right) x versus y displacement of Configuration D2. ....	80
<b>Figure A2.3:</b> Horizontal Displacement (top left), Vertical Displacement (top right) of Configuration D3. Absolute (bottom left) and relative (bottom right) x versus y displacement of Configuration D3. ....	81
<b>Figure A2.4:</b> Horizontal Displacement (top left), Vertical Displacement (top right) of Configuration D4. Absolute (bottom left) and relative (bottom right) x versus y displacement of Configuration D4. ....	82
<b>Figure A2.5:</b> Horizontal Displacement (top left), Vertical Displacement (top right) of Configuration E1. Absolute (bottom left) and relative (bottom right) x versus y displacement of Configuration E1. ....	83
<b>Figure A2.6:</b> Horizontal Displacement (top left), Vertical Displacement (top right) of Configuration E2. Absolute (bottom left) and relative (bottom right) x versus y displacement of Configuration E2. ....	84
<b>Figure A2.7:</b> Horizontal Displacement (top left), Vertical Displacement (top right) of Configuration E3. Absolute (bottom left) and relative (bottom right) x versus y displacement of Configuration E3. ....	85

<b>Figure A3.1:</b> Horizontal Velocity (top left) and Horizontal Acceleration (top right) derived from Hadamard Regularization methods for Configuration D1. Polynomial 6 Fit Curve of Velocity (bottom left) and Acceleration (bottom right) data derived from Hadamard Regularization methods for Configuration D1.....	86
<b>Figure A3.2:</b> Horizontal Velocity (top left) and Horizontal Acceleration (top right) derived from Hadamard Regularization methods for Configuration D2. Polynomial 6 Fit Curve of Velocity (bottom left) and Acceleration (bottom right) data derived from Hadamard Regularization methods for Configuration D2.....	87
<b>Figure A3.3:</b> Horizontal Velocity (top left) and Horizontal Acceleration (top right) derived from Hadamard Regularization methods for Configuration D3. Polynomial 6 Fit Curve of Velocity (bottom left) and Acceleration (bottom right) data derived from Hadamard Regularization methods for Configuration D3.....	88
<b>Figure A3.4:</b> Horizontal Velocity (top left) and Horizontal Acceleration (top right) derived from Hadamard Regularization methods for Configuration D4. Polynomial 6 Fit Curve of Velocity (bottom left) and Acceleration (bottom right) data derived from Hadamard Regularization methods for Configuration D4.....	89
<b>Figure A3.5:</b> Horizontal Velocity (top left) and Horizontal Acceleration (top right) derived from Hadamard Regularization methods for Configuration E1. Polynomial 6 Fit Curve of Velocity (bottom left) and Acceleration (bottom right) data derived from Hadamard Regularization methods for Configuration E1. ....	90
<b>Figure A3.6:</b> Horizontal Velocity (top left) and Horizontal Acceleration (top right) derived from Hadamard Regularization methods for Configuration E2. Polynomial 6	

Fit Curve of Velocity (bottom left) and Acceleration (bottom right) data derived from Hadamard Regularization methods for Configuration E2. ....91

**Figure A3.7:** Horizontal Velocity (top left) and Horizontal Acceleration (top right) derived from Hadamard Regularization methods for Configuration E3. Polynomial 6 Fit Curve of Velocity (bottom left) and Acceleration (bottom right) data derived from Hadamard Regularization methods for Configuration E3. ....92

**Figure A4.1:** Computational data for Extra Coarse grid with 72000 iterations and a timestep of 1E-07. Relative horizontal displacement (top left) and Relative vertical displacement (top right). X vs Z displacement (bottom left) and Pitch (bottom right). ....93

.....93

**Figure A4.2:** Computational data for Extra Coarse grid with 72000 iterations and a timestep of 1E-07. Horizontal velocity (top left) and horizontal acceleration (top right). Horizontal Forces (bottom left) and Moments magnitude (bottom right). ....94

**Figure A4.3:** Computational data for Coarse grid with 53809 iterations and a timestep of 1E-07. Relative horizontal displacement (top left) and Relative vertical displacement (top right). X vs Z displacement (bottom left) and Pitch (bottom right). ....95

.....95

**Figure A4.4:** Computational data for Coarse grid with 53809 iterations and a timestep of 1E-07. Horizontal velocity (top left) and horizontal acceleration (top right). Horizontal Forces (bottom left) and Moments magnitude (bottom right). ....96

**Figure A4.5:** Computational data for Medium grid with 123294 iterations and a timestep of 5E-08. Relative horizontal displacement (top left) and Relative vertical displacement (top right). X vs Z displacement (bottom left) and Pitch (bottom right). ....97

.....97

**Figure A4.6:** Computational data for Medium grid with 123294 iterations and a timestep of 5E-08. Horizontal velocity (top left) and horizontal acceleration (top right). Horizontal Forces (bottom left) and Moments magnitude (bottom right). ....98

## List of Abbreviations

### Acronyms

HyperTERP	Hypersonic Tunnel for Educational and Research Purposes
CREATE-AV	Computational Research and Engineering Acquisition Tools and Environments – Air Vehicle
DOF	Degrees of Freedom
STS	Space Transportation System
CPU	Central Processing Unit
CFD	Computational Fluid Dynamics
NBOB	Near-body, Off-body
NS	Navier-Stokes
NAVAIR	Naval Air Systems Command
DoD	Department of Defense
UMD	University of Maryland
HAPL	High-Speed Aerodynamics and Propulsion Laboratory
MATLAB	Matrix Laboratory
CAD	Computer Aided Drawing
RMS	Root Mean Square
STL	Stereolithography
KUI	Kestrel User Interface
CFL	Courant–Friedrichs–Lewy
WENO	Weighted Essentially Non-Oscillatory

## Variables and Symbols

$t$	Time (s)
$T$	Temperature (K)
$T_s$	Static Temperature (K)
$T_o$	Total Temperature (K)
$P$	Pressure (kPa, Pa)
$P_s$	Static Pressure (Pa)
$P_o$	Total Pressure (Pa)
$\rho$	Density (kg/m <sup>3</sup> )
$M$	Mach Number
$\circ$	Pitch Angle
$\gamma$	Pose parameter iteration step size
$Re$	Reynolds Number
$L_{max}$	Longest Length (m)
$L_{ref}$	Reference Length (m)
$\oint_S$	Surface Integral
$\iiint_V$	Volume Integral
$\hat{n}$	Unit normal vector
$e$	Energy
$\vec{f}$	Body force per unit mass
$\vec{F}_{viscous}$	Shear and normal viscous stresses
$\dot{W}_{viscous}$	Rate of work due to viscous forces
$\dot{q}$	Rate of heat addition
$C(x)$	Contour function
$x_c$	Camera position
$e_1, e_2$	Horizontal Axis, Vertical Axis
$I_a$	Optical Axis
$\hat{x}$	Transformation Variable
$N_u, N_v$	Horizontal coordinate, Vertical coordinate
$K_u, K_v$	Horizontal coordinate length, Vertical coordinate length
$r$	Pixel scale factor
$\mathbf{r}$	Incident light ray vector
$\mathbf{n}_i$	Triangle surface normal vector
$\mathbf{x}_{ep,i}$	$i$ 'th (of N) edge points
$\mathbf{x}_{s,i}$	is the nearest location on the reconstructed silhouette
$\mathbf{p}_n$	Pose parameter vector

# Chapter 1: Introduction

## 1.1 Motivation and Background

The many applications of high-speed separation problems motivates the continued study of the dynamics of high-speed interacting bodies. Examples of high-speed separation problems include separation of a store from a pylon on a military aircraft, a multistage rocket detaching a booster, and particulate matter detachment from the leading edge of a high-speed vehicle. Failed or unexpected separation events can cause system failure and may even lead to loss of life. The work presented in this study is motivated by the need to characterize and predict separation trajectories in the field of aerodynamics.

Aircraft structures operating in hypersonic flows are subjected to high thermal and fluid stresses [10]. When exposed to such an extreme environment, particulate matter can potentially shed from the air vehicle. Though the size of the particulate matter may seem insignificant compared to the aircraft, the high-speed at which it travels results in kinetic energy that can cause catastrophic impact downstream. This phenomenon was demonstrated during the flight of the Columbia shuttle on mission STS-107 on February 1, 2003. During ascent, a small piece of foam detached from the vehicle and separated into particulate matter. As the debris continued in free flight motion, it impacted the leading edge of the orbiter wing and damaged the heat shield. As a result, the spacecraft was not able to survive the extreme thermal environment upon reentry, resulting in the loss of the spacecraft and crew [7].

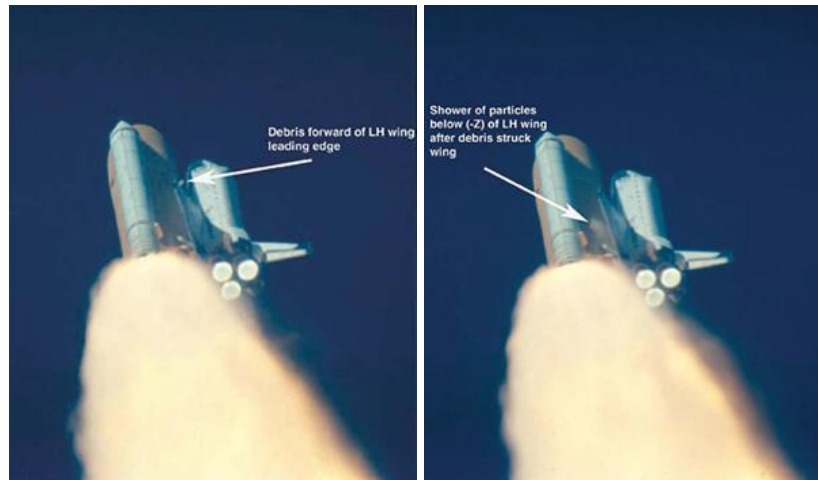


**Figure 1.1:** (Left) The Columbia just before the detached foam impacted the leading edge. Right: Moments just after the detached foam impacted the leading edge (picture courtesy of CBS news)

Another relevant phenomenon is a store separation event in which a component releases from a vehicle travelling at supersonic/hypersonic speed. The store separation phenomenon itself is not a new area of study. In fact, the prediction capability of store separation has greatly improved since the 1960s. In earlier days, the trajectories of store separation events were “hit or miss”, meaning, there was no established method to predict the motion of the store as it detached from the vehicle. In some cases, the store would impact the vehicle, ultimately destroying it [1]. Many of today’s research efforts are focused on improving the fidelity of the predictive capability of store separation tools for more complex flow problems, especially in defense applications. Complexities of store separation prediction capabilities have transitioned from simple cases such as a bomb launching from an open cockpit to an unmanned aerial vehicle releasing a missile in high-speed flight [1]. Prediction capability of store separation is especially an area of interest in defense applications.

Lastly, multistage rockets involve a variety of separation modes. These include heat shield separation, ullage rocket separation, stage separation, and spacecraft separation. In every instance, a successful separation event is critical to the mission. An example of a failed separation event was the multistage rocket used in the Soyuz Expedition 57 mission. Within minutes of launch, the vehicle aborted mid-flight due to a booster failure. Although no life was lost, substantial resources were wasted after one launch [10].

## 1.2 Literature Review

### 1.2.1 Shock-Wave Surfing

There have been many studies conducted evaluating separation between bodies travelling at supersonic and hypersonic speeds. This continues to be an area of interest due to the many applications related to this phenomenon. An important concept to emerge from these previous studies is that of shock-wave surfing. The concept of shock wave surfing states that as a body is in motion, it follows the shock wave generated by another body upstream [31]. Examples of an event in which shock wave surfing will appear is meteor fragmentation or detachment of particulate matter from a leading edge. In the early 80s, Passey and Melosh [27] first studied the separation behavior of discrete fragments. The separation velocity was derived as:

$$V_T = \sqrt{C \frac{r_1 \rho_a}{r_2 \rho_m}} V \quad (1.1)$$

In Equation 1.1,  $V$ ,  $\rho_a$ , and  $\rho_m$  represents the velocity of the meteoroid through the atmosphere, the atmospheric density, and the meteoroid density, respectively. The variable  $C$  represents an empirical constant and  $r_1$  and  $r_2$  are the radius of the bodies where  $r_1 \geq r_2$ . The study showed that the dynamics of the smaller body will be dominated by the bow shock generated from the larger body upstream. However, the assumption of lateral separation caused a discrepancy in the separation velocity values derived from Equation 1.1. A further study was conducted by Laurence and Deiterding proving that findings for equally sized bodies cannot be extended to the behaviors of unequally sized bodies and that the scaling law of Passey and Melosh does not adequately predict separation behaviors of unequally sized bodies [34]. Laurence and Deiterding proved that the axial acceleration of the smaller body will be greater than that of the larger body. In this more accurate description, purely lateral separation is unlikely, and the concept of shock-surfing is introduced.

In a separate study, Laurence and Deiterding characterized the effects of shock-surfing on the separation dynamics of spherical bodies [31]. Surfing trajectories were evaluated from two different shock types: a ramp generated planar shock and a bow shock produced by a larger upstream body. Of the two cases studied, the effects of the planar oblique shock is the more simplified case. Nevertheless, it is the most relevant for this body of work. The effects of a planar oblique shock impingement on a blunt body were first studied by Edney in 1968 [3]. As Laurence and Deiterding built upon the foundational concepts established in the study performed by Edney, they were able to conclude that a relation of  $(\frac{L}{D})_{max} \geq \tan\beta$  determined the likelihood of shock surfing. In the relation, the variable  $\beta$  is the wave angle and  $L$  and  $D$  are the lift and drag force,

respectively, as the sphere interacts with the planar shock. The study established the required minimum value of  $\tan\beta$  for which shock surfing can occur as they correspond to different Mach numbers [31]. Figure 1.2 proved that as the Mach number decreased,  $\tan\beta$  becomes progressively limited, reducing the chance for shock-surfing.

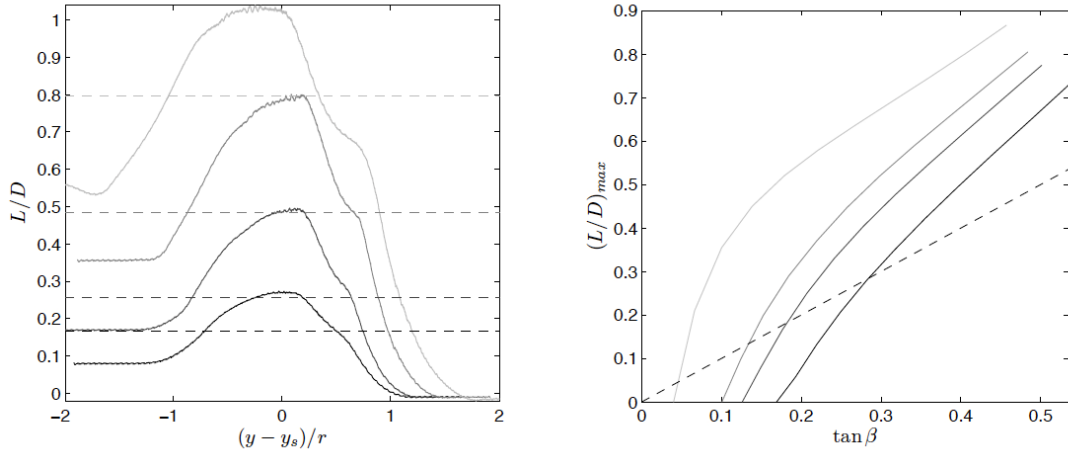


**Figure 1.2:** (Left) Ratio of lift to drag for sphere/oblique shock interactions, with wedge angles of 5, 10, 20, and 30° (dark to light). The horizontal dashed line for each shade indicates the tangent of the corresponding shock angle. (Right) The maximum  $L/D$  value versus the tangent of the shock angle for Mach numbers of (dark through light) 6, 8, 10, and 25. The dashed line corresponds to  $(\frac{L}{D})_{max} = \tan\beta$  [31]

### 1.2.2 Review of the Previous Study: Dynamics of a spherical body shedding from a hypersonic ramp

In a previous body of work [6], the dynamics of a sphere were observed as it separated from a 10° ramp in Mach 6 flow. The effect of the near ramp boundary layer on the sphere’s motion was studied experimentally and with an approximate

computational model. In the experimental methods, the sphere's diameter varied between 1.59 mm, 3.18 mm, 6.35 mm, and 9.53 mm. Similarly, the computational methods simulated the shedding behavior with spheres of 4 mm, 6 mm, 8 mm, 12 mm, and 16 mm diameter. The experimental results showed that with the variance in diameters, the spheres exhibited three distinct behaviors: shock surfing, initial expulsion from the shock area followed by reentry, and direct entrainment in the shock area [6]. Numerical simulations showed that the sphere force coefficients were altered by the near ramp boundary layer, which altered the overall dynamical behavior. This observation was validated experimentally. An increase in the sphere sizes led to a predominance of the expulsion to re-entrainment over shock surfing as the wall lift coefficients ejected the spheres outside of the shock area.

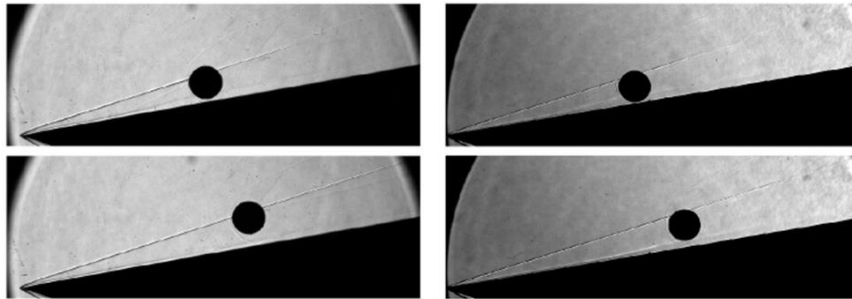


**Figure 1.3:** Shadowgraph images of the 9.53-mm sphere as it travelled downstream the ramp-generated shock [6]

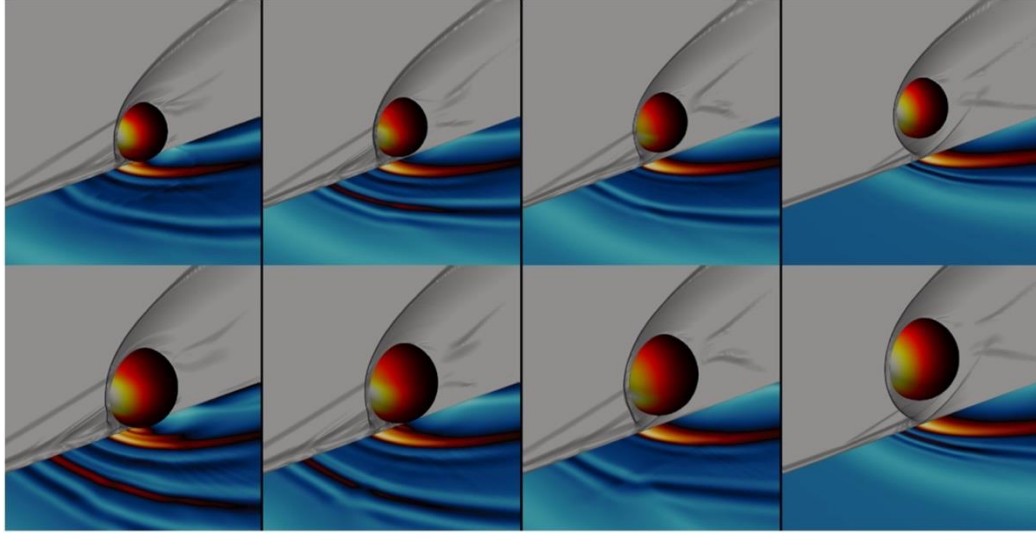


**Figure 1.4:** Numerical visualizations from the viscous sphere/boundary-layer simulations: (top) 6-mm diameter sphere and (bottom) 8-mm diameter sphere [6]

A few recommendations were made at the completion of the previous study and are outlined below:

- Further study on boundary layer characteristics such as the wall temperature ratio
- Effects of variations in Mach numbers and leading-edge ramp configurations to the near wall boundary layer
- Effects on separation trajectories due to deviations in purely spherical geometries

The body of work presented herein seeks to build upon this previous study with added complexities by replacing the spherical body with an ellipsoidal body. In the previous study, the sphere's uniform diameter in the XY, YZ and XZ planes prevented

any effects from pitch, roll, and yaw as it traversed downstream. However, in the case of the ellipsoid, the body is not dimensionally uniform in all directions. Therefore, pitch, roll and yaw will now become factors to consider when studying its motion. The added complexity demands careful evaluation of the ellipsoid's 6-DOF (degrees of freedom) motion and the resulting boundary layer. In the previous body of work, numerical simulations were employed; however, due to limitations of the codes employed, these were static simulations (from which an approximate dynamical model was constructed), restricting the accuracy of the derived behavior. To enable full dynamical simulations, a near-body/off-body (NBOB) solver with adequate adaptive grid refinement must be employed to predict the body's motion. This implies the need for a high-fidelity fluid solver that can simulate the near-ramp boundary layer and compute the corresponding flow properties.

### 1.3 Scope and Outline

The focus of this body of work is to employ experimental methods available at the University of Maryland to assess the predictive capability of Naval Air Systems Command's (NAVAIR) current modeling and simulation tools for hypersonic fixed wing flow problems. NAVAIR and other agencies across the Department of Defense (DoD) depend on simulation tools to predict the behavior of fluids, structures, and materials in hypersonic flows. However, the cost of testing and the limited available facilities make it difficult to obtain experimental data for hypersonic flow problems. As a result, NAVAIR has little experimental data to prove the fidelity of those simulations, especially for the type of moving-rigid-body problem considered here.

The primary objectives of this study are to:

- Experimentally characterize the separation dynamics of an ellipsoidal body from a two-dimensional ramp in hypersonic flow, and
- Verify/validate NAVAIR's computational prediction tool and its ability to produce high-fidelity simulations in hypersonic flows.

These objectives are accomplished by the following tasks:

- 1) Conduct experiments in UMD's Hypersonic Tunnel for Educational and Research Purposes (HyperTERP)
- 2) Use shadowgraph imaging to gather high-contrast images of the ellipsoid's motion
- 3) Apply an optical tracking routine to trace the ellipsoid's motion using the images gathered by the camera
- 4) Generate multiple levels of computational grids and conduct a refinement study to identify and minimize spatial and temporal discretization errors in the solution
- 5) Create a representative flow problem that resembles those conducted in the HyperTERP using Kestrel, NAVAIR's computational simulation tool
- 6) Compare experimental and computational results to assess the predictive capability of Kestrel for hypersonic, multi-body dynamics problems

## Chapter 2: Experimental Methods

### 2.1 Experimental Approach

All experiments were performed at the University of Maryland High-Speed Aerodynamics and Propulsion Laboratory (HAPL). The experimental apparatus consisted of the Hypersonic Tunnel for Educational and Research Purposes (HyperTERP). Each ellipsoid was placed on a  $10^\circ$  ramp inside the HyperTERP test section and exposed to Mach 6 flow. As the ellipsoid responded to the flow, a high-speed camera was used to capture the ellipsoid's motion in hundreds of shadowgraph images. An optical tracking routine was then employed to track the dynamics of the ellipsoid from the shadowgraph images. Full details of the experimental method are described in the following sections.

#### 2.1.1 HyperTERP

The HyperTERP is a hypersonic reflected shock tunnel with a Mach 6 free-jet nozzle which is used for free-flight experiments [4]. The schematic in Figure 2.2 illustrates the physical layout of the tunnel. The tunnel consists of a driver section, a primary diaphragm, a driven section, a secondary diaphragm, a Mach 6 nozzle, and a dump tank. The driver section is 5.4 m in length with an internal diameter of 100 mm. The primary diaphragm separates the driver and driven sections. It consists of two mylar diaphragms to produce a double burst mechanism. This allows for control of

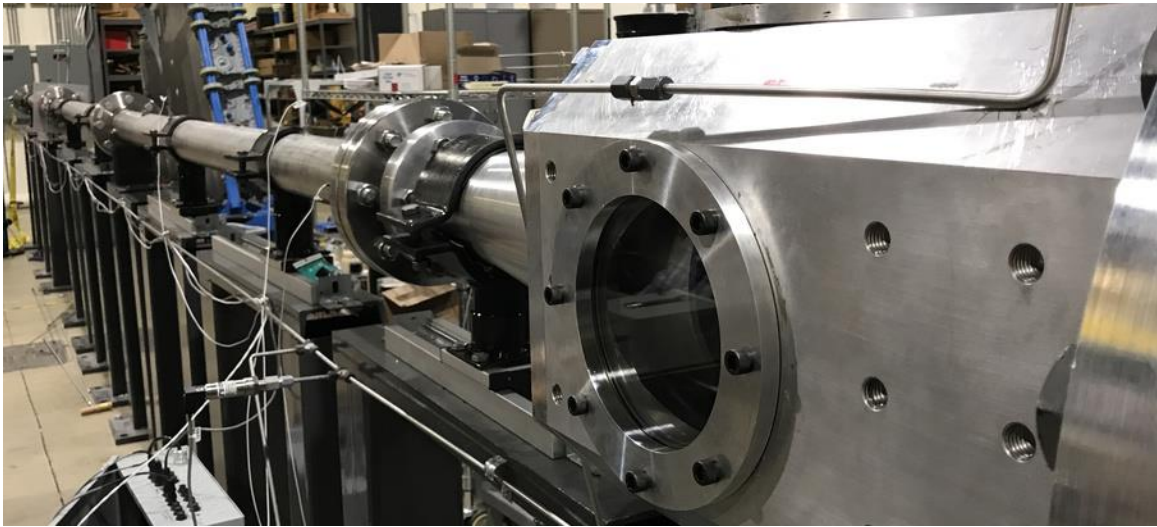


**Figure 2.1:** HyperTERP located at the University of Maryland.

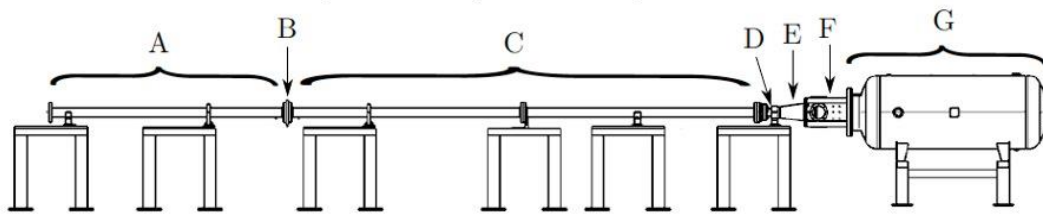


**Figure 2.2:** Schematic of shock tunnel used to perform the experimental testing

the burst conditions by preventing the high-pressure region in the driver section from expanding prematurely and triggering the shock. The driven section is a 6 m long tube with an internal diameter identical to the driver section. The secondary diaphragm, consisting of only a single mylar diaphragm, separates the driven section and the Mach 6 nozzle. A contoured nozzle was initially used for preliminary test runs but was replaced with a conical nozzle for most of the testing because of the shorter start-up time of the latter nozzle. The conical nozzle contains a  $7^\circ$  constant expansion angle with a throat and exit diameter of 23.88 mm and 200 mm, respectively. The cylindrical

test section has an internal diameter of 305 mm is equipped with three 152 mm circular windows for visualization purposes.

To fill the driver, driven, and primary diaphragm sections with the appropriate pressures, the tunnel was first reduced to a near vacuum. Once the entire tunnel reached ~3 kPa air, the driven section was pressurized to ~52 kPa air. Next, the driver section and primary diaphragm were filled with 350 kPa bar air, simultaneously. Finally, the primary diaphragm and the driver section was mixed with 750 and 1900 kPa Helium, respectively. The intermediate pressure in the primary diaphragm section (i.e., the volume between the two primary diaphragms) prevents a premature burst of the primary diaphragm. The tunnel was filled with the appropriate pressures to produce the desired freestream conditions found in Table 2.1.

$M$	$P_s$ (Pa)	$T_s$ (K)	$R_e$ [1/m]	$u$ (m/s)	$T_o$ (K)	$P_o$ (Pa)	$\rho$ kg/m <sup>3</sup>
6.32	599	102	3.7e+06	1281	890	1.35e+06	.0204

**Table 2.1:** HyperTERP freestream conditions

### 2.1.2 Shadowgraph Imaging

A focused shadowgraph configuration was used to capture high resolution images of the ellipsoid trajectories and the corresponding flow features. Two f/10 spherical mirrors of 152.4 mm diameter parallelized and refocused the light beam produced by a Cavitar Cavilux pulsed diode laser. High contrast images of the ellipsoids were captured for optical tracking purposes. Figure 2.3 displays an example of a shadowgraph image captured from a test. The Vision Research Phantom v2512 camera

recorded the images at 54,000 frames per second with a resolution of 896 x 464 pixels and an exposure time of 10  $\mu$ s (though note that the effective exposure time was determined by the shorter pulse width of the laser). Depending upon the time required for the ellipsoid to exit the field of view, each recording captured anywhere from 200-800 frames. The use of shadowgraph imaging minimizes the influence of flow features on the tracking accuracy while simultaneously maintaining focus on the ellipsoid [6]. Additionally, the ramp-generated shock, bow shock, and viscous boundary layer is captured in the recordings.

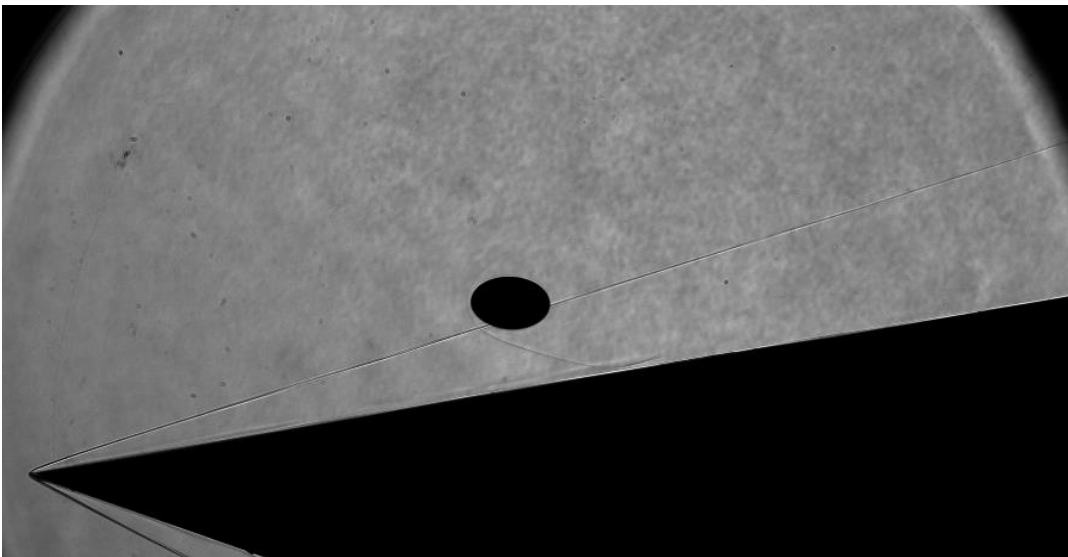


**Figure 2.3:** A shadowgraph of a single frame recorded during experimental testing.

### 2.1.3 Test Articles

The test articles for this campaign were ellipsoids of various diameters and a fixed planar ramp. Six different configurations of the ellipsoids were studied, three having a prolate geometry and three having an oblate geometry. The prolate ellipsoids contained

a single semi-major axis in the dimensional x-axis and two semi-minor axes in the dimensional y-axis and z-axis. The oblate ellipsoids contained two semi-major axes, one in the dimensional x-axis and y-axis, and a single semi-minor axis in the dimensional z-axis. Upon testing, each ellipsoid was positioned so that the dimensional x-axis was aligned in the streamwise direction, and the z-axis aligned with the wall normal direction of the ramp. Initially, a prolate ellipsoid of three different semi-major axis diameters was tested, but there was a significant amount of yaw in each test because of the varying diameter in the dimensional XY plane. After 4 tests with the prolate ellipsoid, it was decided to change the configuration to an oblate ellipsoid shape. With the change in shape, the radii in the dimensional XY plane are uniform and yaw should be excluded from the motion of the body (since they are rotationally symmetric about the yaw axis). The majority of the tests were performed with oblate ellipsoids with axis ratios 1.5:1.5:1 or 2:2:1. A schematic of the ellipsoids is found in Figure 2.4.

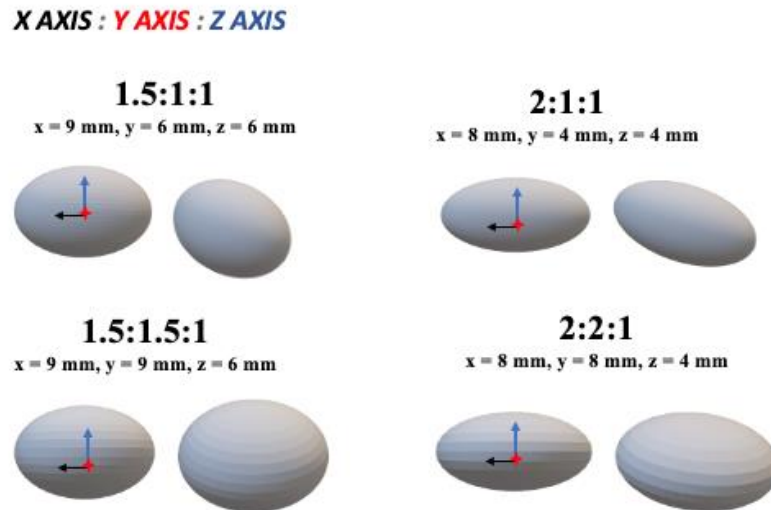


**Figure 2.4:** Schematic of the prolate ellipsoids (top). Schematic of oblate ellipsoids (bottom).

## 2.2 Optical Tracking Routine

The optical tracking routine is a mathematical tool used to convert the shadowgraph data from image space to physical space. In doing so, the ellipsoid motion can be analyzed. The fundamental concept of the tracking code is that the position and orientation of the model, which we collectively describe as the pose, are directly related to its silhouette through a one-to-one correspondence. The optical tracking routine is written in MATLAB and consists of two components: Edge Point Finding and Silhouette Fitting. The main workings of the code can be summarized as:

- 1) Initial selection of the pixel-resolution edge points
- 2) Refinement of the edge-points using sub-pixel precision
- 3) Generation of hypothetical outline for an arbitrary set of pose parameters from the corresponding CAD model
- 4) Iterate pose parameters to a best-fit solution between the refined edge points and generated CAD outline

Further details of these steps are provided in the following subsections.

### 2.2.1 Image Edge Point Detection

First, the edge point scheme is used to trace the outline of the ellipsoid in the experimental images. High contrast images are required for the routine to detect the edges of the outline. Therefore, high intensity backlighting is present in the wind tunnel as the ellipsoid travels downstream. As the ellipsoid is in motion, the images captured from the Vision Research Phantom v2512 camera displays a clear outline. A MATLAB

edge point script uses Canny edge detection, a mathematical toolbox that detects the edges using a binary system, where the pixels represented as edge points are zeros and all other pixels are ones [25]. Once the edges are identified, a sub-pixel routine resolves their locations for greater precision. The subpixel edge detection has proven to increase the accuracy of the optical tracking routine by a factor of 4 or more [30]. The sub-pixel routine starts by first increasing the intensity gradient at each pixel. A Gaussian filter is applied in the vertical and horizontal directions. The subpixel localization is performed in the vertical, horizontal, or diagonal direction. Central differencing is performed on all the edge points along a given line segment. The local edge direction is determined, and the subpixel localization is defined as the normal to that direction. Once the gradient has been defined for the edge points, a quadratic curve is applied to find the maximum intensity gradient along the direction of the edge points. Three points are used for this process: the edge point and the neighboring pixels on both sides of the gradient direction. Lastly, a correction is applied to the diagonal edges to improve accuracy of the subpixel localization.

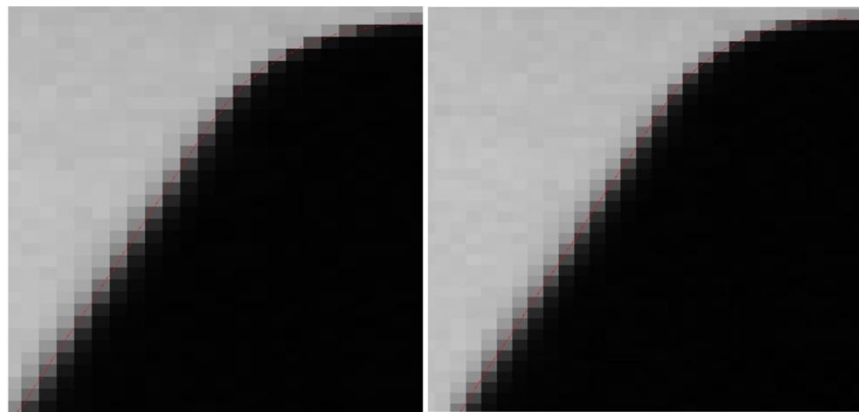


**Figure 2.5:** Edges detected without subpixel localization correction (left). Edges detected with subpixel localization correction (right).

Once the edge detection and subpixel edge detection are complete, the result is a final locus of points defining the ellipsoid outline. This can be seen in Figure 2.5. The process described in this section is performed for every frame collected by the Vision Research Phantom v2512 camera.

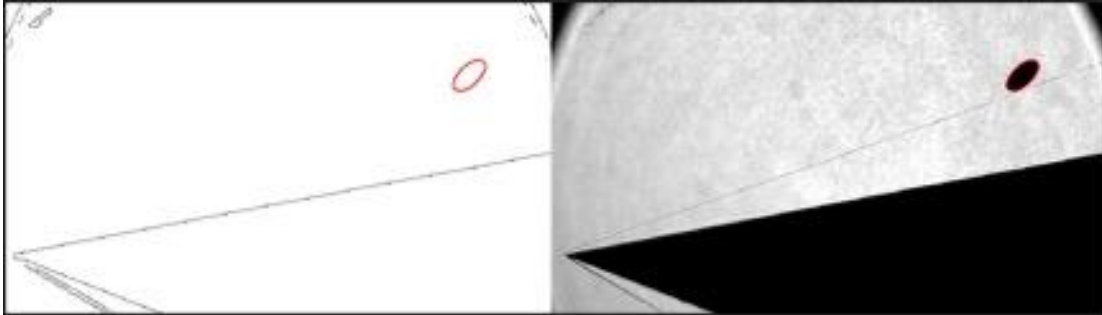


**Figure 2.6:** Binary image of edge points traced in pixel space (left). Traced edge points projected in image space to verify edge points detection (right)

### 2.2.2 CAD model of ellipsoid

To determine the pose parameters, we require a physical description of the ellipsoid outline to compare the detected image edge points too. Although it would, in principle, be possible to construct an analytical description of the outline from the ellipsoid geometry, a more general approach is through a CAD model of the ellipsoid. To begin, we define the pose vector as:

$$x \in \mathbb{R}^n \quad (2.1)$$

where  $n$  is the number of degrees of freedom. The computer model is oriented so that  $x$  is the axis aligned with the flow direction,  $y$  represents the lateral position, and the  $z$

axis is pointing vertically downward. For the ellipsoid's rotation, the Tait-Bryan angle rule is followed: yaw, pitch, and roll are about the  $z$ ,  $y$ , and  $x$  axis, respectively.

Starting from the CAD model, a simplified approach to silhouette generation is implemented by way of common computer graphic techniques. When using a computer model, the ellipsoid's silhouette  $C(x)$ , is represented by numerical values defined by a triangular mesh. CAD (Computer Aided Drawing) models are commonly exported in the format of an STL (stereolithography) file, where the surface mesh is comprised of triangles. In a triangular mesh, two vertex indices of an edge segment can only belong to one pair of triangles. This definition justifies the use of neighboring triangles in the edge detection routine. Neighboring triangles are essential when detecting the contours, or the set of edge segments that could potentially lie on the silhouette, from forward and backwards facing triangles. In the case of the ellipsoid's triangular mesh, the algorithm loops through all triangles until it finds another that contains the same two vertex indices.

A silhouette is defined not only by its contour, but also its visibility. Therefore, there must be a mechanism to mathematically define the space or world the ellipsoid traverses through. The camera model is a mathematical model of how the camera images the world. In the camera model, the camera is defined by the camera position,  $x_c$ . A horizontal and vertical axis,  $e_1$  and  $e_2$ , represent the two vectors that define the camera's orientation. The optical axis can be defined as:

$$I_a = -e_1 \times e_2 = e_3 \quad (2.2)$$

whereas the camera is positioned in the center of the image plane. A matrix transformation is used to map the world frame to the camera frame:

$$\hat{x} = [e_u; e_v; -e_u \times e_v]^{-1}(x - x_c) \quad (2.3)$$

where subscript  $u$  and  $v$  represent the horizontal and vertical axes, respectively. The camera frame is then mapped to the pixel frame using the following transformation matrix:

$$\begin{bmatrix} u \\ v \end{bmatrix} = \begin{bmatrix} \hat{x}_1 \\ K_u \\ \hat{x}_2 \\ K_v \end{bmatrix} + \frac{1}{2} \begin{bmatrix} N_u + 1 \\ N_v + 1 \end{bmatrix} \quad (2.4)$$

where  $N_u$  and  $N_v$  are the horizontal and vertical coordinates and  $K_u$  and  $K_v$  are the horizontal and vertical coordinates lengths, respectively. The pixel frame is the numerical value by which the ellipsoid's position is derived.

### 2.2.3 Silhouette Generation

As previously mentioned, the ellipsoid's contour and visibility are required to detect the edges of the body as it floats in space. A combined process using the computer and camera model is required so that the triangular mesh may be viewed in the camera frame. This combined process is separated into two steps:

- 1) Determine the triangular mesh contour using the computer and camera model
- 2) Determine the visible contours using computer graphics

First, the routine will detect forward and backward facing triangles which face towards and away from the camera. The triangles are connected at the front and back faces by a set of line segments, or edge line. Each triangle is comprised of three (3) line segments in which each line is shared between two triangles. Therefore, the number of total shared line segments for each pair of triangles is defined by:

$$\frac{3N_{tris}}{2} \quad (2.5)$$

These line segments determine the spatial relationship between neighboring triangles. Using this spatial relationship, the direction of the contours can be determined using the dot product. The positive dot product can be illustrated in Equation 2.6:

$$-\mathbf{r} \cdot \mathbf{n}_i \quad (2.6)$$

where  $\mathbf{r}$  is the incident light ray and  $\mathbf{n}_i$  represents the triangle surface normal vector. If the dot product in Equation 2.6 is positive, the triangle is facing forward and the converse is true if Equation 2.6 is negative. As the dot product is calculated for each triangle,  $\mathbf{n}_i$  is updated based on the current pose of the ellipsoid. The result of the dot

product for each triangle is compared to the neighbor map. If a pair of triangular elements are facing the opposite direction (forward and backward) then the connecting line segment is a contour.

The second step in the silhouette fitting is proof of visibility of the contours. Computer graphics ray tracing is used to determine if the line segments identified in the first step are visible to the camera. Light rays are projected from the camera view to points located at the line segments. If the light ray does not intersect any other triangular segment, it is considered a contour. In some cases, the visibility check is unnecessary. For a convex shape (like the ellipsoid in this present study), the collection of line segments determined from the contour detection defines the computational silhouette of the model.

#### 2.2.4 Error Characterization and Iteration Scheme

Once the edges are detected, there are two final steps needed to determine the position and orientation of the ellipsoid in the images:

- 1) Define a metric that quantifies the “goodness of fit”
- 2) Minimize the error for all combinations of pose parameters

The “goodness of fit” metric applied to minimize the errors propagated during edge detection is the root-mean-square distance between each edge point and the nearest location on the silhouette. It is defined as below:

$$RMS = \sqrt{\frac{1}{N} \sum_{i=1}^N \| \mathbf{x}_{ep,i} - \mathbf{x}_{s,i} \|^2} \quad (2.7)$$

where  $\mathbf{x}_{ep,i}$  is the  $i$ 'th (of  $N$ ) edge points and  $\mathbf{x}_{s,i}$  is the nearest location on the reconstructed silhouette (which comprises a collection of connected line segments).

The process to the  $RMS$  is defined below:

- 1) For each line segment considered, calculate the minimum orthogonal approach distance along that segment to  $\mathbf{x}_{ep,i}$  and take the minimum approach distance among all such line segments
- 2) Calculate the minimum distances from points (1) and (2) and equate to  $|\mathbf{x}_{ep,i} - \mathbf{x}_{s,i}|$
- 3) Square and sum over all edge points

To decrease computational requirements for step (1) above, we first calculate the distances from the given  $\mathbf{x}_{ep,i}$  to the end points of each line segment; the calculation of the minimum orthogonal distance is then only performed for the line segments with the three nearest end points to  $\mathbf{x}_{ep,i}$ .

Minimization of the  $RMS$  over the pose-parameter space is achieved by applying a gradient descent algorithm. A gradient descent is a first order optimization algorithm used to find the local maximum and minimum of a function. The gradient

descent method avails greater stability, in turn, allowing for convergence of the solution. The pose parameter vector is then updated iteratively as:

$$\mathbf{p}_{n+1} = \mathbf{p}_n - \gamma \nabla RMS(\mathbf{p}_n), \quad (2.8)$$

where  $\gamma$  is the designated step size and  $\nabla RMS$  is the Jacobian vector. Note that  $\gamma$  is a vector quantity and varies for each different pose parameter.

In general, the Jacobian vector is a vector of partial derivatives with respect to the variables of that function. In this case, the RMS Jacobian is the derivative of the RMS value with respect to the corresponding pose parameter. It is calculated numerically by incrementing the pose parameter independently and calculating the corresponding RMS. A step size of  $1 \times 10^{-8}$  is found to be generally appropriate but can certainly change based on more complex geometries.

The step size is a critical parameter when using the gradient descent method to converge to a solution. The step size is employed to refine the solution through each iteration and can be detrimental to the time to converge if too small or too large. If too small, the algorithm will converge very slowly to a solution. If too large, the algorithm will perform frequent line searches. Essentially, both extremes where the step size is too large or small, will become time consuming.

A line search is an added step to ensure that convergence is still achievable through each iteration. If  $RMS(\mathbf{p}_{n+1})$  is larger than  $RMS(\mathbf{p}_n)$  for a given step size, then a line search will be initialized. The vector values between  $RMS(\mathbf{p}_{n+1})$  and

$RMS(\mathbf{p}_n)$  should monotonically increase from zero to one. All values between  $RMS(\mathbf{p}_{n+1})$  and  $RMS(\mathbf{p}_n)$  can be calculated as follows:

$$\mathbf{p}_n - \epsilon\gamma\nabla RMS(\mathbf{p}_n). \quad (2.9)$$

The new  $RMS(\mathbf{p}_{n+1})$  is updated by determining the new minimum RMS over all entries in that pose parameter. If the new minimum occurs at the original  $\mathbf{p}_n$ , then the new point is represented as:

$$\mathbf{p}_n - 0.5\epsilon_{min}\gamma\nabla RMS(\mathbf{p}_n). \quad (2.10)$$

In the line search, if no minimum can be found, then the chosen  $\gamma$  value is too large, and the algorithm will reduce it by an order of magnitude [32]. Figure 2.7 shows an example of the convergence in the RMS from the edge fitting algorithm. The values of the initial guess are as follows:  $x = 560$  pixels,  $y = -243$  pixels, and  $\text{pitch} = -133.3^\circ$ . The values of the final solution after the RMS convergence are:  $572.46$  pixels,  $y = -242.66$  pixels, and  $\text{pitch} = -135.41^\circ$ . After 20 iterations, the solution converges, and the RMS derivative is reduced by multiple orders of magnitude for each parameter.

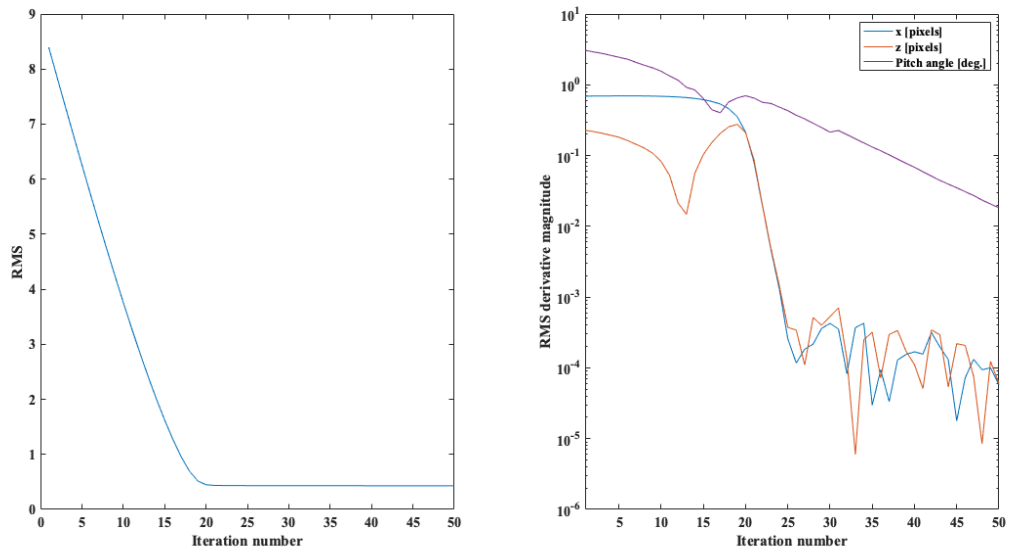


**Figure 2.7:** (Left) RMS convergence of pose parameter with poor initial guess. (Right) RMS derivative magnitude of pose parameter.

## Chapter 3: Computational Methods

### 3.1 Computational Approach

Computational simulations were compared against experimental data to assess the accuracy of Kestrel, NAVAIR's primary fixed-wing hypersonic flight simulation tool, in simulating the present separation problem. Kestrel is a high-fidelity flow solver with the capability of simulating coupling aerodynamics, thermochemistry, structural dynamics, thermodynamics, propulsion, and flight controls. The flow solver supports regimes ranging from incompressible to hypersonic speeds. Kestrel's ability to compute unsteady boundary layers at high speeds suggested it to be a suitable candidate for this study, considering the nature of the ellipsoid's dynamics. Computational simulations were designed to replicate certain experimental cases for the purpose of comparing experimental and numerical data. The results were used to validate the accuracy of the flow solver. The process for the computational method is briefly summarized below:

- 1) A grid generation tool, Capstone, is employed for the initial grid generation of the ellipsoid and ramp
- 2) The simulation is constructed within Kestrel to replicate the HyperTERP experimental freestream conditions
- 3) A grid refinement study is performed to determine the temporal and spatial convergence of the simulation
- 4) Post processing is performed to analyze computational results

The details of the computational method are described in the following section.

### 3.1.1 Grid Generation

The generation of the computational mesh/grid is critical to yielding an accurate numerical simulation. Furthermore, the sizing of the grid cells at the surface of the ellipsoid and ramp geometry, volumetric boundary layer, and farfield is crucial for precise flow computations. In this study, Capstone was employed to produce all computational grids. Capstone is a CREATE-FT (Fundamental Technologies) tool used to create, modify, and query geometry grids and attribution information needed to define a digital model for physics-based simulations of complex engineering systems [8]. Capstone has capabilities to support highly complex flow field applications such as aircraft, ships, submarines, and design of radio-frequency antenna systems by generating unstructured anisotropic grids [8].

First, grid generation was required for the ellipsoid, ramp and Cartesian overset, independently. The ellipsoid and ramp grids were generated by user input in Capstone and were composed of unstructured geometries on the surface and in the volume boundary layer. An off-body grid was automatically generated by Kestrel once the unstructured grids were loaded into the system. The Cartesian grid is a non-uniform structured grid that communicates with the ellipsoid and ramp near-body grids via an overset boundary. It allows for computation of the ellipsoid's boundary layer as it travels downstream through iterative grid adaptation and refinement.

Multiple versions of the unstructured grids were created to determine optimal surface, volume, and global cell sizing. The initial cell sizing on the geometry surface,

the volumetric boundary layer, and the bounding box (farfield) was derived from the longest length of the ellipsoid. In all simulations, the 1.5 ratio (in the major-minor axis) ellipsoid was used. Therefore, the reference length for initial cell sizing was .009 m. The sizing for the unstructured grid is found in Table 3.1, where all unit lengths are in meters.

	<b>Ellipsoid</b>	<b>Ramp</b>
Global Sizing	$2.5 \times 10^{-4}$	$5 \times 10^{-3}$
Topos Sizing	Curvature H/L = 0.628 125 points on circle	Top Surface = $5 \times 10^{-4}$ Other Surfaces = $1.2 \times 10^{-3}$
Edge Boundary Layer	N/A	Total Layer Thickness = $3.79 \times 10^{-3}$ First Layer Thickness = $1.5475 \times 10^{-4}$ Last Layer Thickness = $4.86 \times 10^{-4}$ Number of Layers = 13 Growth Rate = 1.1
Volumetric Boundary Layer	Total Layer Thickness = $1.064 \times 10^{-3}$ First Layer Thickness = $2.553 \times 10^{-6}$ Last Layer Thickness = $1.793 \times 10^{-4}$ Number of Layers = 25 Growth Rate = 1.2	Total Layer Thickness = $2.71 \times 10^{-2}$ First Layer Thickness = $1.0 \times 10^{-4}$ Last Layer Thickness = $4.4 \times 10^{-2}$ Number of Layers = 22 Growth Rate = 1.2

**Table 3.1:** Initial global sizing for computational grids. All unit lengths are in meters

The ellipsoid and ramp each have a corresponding volumetric boundary layer that is determined by the topos sizing. The topos sizing is essentially the sizing on the surface of the ramp and ellipsoid geometry. The ellipsoid leveraged Capstone’s ability to perform curvature-based sizing for acceptable contour resolution. Capstone’s localized sizing feature was used for the ramp surfaces, where the top surface is more refined than the back, left, right and bottom surfaces. In this case, the purpose of employing

localized cell sizing is to resolve larger flow gradients where the ellipsoid is near the ramp during the simulation. The sharp edges of the ramp made it necessary to assign an edge boundary layer. However, the curvature sizing feature in Capstone eliminates the need for an edge boundary layer on the ellipsoid. A volumetric boundary layer is needed for both the ellipsoid and ramp for computation of the boundary layer and corresponding flow features. Equation 3.1 represents the correlation by which the volumetric boundary layer is constructed where  $R_e$  represents the Reynolds number,  $L_{ref}$  is reference length, and  $L_{max}$  is the longest length of the geometry.

$$\frac{R_e}{L_{ref}} \times L_{max} \quad (3.1)$$

For both cases,  $R_e = 6.38 \times 10^6$  and  $L_{ref} = 1.0$  m. The values of  $L_{max}$  for the ellipsoid and the ramp are 0.009 m and 0.12 m, respectively.

A grid refinement study was conducted to determine grid dependency of temporal and spatial convergence of the solution. Each grid was refined from the baseline coarse grid cell sizing by a factor of  $1/\sqrt{2}$ . In each case, the Cartesian grid is automated by Kestrel and is dependent on the sizing of the unstructured ramp and ellipsoid grid. More discussion on the grid refinement study is found in Chapter 5. The untrimmed coarse grids for the ellipsoid and ramp are illustrated in Figure 3.1.

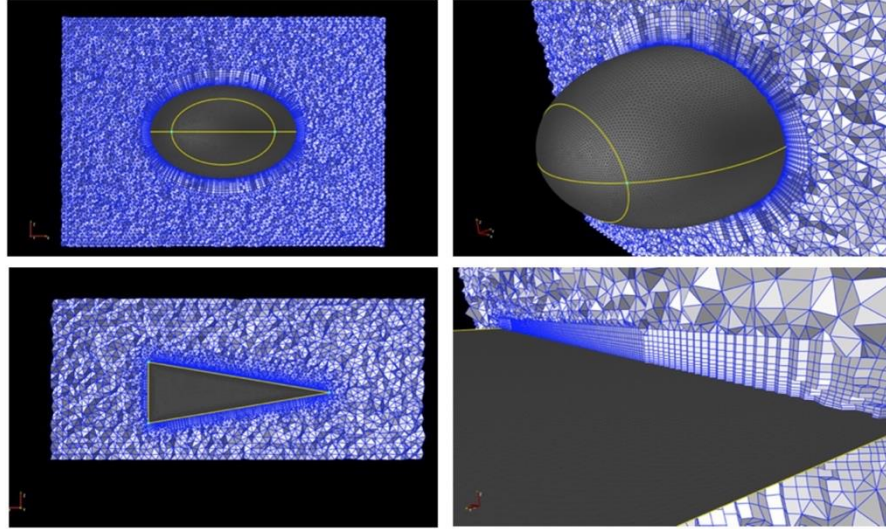


**Figure 3.1** XZ plane view of ellipsoid (top left) and ramp (bottom left) grid with cut plane view of the untrimmed volumetric boundary layer. Orthogonal view of ellipsoid (top right) and ramp (bottom right) grid.

### 3.1.2 Kestrel: Hypersonic Flow Solver

A significant portion of this study is the assessment of the flow solver, Kestrel. As previously mentioned, Kestrel is the primary simulation tool used by NAVAIR to predict hypersonic flow properties for fixed wing applications. Kestrel was employed to solve the simplified case of an ellipsoid separating from a  $10^\circ$  ramp. The simulation case was built in KUI, the Kestrel User Interface.

The laminar Navier-Stokes (NS) equations were employed to initialize Kestrel's global CFD solver, with an assumption of compressible laminar flow. The governing equations for the flow problem are found in Equations 3.2, 3.3, and 3.4.

$$\frac{\partial}{\partial t} \iiint_{\mathcal{V}} \rho d\mathcal{V} + \iint_S \rho(\vec{u} \cdot \hat{n}) dS = 0 \quad (3.2)$$

$$\iiint_{\mathcal{V}} \frac{\partial(\rho\vec{u})}{\partial t} d\mathcal{V} + \iint_S \rho\vec{u}(\vec{u} \cdot \hat{n}) dS = \iiint_{\mathcal{V}} \rho\vec{f} d\mathcal{V} \iint_S p(\hat{n} dS) + \vec{F}_{viscous} \quad (3.3)$$

$$\begin{aligned} \iiint_{\mathcal{V}} \frac{\partial}{\partial t} \rho \left( e + \frac{u^2}{2} \right) d\mathcal{V} + \iint_S \rho \left( e + \frac{u^2}{2} \right) (\vec{u} \cdot \hat{n}) dS \\ = \iiint_{\mathcal{V}} \rho(\vec{f} \cdot \vec{u}) d\mathcal{V} - \iint_S p\vec{u}(\hat{n} dS) + \iiint_{\mathcal{V}} \dot{q}\rho d\mathcal{V} \\ + \dot{W}_{viscous} \end{aligned} \quad (3.4)$$

The continuity equation enforces conservation of mass such that mass is neither created nor destroyed. First, examine a fixed control volume (CV) with a volume of  $\mathcal{V}$ . A closed surface defined by  $dS$  is the elemental surface area, and  $\hat{n}$  is the normal unit vector to that surface. Let  $\vec{u}$  represent the local velocity and let  $\rho$  represent the density of the fluid element. The volume integral represents the time rate of change of the mass inside the CV and the surface integral represents the mass flow through the surface area  $S$ . The conservation of momentum in Equation 3.3 states that the time rate of change of momentum of a body equals the net force exerted. The left-hand side represents the time-dependent change of momentum in the fluid element and net flow rate of momentum through the elemental surface area  $\hat{n}dS$ . The right-hand side represents the body forces, surface forces, and viscous forces. Equation 3.4 represents the conservation of energy and states that energy can neither be created nor destroyed.

Equation 3.4 consists of three main principles: the rate of heat added to the fluid inside the CV from its surroundings, the rate of work done inside the fluid inside the CV, and the rate of energy of the fluid as it flows through the CV. The first term on the left-hand side represents the time rate of change of energy inside the fluid element due to time dependent variations in the flow. The second term on the left-hand side represents the net rate of change in energy due to flow entering and exiting the control volume. The first two terms on the right-hand side represents the total work done on the fluid from inside the CV. The third term on the right-hand side represents the work done on the fluid due to heat addition, and the last term on the right-hand side represents the work done on the fluid element due to viscous stresses on the surface [24]. These three principles form the foundation to Kestrel's laminar NS flow solver.

The initial positioning of the ellipsoid in the computational case was modeled to approximately represent one of the experimental cases where the shock impinged slightly below the ellipsoid's semi-major axis. To simulate this in Kestrel, the ellipsoid was positioned 15.5 mm from the leading edge of the ramp with a starting pitch of -14.6°. The freestream conditions were established in KUI to represent those of the experimental methods. The known conditions of static pressure, static temperature, and the Mach number were user-defined, and all other conditions were calculated automatically. These conditions were compared to the freestream conditions in HyperTERP to validate the accuracy of the simulated flow environment. The comparison of the freestream conditions are found in Table 3.2.

Condition	Kestrel	HyperTERP
$M$	6.32	6.32
$P_s$	599 Pa	599 Pa
$T_s$	102 K	102 K
$R_e$	$3.7 \times 10^6$ [1/m]	$3.7 \times 10^6$ [1/m]
$u$	1279.45 m/s	1281 m/s
$T_o$	916.82 K	890 K
$P_o$	$1.3 \times 10^6$ Pa	$1.35 \times 10^6$ Pa
$\rho$	.0205 kg/m <sup>3</sup>	.0204 kg/m <sup>3</sup>

**Table 3.2:** Comparison of the computational and experimental freestream conditions

The boundary conditions for the simulation included no-slip and overset conditions for both the ramp and ellipsoid, and a Cartesian farfield. The boundary conditions were defined by the computational grids generated in Capstone. Overset boundary conditions were defined by the bounding box of the ramp and ellipsoid. The ellipsoid and ramp volumetric boundary layers (as seen in Figure 3.1) were trimmed to allow for the near-body/off-body paradigm. The trimmed grids are illustrated in Figure 3.2. The Cartesian overset was automated by Kestrel as the off-body solver feature was triggered.



**Figure 3.2:** Trimmed no slip boundary condition of the ellipsoid (left) and ramp (right) with a trim distance of .0015 m and .005 m, respectively.

### 3.1.3 SAMAir Solver

Adaptive grid/mesh refinement is necessary to accurately capture flow features away from a primary body. In the case of the ellipsoid's off-body motion, SAMAir is employed as the off-body solver. Unlike the unstructured grids, the Cartesian grid is automated by Kestrel. The Cartesian grid specification is defined by length multiples where reference lengths in the forward, aft, left, right, upper, and lower boundaries determine the total boundary size. SAMAir applied a fifth-order spatial discretization and a second-order temporal discretization. The CFL number has a range of 100-1000 with a ramping factor of 0.2. The WENO (weighted essentially non-oscillatory) limiter was applied to the SAMAir solver to control oscillations and instabilities; this is most helpful around the shock where the compressibility of the flow may cause discontinuities. Within the Cartesian grid itself is a refinement region. This is a user-defined feature to avoid refining in areas of the grid that are unimportant, ultimately saving computational cost and time. The refinement region was defined around the ellipsoid, and the shock sensor was designated as the refinement variable.

## Chapter 4: Experimental Results

### 4.1 Experimental Variables

Firstly, we must note the experimental parameters in this study, as each will impact the trajectory and dynamics of the ellipsoids. Three variables must be considered: the ellipsoid's geometry (i.e., aspect ratio), the starting position of the ellipsoid relative to the ramp's leading edge, and the initial pitch of the ellipsoid at rest.

#### 4.1.1 Ellipsoid Geometry

Twenty-four ellipsoids in total were tested in the HyperTERP, varying in six different configurations. The dimensional matrix is outlined in Table 4.1.

Configuration	Diameter in x:y:z axes (mm)	Aspect Ratio in X:Y:Z axes	Number of ellipsoids tested
A	9:6:6	1.5:1:1	1
B	8:4:4	2:1:1	2
C	9:4:4	2.25:1:1	1
D	9:9:6	1.5:1.5:1	8
E	8:8:4	2:2:1	11
F	9:9:4	2.25:2.25:1	1
			Total = 24

**Table 4.1:** Dimensional Matrix of the Ellipsoids

The CAD model of the dimensional configurations is also pictured in Figure 2.4. Configurations A, B, and C were used in preliminary testing to verify the proper

conditions and methods. In the preliminary tests, the ellipsoid motion was dominated by yaw. As a mitigation, the geometries were modified, resulting in Configurations D, E, and F. The preliminary tests also proved that there was not much difference in the dynamic behavior of Configurations E and F. Therefore, it was determined that Configurations D and E would provide the most useful data moving forward.

Of the twenty-four ellipsoids tested, seven were studied in detail, i.e., the separation trajectories were analyzed using the optical tracking code. These ellipsoids were strategically chosen based on factors such as initial shock impingent, trajectory type, and similar shedding behavior. The ellipsoids with the corresponding configurations can be found in Table 4.2. The numbers are assigned according to the ellipsoid’s initial distance (increasing) from the ramp leading edge, i.e., D1 had the closest initial position to the leading edge of the D-configuration experiments.

Test Number	Configuration
Shot #5	D2
Shot #13	D1
Shot #14	D3
Shot #15	E2
Shot #18	E3
Shot #20	D4
Shot #22	E1

**Table 4.2:** Ellipsoids studied with optical tracking routine and their corresponding configurations

#### 4.1.2 Initial Configuration

One of the factors contributing to the ellipsoid's separation behavior is the initial configuration. Therefore, it is therefore imperative to detail in the following section.

There are two variables that ultimately determine the ellipsoid's initial configuration: the ellipsoid's starting distance relative to the ramp's leading edge and the initial pitch of the ellipsoid. The optical tracking code was used to determine the starting distance of the ellipsoid relative to the ramp's leading edge. Employing the process detailed in Section 2.2, the ellipsoid and leading-edge pixel coordinates were extracted from the pose vector of the first frame. The pixel distance of the ellipsoid parallel to the ramp was recorded and converted to a dimensional value using an averaged scale value,  $S_A$ , which was also derived from the optical tracking code. However, non-dimensional values will be used for all analyses in this section, as the dimensional starting distance was only used as a reference to later build the computational configuration in Chapter 5. The non-dimensional relations for the initial position are defined as  $x_0/r$  and  $y_0/r$ , where  $x_0$  and  $y_0$  are the initial x and y pixel coordinates, normalized by the value  $r$  (also in pixels):

$$r = r_e \times S_A \tag{4.1}$$

In Equation 4.1,  $r_e$  represents the average length of the ellipsoid's semi-major and semi-minor axes, and a summary of the value  $r$  for each configuration is found in Appendix A5.

Configuration	Starting distance (mm)	$x_0/r$	$y_0/r$	Initial Pitch (°)	Shock Impingement
D1	11.3138	1.7287	0.1574	-14.9556	Below
D2	11.0910	1.8159	0.2911	-16.2864	Below
D3	17.8663	2.6393	0.3164	-17.6700	Centered
D4	8.8287	3.6349	0.7161	-15.8874	Above
E1	19.0681	1.7135	0.4422	-8.1195	Below
E2	24.9602	1.8319	0.3818	-12.2164	Below
E3	8.4124	2.8358	0.5565	-10.4159	Above

**Table 4.3:** Experimental results of ellipsoid initial position and corresponding shock impingements

The initial pitch about the ellipsoids Y axis (as pictured in Figure 2.4) is also an important parameter and was evaluated in all cases. The initial pitch of the ellipsoid is an uncontrolled variable, as the resting pitch position is dominated by a combination of gravity and the surface friction at the interface of the ellipsoid and ramp. In Table 4.3, some variation was observed from run to run even for the same nominal geometry. Nevertheless, each initial pitch value contributes to the impingement of the shock, in turn, affecting the trajectory of the ellipsoid. As each configuration has a unique initial position due to the combination of starting distance and initial pitch, a corresponding shock impingement will result. The initial position, initial pitch and corresponding shock impingement is recorded in Table 4.3.

#### 4.2 Ellipsoid Trajectories

As previously mentioned, there were three distinct behaviors exhibited by the sphere in the previous body of work: shock-wave surfing, initial expulsion from the shock area followed by reentry, and direct entrainment in the shock area. Similar

qualitative behavior was observed in the present experiments with ellipsoids, though complicated by the ability of the body to undergo pitching motion while separating. Consequently, a new trajectory type was introduced in this study: initial expulsion to shock-wave surfing.

To familiarize the reader with each trajectory type, examples are shown in Figure 4.2. In the shock-wave surfing trajectory type shown in the left three images in Figure 4.2, the ellipsoid follows the oblique shock generated by the ramp upstream. In the center three images of Figure 4.2, the expulsion to surfing trajectory type is shown. This trajectory, which was absent in the previous study, is one where the ellipsoid is immediately ejected from the shock layer. As the ellipsoid continues its motion downstream, it pitches in the clockwise direction. At some point, the semi-major axis of the ellipsoid will reapproach a parallel position with the shock and surf the shock until it exits the test section. Lastly, the direct entrainment trajectory is referenced in the right three images in Figure 4.2. Here, the ellipsoid pitches downward upon separation and immediately enters and remains in the shock area as it traverses downstream. Table 4.4 summarizes the behavior observed in the experiments considered, with the initial distances downstream from the leading edge, the normalized lateral distances from the shock, and the resulting trajectory types for the ellipsoids provided. Comparing with Table 4.3, Configuration D4 and E3 each having a shock impingement above the ellipsoid's semi-major axis, which result in negative  $(y_0 - y_s)/r$  values of -0.0708 and -0.1284, respectively.

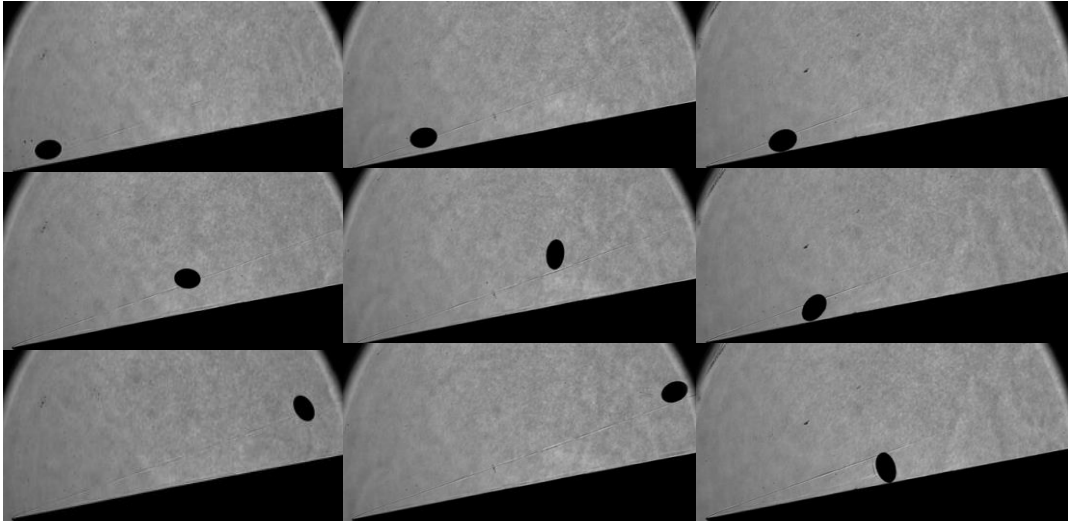


**Figure 4.1:** Shock-wave surfing trajectory (left 3 images). Expulsion to surfing (center 3 images). Direct entrainment (right 3 images)

Configuration	$x_0/r$	$(y_0 - y_s)/r$	Trajectory Type
D1	1.7287	0.1767	Shock Surfing
D2	1.8159	0.1990	Expulsion to Surfing
D3	2.6393	0.0731	Expulsion to Surfing
D4	3.6349	-0.0708	Direct Entrainment
E1	1.7135	0.1659	Expulsion to Surfing
E2	1.8319	0.0878	Expulsion to Surfing
E3	2.8358	-0.1284	Expulsion to Surfing

**Table 4.4:** Trajectory behaviors exhibited by each shot

Given the potential for shot-to-shot variation, even with nominally the same configuration, it is necessary to assess the repeatability of the trajectories relative to their corresponding shock impingements. Although the initial positions and orientations weren't able to be exactly reproduced in different experiments, we note from Table 4.3 that Configurations D1 and D2 are sufficiently close in their initial configurations that they can be reasonably compared, and similarly with

Configurations E1 and E2. As can be seen in Figure 4.3, Configurations E1 and E2 resulted in nearly identical separation trajectories despite a subtle difference in their initial positions. The shadowgraph images of the two cases can be seen in Figure 4.4 and show very close agreement.

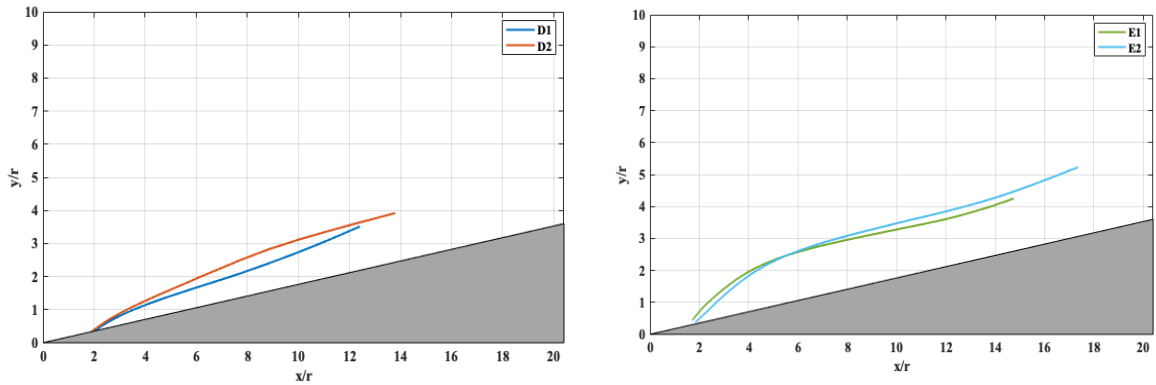


**Figure 4.2:** Comparable trajectories with similar shock impingements

The large initial expulsion caused E1 and E2 to exhibit a maximum  $(y - y_s)/r$  value of 0.997 and 0.993, respectively, and a rapid increase in pitch angle. However, as seen in most trajectories, the semi-major axis of the ellipsoid then becomes more aligned with the shock and the trajectory begins to return towards the shock layer. A somewhat larger discrepancy is noted between Configurations D1 and D2, despite their having very similar initial positions and shock impingements. This can be seen in Figure 4.3 and demonstrates that the ellipsoid dynamics can be very sensitive to the exact initial configuration. The results in Figure 4.3 suggests that trajectory repeatability is more easily achievable with a similar shock impingement in the ellipsoids of Configuration

E compared to Configuration D, though we lack a sufficient number of data points to show this conclusively. We now continue our analysis of all other trajectories.

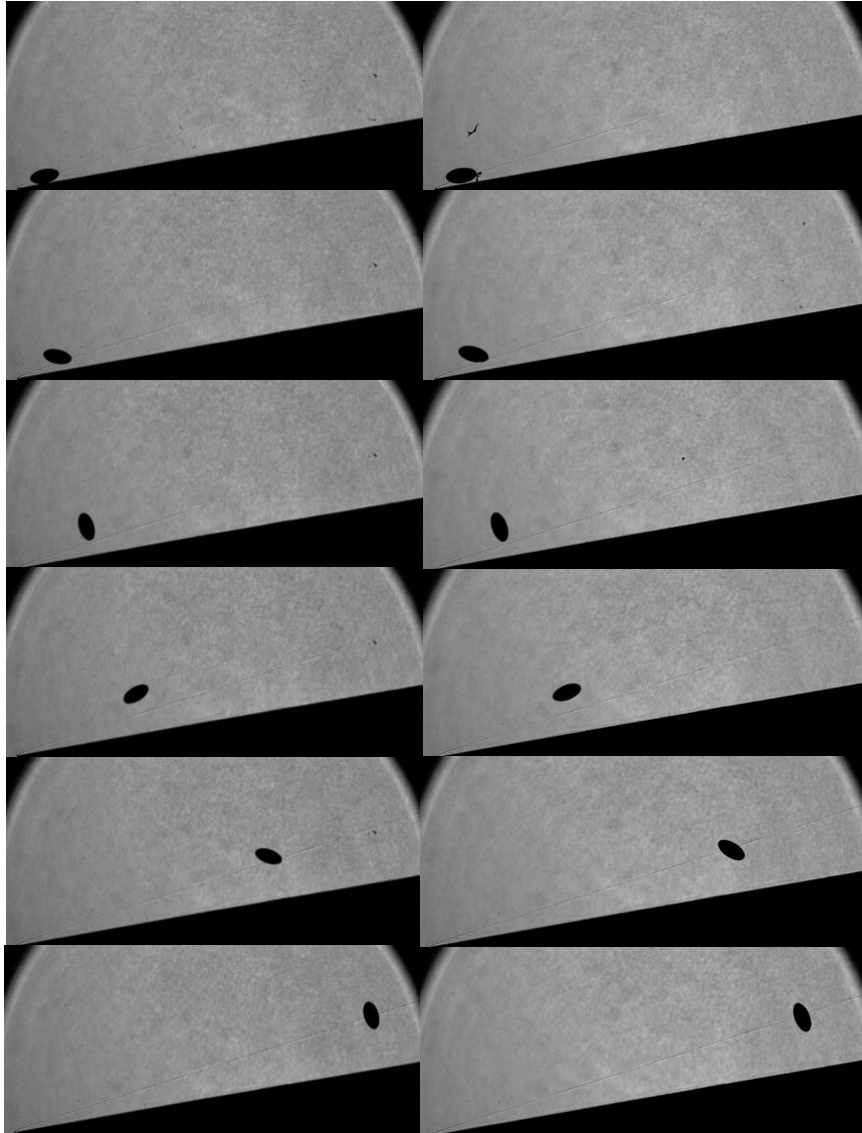


**Figure 4.3:** Experimental shadowgraph images of Configuration E2 (left) and Configuration E1 (right)

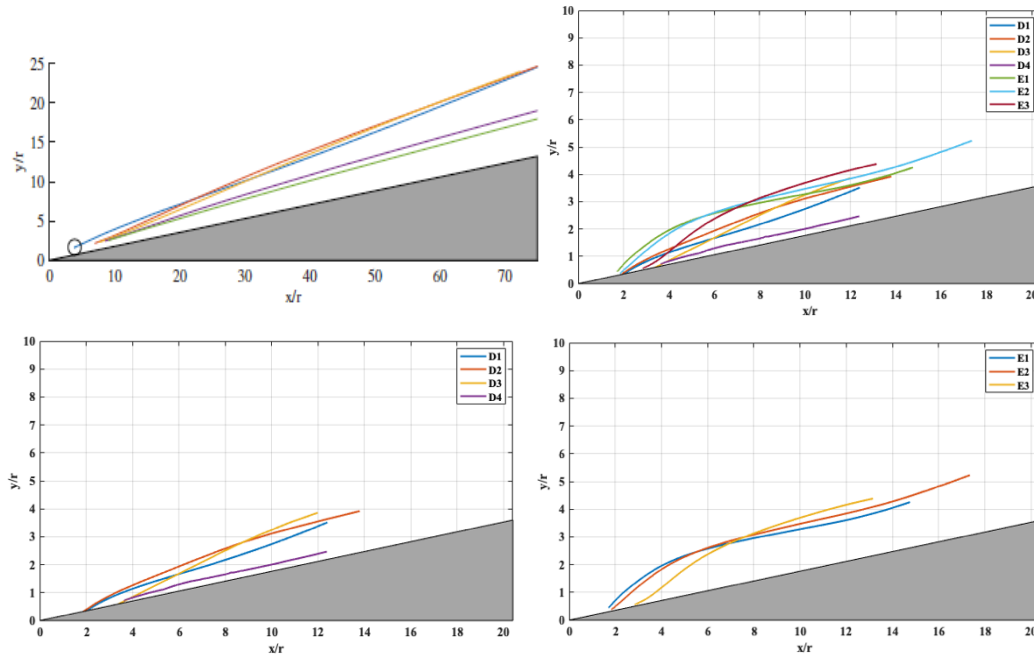


**Figure 4.4:** 3.18 mm spherical trajectories from previous study (top left). Comparison of all ellipsoidal trajectories (top right). Trajectories of ellipsoids with Configuration D (bottom left) and E (bottom right)

With the introduction of pitch to the dynamics of the separating body, the expulsion from the shock area appeared to be much more exaggerated in the ellipsoid trajectories compared to the sphere from the previous work. We can attribute this to an initial pitch-up moment that increases the pitch angle and thus the lift force generated by the ellipsoid, rapidly ejecting it from the shock layer. However, following this initial expulsion, the ellipsoid consistently re-approached the shock before leaving the test section. Additionally, the ellipsoid trajectories were much more sensitive to the initial shock impingement when compared to the sphere trajectories, as it influenced the pitch upon separation. Nevertheless, the ellipsoid displayed comparable behaviors to that of

the sphere at some point in the seven tests analyzed. Figure 4.4 shows experimental data from the 3.18-mm sphere trajectories from the previous study, compared to the ellipsoid trajectories of Configuration D and E. Two of the trajectory types from the previous study (shock surfing and direct entrainment) appeared in the test shots belonging to Configuration D. Despite the differences in shock impingement, all test shots belonging to Configuration E resulted only in expulsion to surfing. Of the seven tests analyzed, Configuration D1 displayed the lowest total change in pitch angle of only  $54.35^\circ$  in the clockwise direction. In this case, the ellipsoid surfed the oblique shock generated by the leading edge of the ramp as it traversed downstream.

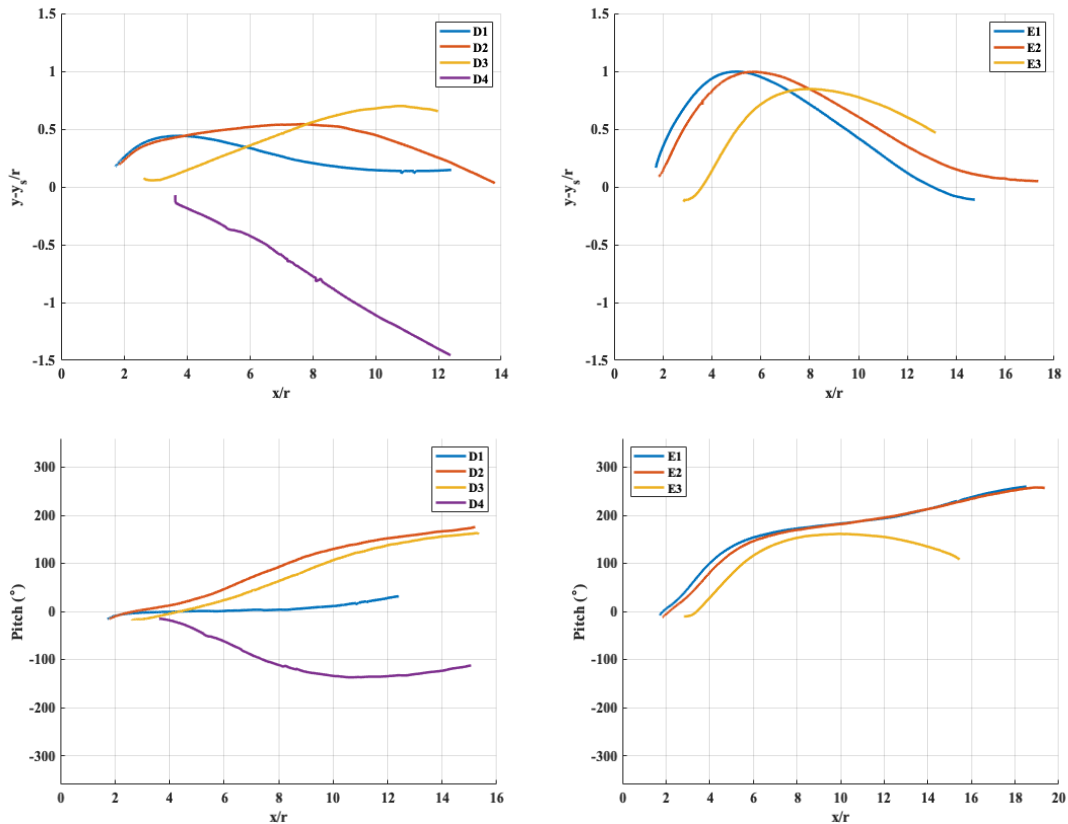


**Figure 4.5:** Normalized distance from shock center for Configuration D (Top Left) and E (Top Right). Pitch values of Configuration D (Bottom Left) and E (Bottom Right)

Minimal pitching allowed for stable shock-wave surfing to take place, resulting in a limited range of  $(y - y_s)/r$  values, varying only between 0.14 and 0.44 as seen in Figure 4.6. A comparison of the shock-wave surfing behavior exhibited by a sphere and the ellipsoid, D1, is shown in Figure 4.7.

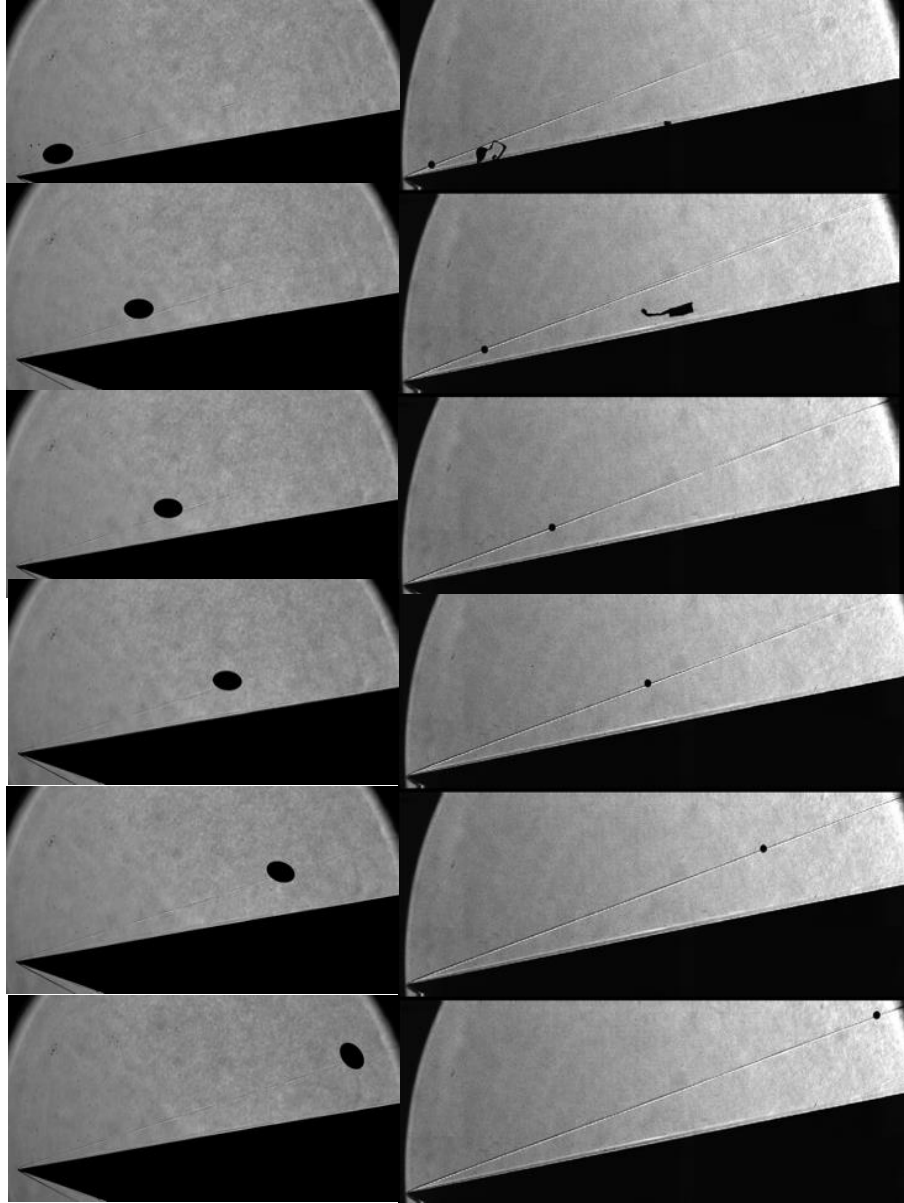


**Figure 4.6:** Shock surfing of an ellipsoid (left) and spherical (right) body

Configuration E3 initially experienced a shock impingement above the semi-major axis and subsequently underwent a total change in pitch of  $149.61^\circ$  in the clockwise direction. As the ellipsoid approached  $x/r = 10.68$ , the pitching motion diverted to the counterclockwise direction, decreasing the pitch angle by a total of  $51.83^\circ$ . Configuration D4 experienced a similar initial shock impingement; however, the motion upon separation now resulted in an opposite, counterclockwise moment, with a total pitch change of  $152.78^\circ$ . As the ellipsoid approached  $x/r = 10.80$ , the pitching motion yielded to the clockwise direction, decreasing the total rotation by  $24.69^\circ$ , before exiting the test section. Configuration D3, having the shock impingement closest to the ellipsoid's semi-major axis, showed likely surfing behavior upon separation as it exhibited a value of  $(y - y_s)/r \approx 0.07$  from  $x/r = 2.66$  to  $3.17$ . However, the expulsion distance progressively increased as the ellipsoid continued downstream, resulting in a maximum  $(y - y_s)/r$  value of  $0.70$  at  $x/r = 10.77$ , greater than all other tests shots in Configuration D.

### 4.3 Ellipsoid Dynamics

In Figure 4.8 we show the horizontal displacement versus time for each of the experiments; this was determined by the extracted x-values from the pose vector derived from the optical tracking code. The ellipsoids of Configuration D all show somewhat different displacements; however, E1 and E2 displayed almost identical displacement behavior as the ellipsoid traversed downstream. This observation is

consistent with their very similar separation trajectories mentioned in the previous section.

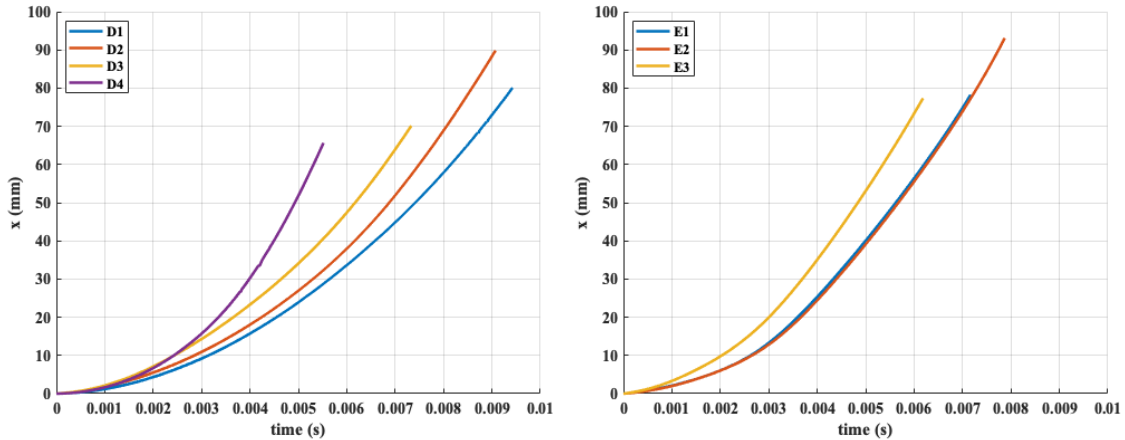


**Figure 4.7:** Horizontal displacement values derived from the optical tracking code of shots in Configuration D (left) and E (right)

The horizontal velocity, acceleration, and forces displayed in Figure 4.8 were derived from the horizontal displacement data using a moving regression method with additional polynomial fitting [36]; the raw (unfitted) data are provided in Appendix A2. Examining the data in Figure 4.8, we see that Ellipsoid D4 traversed downstream with the fastest speed, displaying the highest exiting velocity and acceleration of 27.81 m/s and 8,100 m/s<sup>2</sup>, respectively. The shock impinging above the ellipsoid’s semimajor axis resulted in the direct entrainment trajectory, causing D4 to experience an increased flow density inside the shock layer; additionally, the ellipsoid rotated so that it presented a large area to the oncoming flow. These two effects resulted in a greater force acting on the ellipsoid. This near-ramp boundary layer interaction is shown in Figure 4.9.

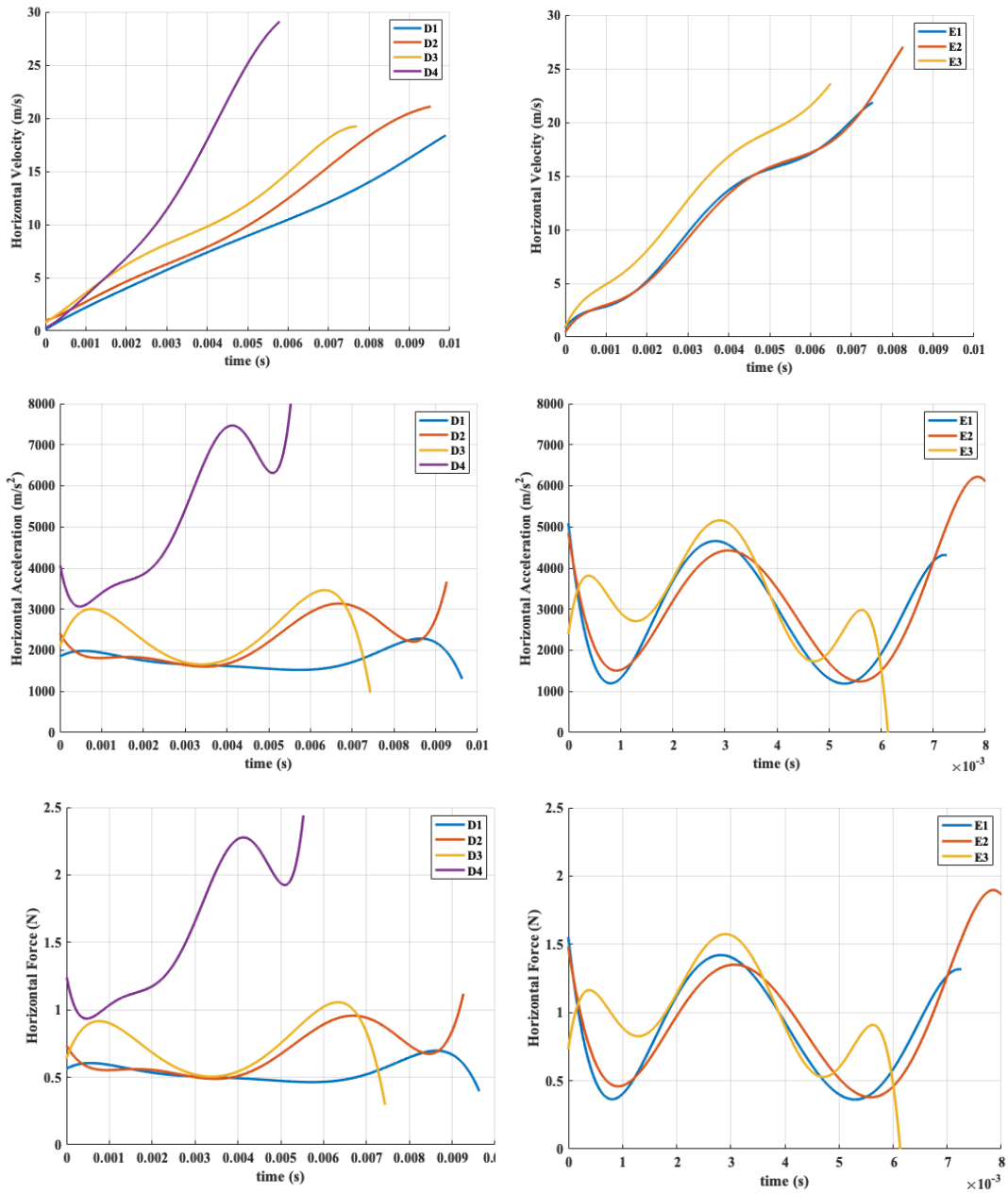


**Figure 4.8:** Horizontal velocity of Configuration D (top left) and E (top right). Horizontal acceleration of Configuration D (bottom left) and E (bottom right).

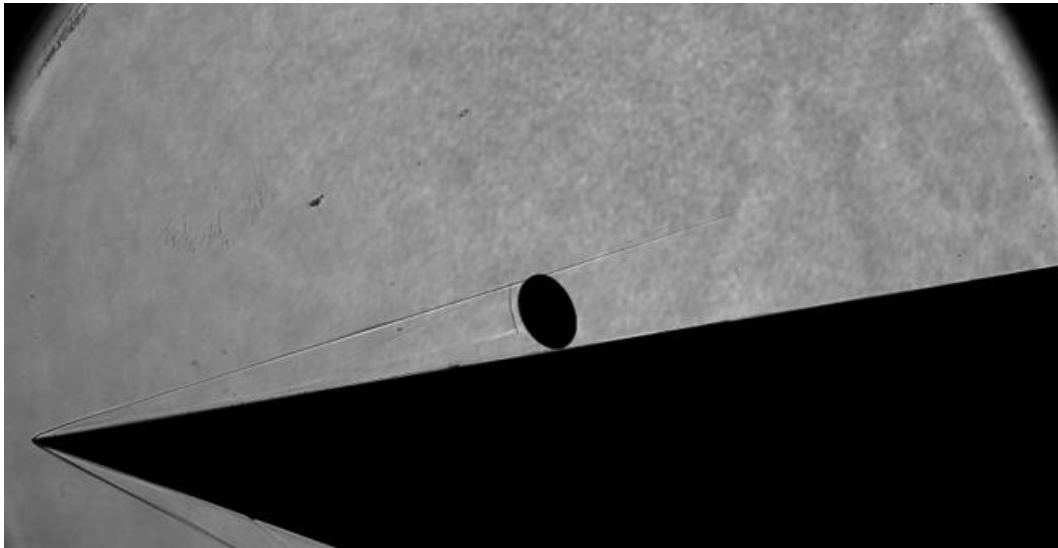


**Figure 4.9:** Near-ramp boundary layer interaction on Configuration D4 ellipsoid

Ellipsoid D1 experienced the lowest velocity and acceleration values during its shock-surfing trajectory. The maximum calculated velocity and acceleration values for D1 peaked at 18.40 m/s and 2,286 m/s<sup>2</sup>, respectively. Ellipsoids D2 and D3, having similar initial positions, converged in acceleration values at approximately 0.0035 seconds. At this point of the trajectory, each ellipsoid has completed its initial separation and is now experiencing an increased angular velocity. As expected, E1 and E2 displayed similar results in the velocity data, although the accelerations exhibited a larger discrepancy. To show this more concretely, Figure 4.10 compares the variability of velocity and acceleration, with the plotted curve representing the ratio of E2:E1 in each case.

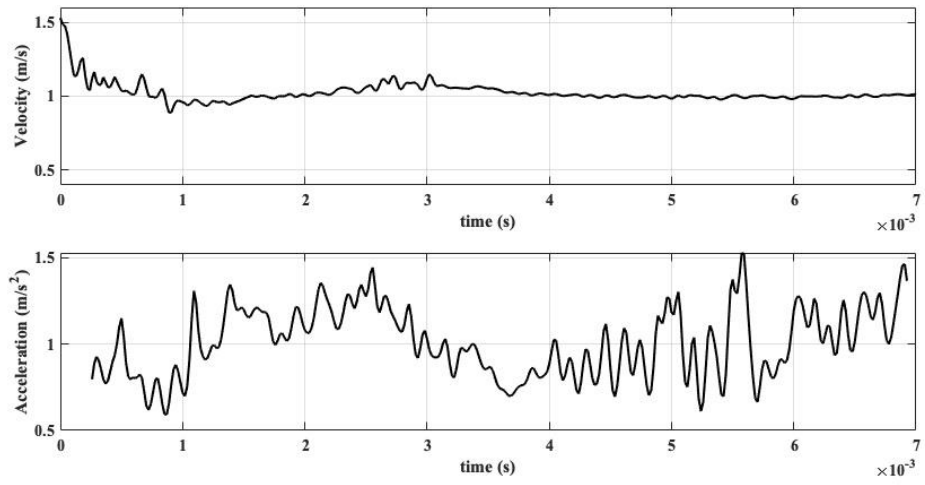


**Figure 4.10:** Comparison of convergence of velocity (Top) and acceleration (Bottom) values between E1 and E2

## Chapter 5: Computational Results

### 5.1 Computational Parameters

The computational case was designed to replicate the trajectory of at least one of the test shots from the experimental methods as closely as possible. The shock impingement was the driving variable for the ellipsoid trajectories in the experimental results and, therefore, was used to determine the configuration of the computational case. In the experimental results, a shock impingement below the centerline of the semi-major axis of Configuration D yielded two possible trajectory types: expulsion to surfing or shock surfing. The initial position of Configuration D1 was referenced to build the computational case, as the goal was to produce a shock impingement below the ellipsoid's semi-major axis. However, in the computational case, the ellipsoid could not rest on the ramp at any point in the simulation, causing a slight discrepancy in creating an identical initial position to that of Configuration D1. A very small gap (approximately 0.5 millimeters) between the ramp and ellipsoid was required to leave space for a few layers of volumetric grid cells from the ellipsoid's no slip boundary condition. This was necessary to produce satisfactory transients and reduce large flow gradients at the ramp-ellipsoid interface in the simulation. Therefore, the starting distance of the computational case was positioned further downstream to compensate for the vertical offset and produce a shock impingement below the semi-major axis. As a result, the ellipsoid for the computational case was positioned 15.5 mm away from the leading edge, with an initial pitch of  $-14.6^\circ$ , as shown in Figure 5.1.

The dimensions of the ellipsoid unstructured grid were identical to the ellipsoids belonging to Configuration D in the experimental methods. To replicate the experimental ellipsoid separating from the ramp, the freestream conditions were initialized with the ellipsoid's motion constrained. The flow initialized during a number of start-up iterations, and once they were completed, the ellipsoid was released.

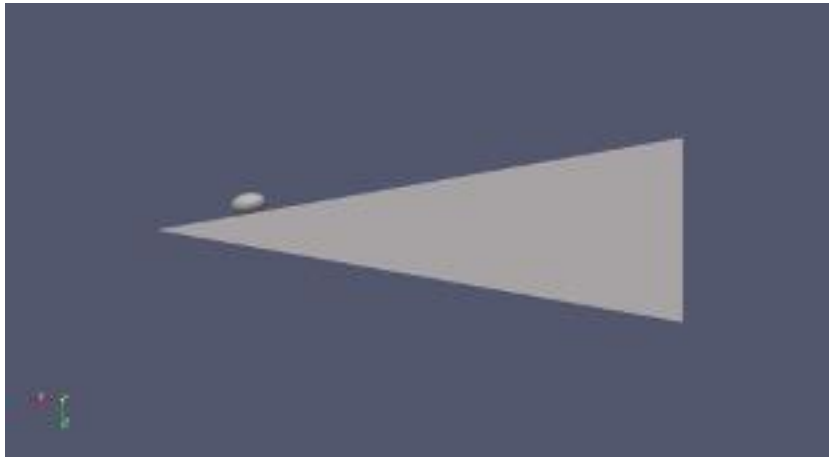


**Figure 5.1:** Visualization of the ellipsoid and ramp positioned in simulation before release

#### 5.1.1 Grid Refinement Study

To ensure an accurate simulation, a grid refinement study was performed to determine spatial convergence and grid dependency of the solution. Three levels of grids were present in the refinement study: Coarse, Medium, and Fine. Each unstructured grid was refined by a factor of  $1/\sqrt{2}$  using the Coarse grid as the baseline sizing. A summary of the Coarse grid sizing is found in Table 3.1. Once the unstructured grids were refined in Capstone, the Cartesian structured overset was then

automated by Kestrel. A summary of the refinement levels are found in Tables 5.1-5.3, and the physical grids are visualized in Figures 5.2 and 5.3.

Cartesian Overset:

Grid Level	Total Cells
Coarse	31,885,772
Medium	71,050,739
Fine	82,749,762

**Table 5.1:** Cell count of the Cartesian overset for each grid level in the refinement study

Surface Faces:

<b>Ellipsoid</b>			
	Triangles	Quadrilaterals	Total Faces
Coarse	1,633,880	1,726,396	3,360,276
Medium	15,217,986	0	15,217,986
Fine	7,928,395	6,523,861	14,452,256

<b>Ramp</b>			
	Triangles	Quadrilaterals	Total Faces
Coarse	8,166,417	0	8,166,417
Medium	3,588,613	3,328,338	6,916,951
Fine	7,084,486	6,409,087	13,493,573

**Table 5.2:** Total faces on the unstructured grids for each grid level in the refinement study

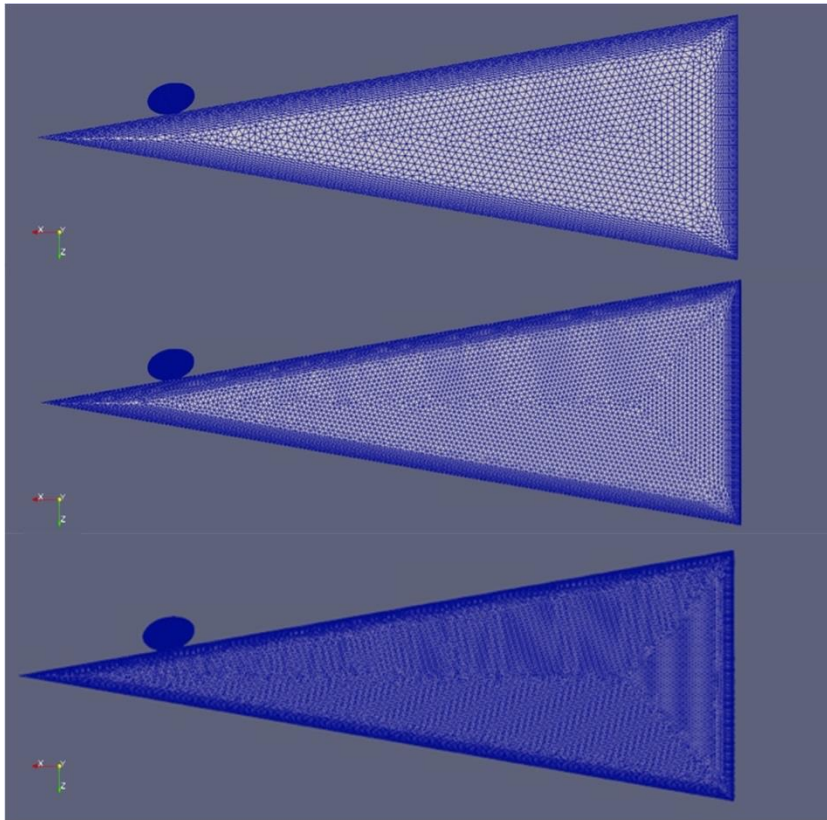
Volume Cells:

<b>Ellipsoid</b>				
	Tetrahedrals	Prisms	Pyramids	Total Cells
Coarse	219,430	1,148,915	6,047	1,374,392
Medium	7,575,440	0	0	7,575,440
Fine	1,708,078	4,342,293	20,843	6,071,214

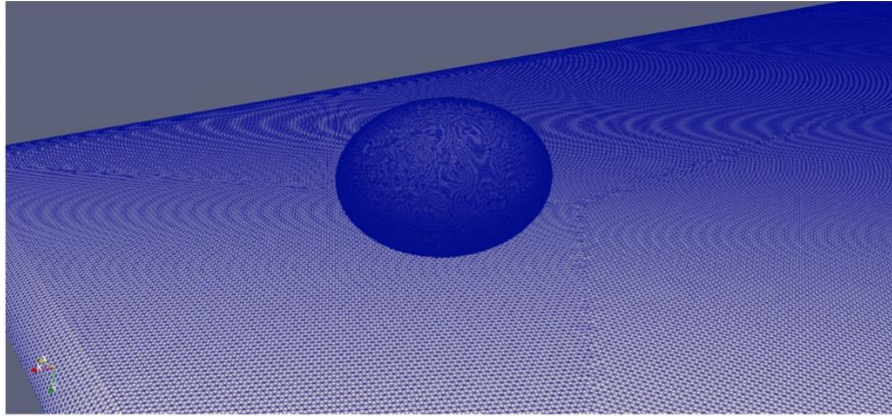
  

<b>Ramp</b>				
	Tetrahedrals	Prisms	Pyramids	Total Cells
Coarse	4,054,678	0	0	4,054,678
Medium	603,070	2,210,612	24,840	2,838,522
Fine	1,270,186	4,259,877	41,243	5,570,406

**Table 5.3:** Total volume cells on the unstructured grids for each grid level in the refinement study



**Figure 5.2:** Coarse (top), Medium (middle), and Fine (bottom) unstructured grids produced from grid refinement study



**Figure 5.3:** Orthogonal view of the starting position of the ellipsoid for the computational Fine grid

The refinement factor of  $1/\sqrt{2}$  sized all features (global sizing, topos sizing, curvature sizing, edge boundary layer, and volumetric boundary layer) of the grid at a uniform rate. As the grids were generated, Capstone applied an iterative optimization check to determine the best combination of triangles and quadrilaterals for the surface faces and tetrahedrals, prisms, and pyramids for the volume cells. For the ellipsoid, the Medium grid contained more surface faces and volume cells than the Fine grid. Similarly, for the ramp, the Coarse grid contained more surface faces and volume cells than the Medium grid. Although this is counterintuitive to grid refinement, it is important to note that an increase in the quantity of cells alone is not a direct correlation of refinement. The Coarse grid for the ramp and the Medium grid for the ellipsoid contain only triangles and tetrahedrals, void of all other face and cell geometries. A combination of geometries often increases the quality of contour resolution in the grid.

At each grid level, the ellipsoid was simulated shedding from the ramp and a convergence check was performed using the coefficient of lift values.

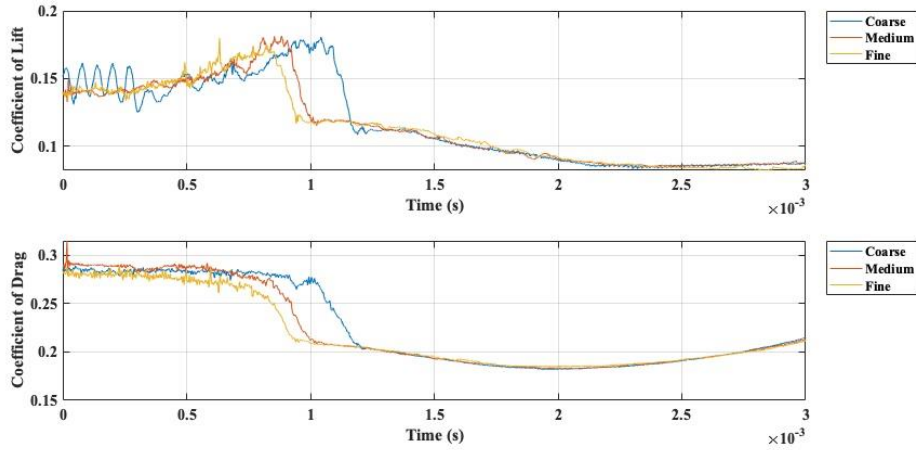


**Figure 5.4:** Comparison of coefficients of Lift (top) and Drag (bottom) between the Coarse, Medium, and Fine grid

The calculated lift and drag coefficients during the first 3 milliseconds of the simulation for each of the refinement levels are shown in Figure 5.4. For each grid level, instability consistently appeared in the first .001 seconds of the solution. Unsteadiness at the start of a simulation could be caused by a number of factors (i.e., startup mechanics, startup iterations, inadequate timestep, impact from the constraint, etc.). Consequently, errors can propagate downstream and, for this reason, a stability analysis was completed to determine if the solution adequately initialized before the ellipsoid was released from the constraint.

### 5.1.2 Sensitivity Analysis

Upon completing the convergence check for the coarse, medium and fine grid, it was deemed necessary to conduct a stability check on the solution. Here, the computational variable of interest was the number of startup iterations the simulation performed before releasing the ellipsoid from the constraint. Startup iterations allows a period in which the flow transients can first initialize, and then adequately subside before performing the first timestep. For example, if a simulation is assigned 2000 startup iterations, the simulation will initialize the freestream conditions at iteration 1, but will not begin any actions or initialize the first timestep until iteration 2001. To evaluate the effect of the number of startup iterations on the stability of the solution, an extra coarse grid was generated and employed to save computational resources during the computation. The Extra Coarse grid was reduced in resolution from the baseline Coarse grid by the refinement factor of  $1/\sqrt{2}$  and the parameters are found in Table 5.4.

	Total Faces and Cells
Ellipsoid	3,872,572
Ramp	4,219,318
Cartesian	34,809,780

**Table 5.4:** Total faces and cells for the extra coarse grid

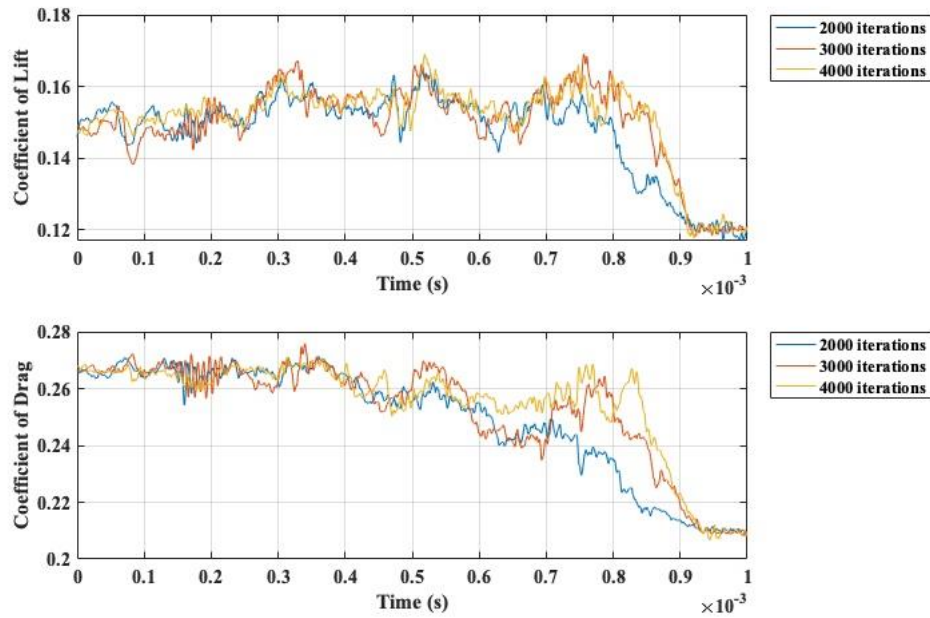


**Figure 5.5:** Comparison of coefficients of Lift (top) and Drag (bottom) between with differing start-up iterations

Three sensitivity analyses were performed on the extra coarse grid with 2000, 3000, and 4000 start-up iterations, shown in Figure 5.5. The figure shows the solution after the startup iterations are complete, essentially starting at the first timestep. The results in Figure 5.5 shows convergence between 3000 and 4000 start-up iterations, with very minimal differences between the two. Therefore, it was concluded that an increase in start-up iterations could provide more steadiness to the solution but in this case, it is not the driving factor for a steadier solution.

## 5.2 Kestrel Comparison

### 5.2.1 Physical Data Validation

Although the fine grid provided greater grid resolution, the solution was relatively unsteady (See Figure 5.4) after release of the ellipsoid compared to the medium and coarse grid. Therefore, the data generated from the medium grid simulation was used for all analysis presented in this section. The parameters for medium grid domain are found in Table 5.5 and visualizations of the grid are shown in Figure 5.6. The value of total cells and faces in Table 5.5 represents all cells and faces of the unstructured grids and structured Cartesian grid referenced in Table 5.1, 5.2, and 5.3. Kestrel performed the simulation at a timestep of 5E-08 seconds per iteration, requiring 123,294 iterations and 7,872 CPU hours to complete.

Length (m)	Width (m)	Height (m)	Total Cells and Faces (m)
0.4604	0.2762	0.2755	1.04E+08

**Table 5.5** Computational domain sizing for the medium Grid

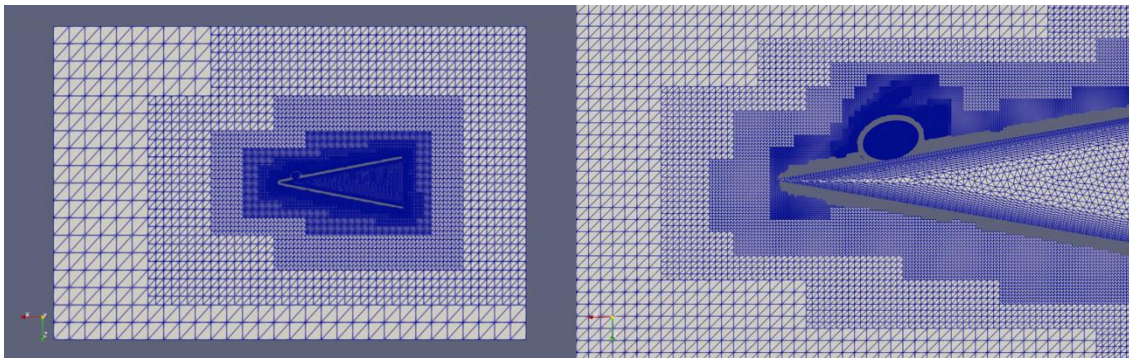


**Figure 5.6:** (Left) Total domain view of Medium computational grid. (Right) Adaptive grid/mesh refinement around ramp generated shock.

As previously mentioned in Section 5.1, the initial position was chosen to produce a shock impingement representative of Configuration D1 (see Figure A1.1), just below the centerline of the semi-major axis. However, in Figure 5.7, as represented by the localized region of high pressure at its leading edge, the initial shock impingement appeared much closer to that of Configuration D3 (see Figure A1.3).

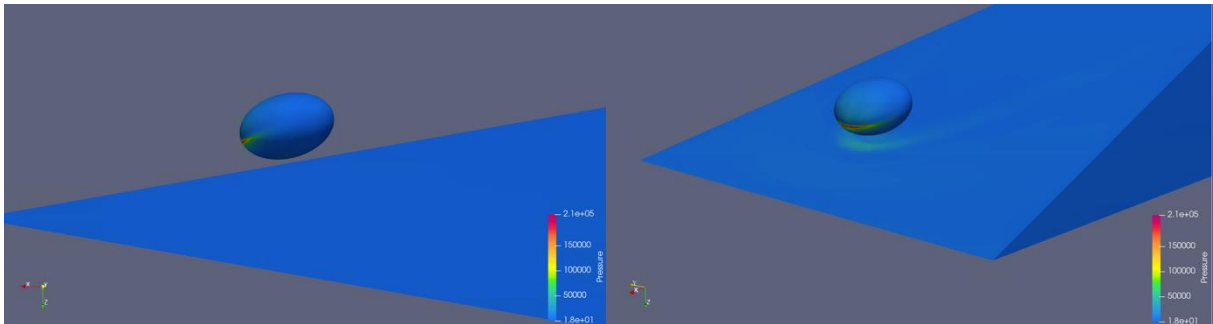


**Figure 5.7:** XZ plane (left) and orthogonal view (right) of the initial shock impingement on the ellipsoid from the numerical simulation.

Additionally, the flow visualization of the computational case is found in Figure 5.8, where the ramp generated oblique shock and bow shock acting on the ellipsoid are now visualized by a density (with plotted limits 0 to  $0.059 \text{ kg/m}^3$ ). Similar ellipsoid behavior to that of the experimental results is seen here, with the impinging oblique shock causing the ellipsoid to be ejected away from the shock layer upon separation. As the ellipsoid continues its pitching motion downstream, it re-approaches the shock layer with its semi-major axis approaching a parallel orientation with the shock. It was expected to see a similar trajectory type similar to those produced by Configuration D1,

D2, and/or D3 due to the location of the initial shock impingement. A direct comparison of the computational and experimental ellipsoid visualization is shown in Figure 5.9.

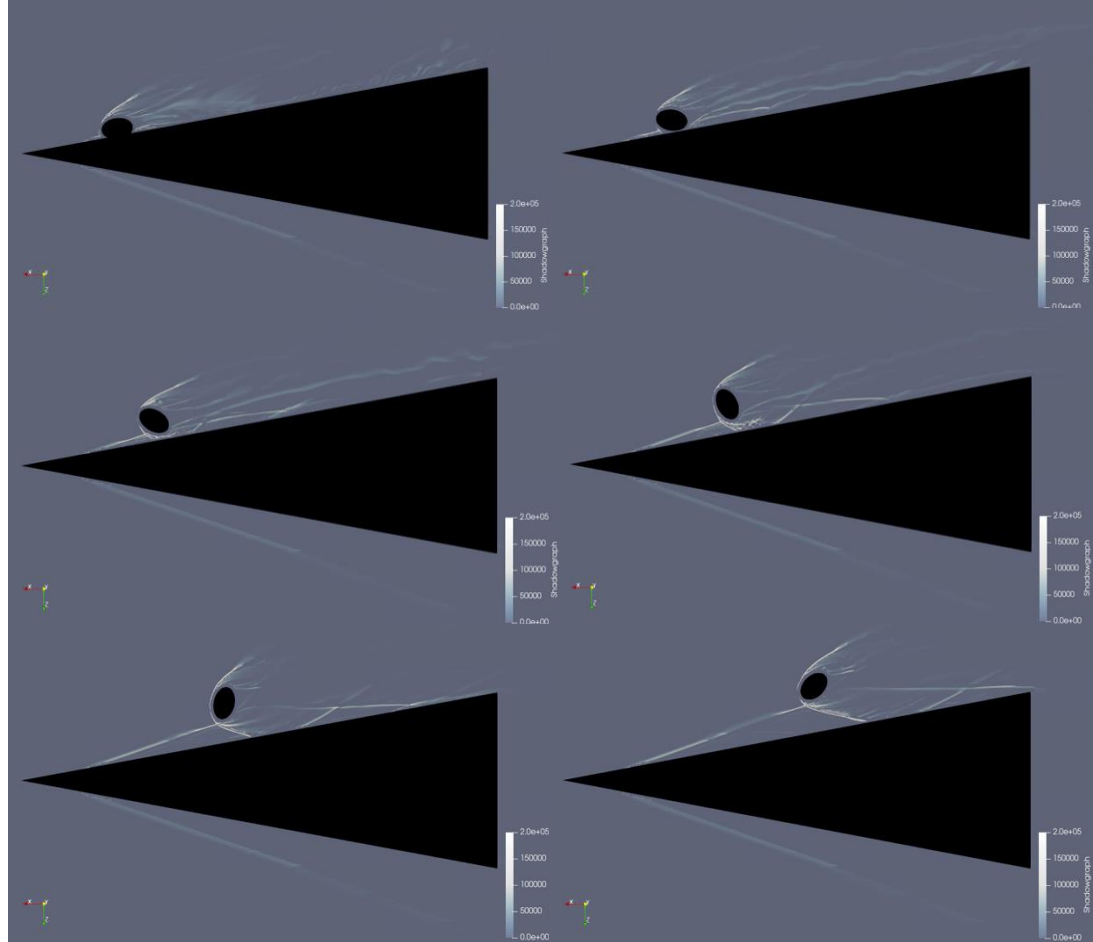


**Figure 5.8:** Flow visualization of the ramp generated shock and ellipsoid bow shock

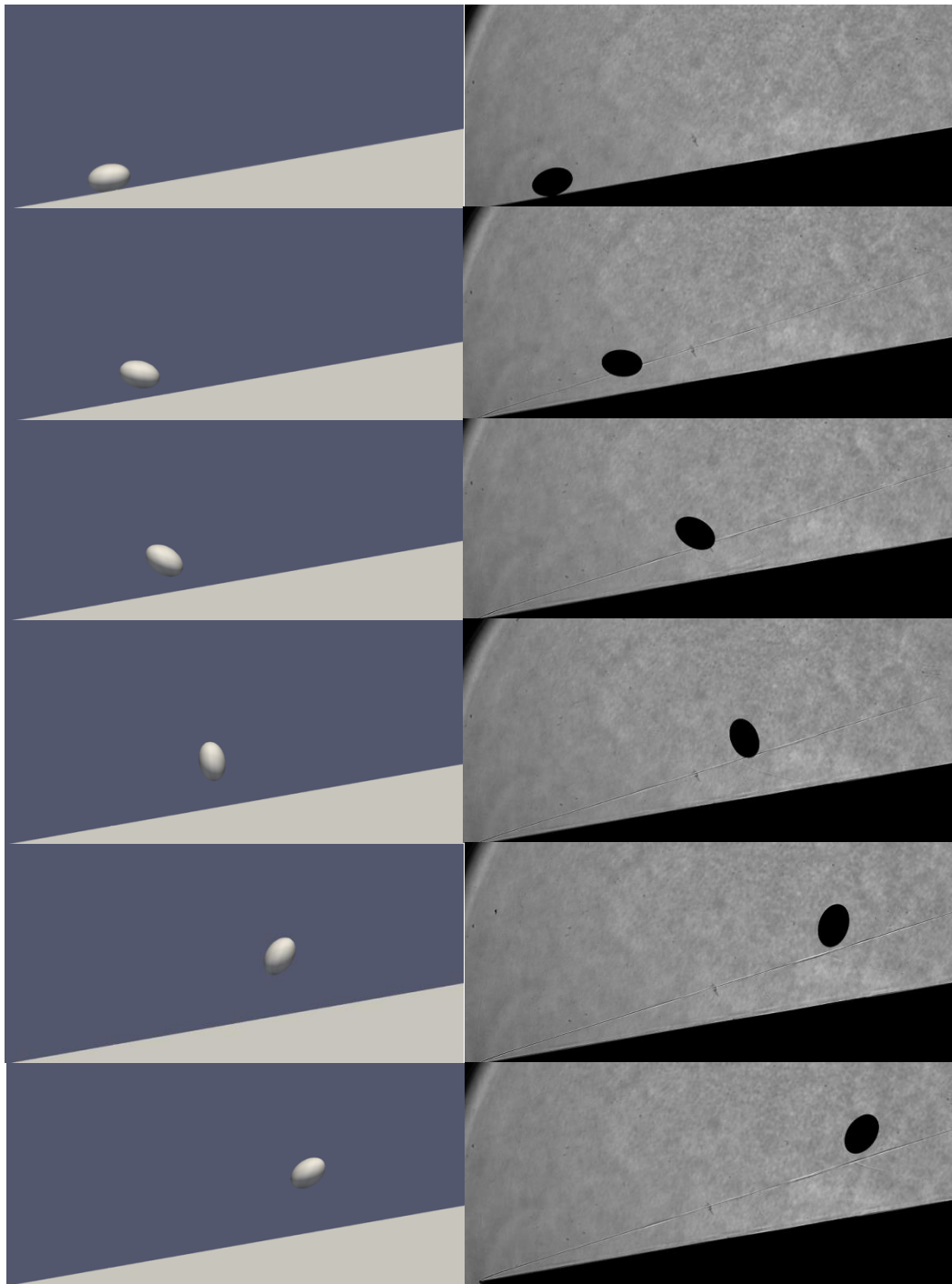


**Figure 5.9:** Resulting trajectory from an initial shock impingement below the semi-major axis of the ellipsoid for the computational case (left images) and the experimental results for Configuration D3 (right images).

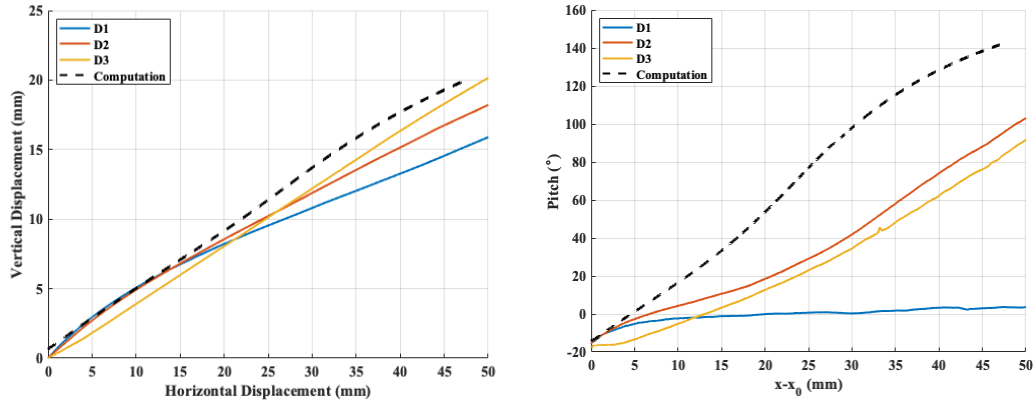


**Figure 5.10:** Displacement (left) and pitch (right) of the computational case compared to the ellipsoids of Configuration D.

To further compare the computational results with the trajectories of Configuration D, the computational displacement and pitch are shown in Figure 5.10 together with all corresponding experimental results from Configuration D. Overall, the simulation predicts similar  $x$  vs  $y$  displacement behavior to those of the experimental ellipsoids. The numerical simulation converges towards the displacement behavior of Configurations D1 and D2 for approximately 15 mm before diverging. This is expected because the initial position of the computational case was the most comparable to D1 and D2. Interestingly, the computation follows the displacement curve of Configuration D3 in Figure 5.10, however, shifted by a positive factor of  $\sim 1.08$ - $1.2$  throughout the entirety of the trajectory. Although, the qualitative behavior of the pitching motion is similar to Configurations D3, Figure 5.10 shows the computational pitch increases more rapidly than the experimental cases.

Continuing with the computational evaluation, we now examine the horizontal displacement, horizontal velocity, horizontal acceleration, and horizontal force

magnitude as functions of time. Figure 5.11 shows that the simulation follows the experimental results of Configuration D3 for approximately .003 seconds before deviating. As mentioned in Section 4.3, this is the point where the ellipsoid has completed its initial separation and is increasing in the rate at which it pitches. Despite this initial divergence at .003 seconds, the simulation appears to again converge to the horizontal displacement curve for D3 further downstream. The velocity of the computation appears similar to Configuration D1 and D2 between .001 and .003 seconds, however, diverges after .003 seconds. The velocity continues to increase as it reaches 16.76 m/s at .006 seconds, a maximum velocity greater than Configuration D1, D2, and D3.

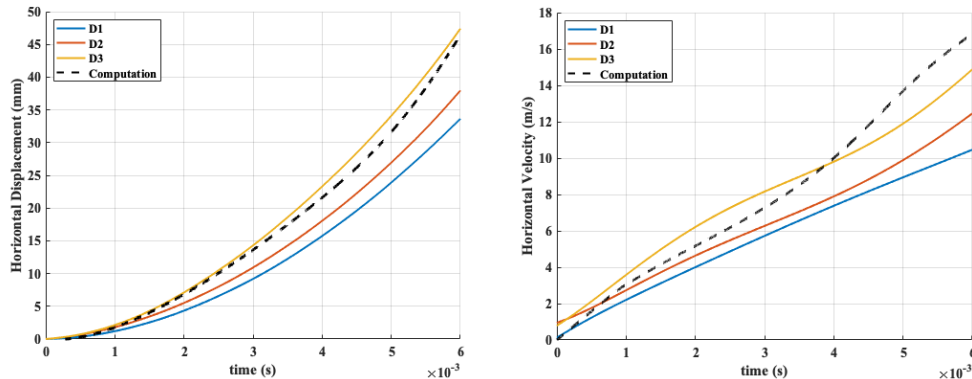


**Figure 5.11:** Horizontal displacement (left) and Horizontal velocity (right) comparison of the numerical simulation and experimental results Configuration D ellipsoids.

Similarly, comparisons of the horizontal accelerations and forces are shown in Figure 5.12. Here we see a larger variance when comparing the computational and experimental results. The simulation exhibits a greater acceleration at the start of the

ellipsoid motion, which affects the solution downstream. This may be partially due to the fact that the ellipsoid never actually rested on the ramp to leave room for the no slip boundary condition and avoid intersecting of the grids – note, for example, that the ellipsoid for Configuration D3 (which best matches the computational trajectory) experiences a rapid increase in force as it separates from the ramp. The simulated ellipsoid reaches a maximum acceleration and force of  $3,832 \text{ m/s}^2$  and  $1.17 \text{ N}$  at  $0.0047$  seconds, respectively, whereas in Configuration D3 the corresponding values are  $3,462 \text{ m/s}^2$  and  $1.056 \text{ N}$  at  $0.0064$  seconds, respectively.

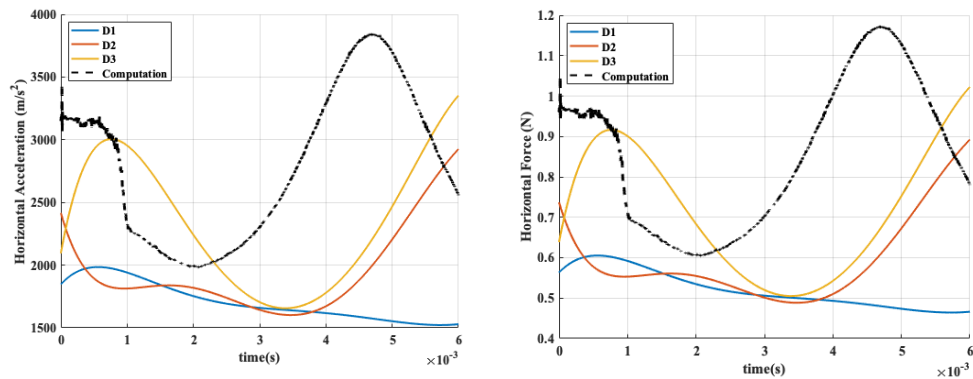


**Figure 5.12:** Horizontal acceleration (left) and forces (right) comparison of the numerical simulation and experimental results Configuration D ellipsoids.

## Chapter 6: Summary and Conclusion

### 6.1 Summary and Conclusions

In the body of work presented, we have evaluated and characterized the separation dynamics of an ellipsoid detaching from a two-dimensional  $10^\circ$  ramp in Mach 6 flow. Building upon a previous body of work involving spherical bodies, the effects of a pitch variable was introduced, and the body's motion was carefully studied experimentally and computationally. Experimental data allowed for a fidelity assessment of the predictive capabilities of computational methods. Important findings and conclusions are detailed in the following section.

#### 6.1.1 Summary of Experimental Results

The first part of this study was conducted experimentally in the HyperTERP shock tunnel. Twenty-four ellipsoids in total were tested, and seven of the ellipsoid trajectories were closely examined with an optical tracking algorithm. Two different configurations were evaluated. Each ellipsoid was positioned to purposely experience a desired shock impingement, in turn affecting the behavior of the ellipsoid in its initial separation from the ramp. Three trajectory types were observed during testing: expulsion to surfing, shock surfing, and direct entrainment. Despite the differences in shock impingement, the ellipsoids belonging to Configuration E resulted in only the expulsion to surfing trajectory type. In contrast, all three trajectory types appeared in the results of the ellipsoids belonging to Configuration D. The ellipsoids belonging to Configuration E contained a flatter geometry than those of Configuration D, in turn,

experiencing more lift and pitching at the start of the motion. To compare, the maximum total rotation an ellipsoid experienced in Configuration D was  $150^\circ$ , whereas Configuration E produced a maximum of  $235^\circ$ .

An important factor revealed in these experiments was the relation of the pitching motion to the velocity and acceleration as the ellipsoidal body traversed downstream. The one ellipsoid to experience direct entrainment in the shock layer exhibited the highest velocity and acceleration values. The shock impingement above the semi-major axis caused a counterclockwise pitching motion on the ellipsoid, resulting in the direct entrainment trajectory. Within the shock layer, the ellipsoid rapidly gained momentum due to the increased dynamic pressure and the orientation induced by the near-wall interaction (which led to a large cross-sectional area being exposed to the flow), resulting in an increased velocity and acceleration. Conversely, for an ellipsoid that experienced stable shock surfing, the reduction in pitching motion caused the ellipsoid to experience less momentum as it travelled downstream; it thus exhibited the lowest velocity and acceleration values of all the experimental cases.

### 6.1.2 Summary of Computational Results

The purpose of employing computational methods was to evaluate Kestrel's ability to predict NBOB (near-body/off-body) flow problems with a high level of accuracy. The computational flow problem was implemented to simulate the trajectories found in the ellipsoids with the maximum aspect ratios in the experimental results. Positioned 15.5 mm (non-dimensionally, 2.067) from the ramp's leading edge with an initial pitch of  $14.6^\circ$  (i.e.,  $4.6^\circ$  relative nose-down to the ramp), the intent was

to produce an initial shock impingement just below the semi-major axis. The flow was initialized by the freestream conditions derived in the experiments, with the simulation constraining the ellipsoid motion for a duration of 2000 startup iterations to allow the flow to be established. Once the startup iterations were completed, the ellipsoid was released and could fly freely in response to the experienced forces. The derived trajectory showed that the computation was comparable to the trajectories found in experimental results.

There was, however, considerable variation in the velocity and acceleration compared to experimental results. The simulation generated overall greater velocities and accelerations than those found in the experimental results. One factor that may have contributed to this result is the initial positioning of the ellipsoid. In order to initialize the flow problem in Kestrel, SAMAir (the NBOB solver) required the ellipsoid to avoid any contact with the ramp. For this reason, the ellipsoid was positioned with an initial vertical offset and never rested on the ramp in the beginning of the simulation. This affected the velocity and acceleration, as the forces are very sensitive to the exact initial position of shock impingement. A refinement study showed that the simulation was very sensitive to the start-up mechanics as errors propagated later in the solution.

In this study, the steadiness of the solution in the first .001 seconds showed to be less than ideal, which could have caused inconsistencies in the prediction of the velocity and acceleration values downstream. Each grid level in the refinement study showed unstable lift and drag coefficients, and horizontal acceleration and forces in the first .001 seconds of the dynamics of the ellipsoid. The sensitivity analysis showed that

increasing the number of startup iterations did not have a major impact on the steadiness of the solution. The reason of the unsteadiness could be of a physical and/or numerical origin. However, the analysis required to conclusively prove this is beyond the scope of this work.

It is important to note some of the computational challenges encountered in this study, as the purpose of employing computational methods was to validate the accuracy of NAVAIR's fixed-wing hypersonic flow solver. A summary of two notable challenges are detailed below:

- Originally, SAMAir would not initialize and caused immediate termination of the solution. Upon investigation, it was found that an error existed in the program that defined the effective fluid heat transfer coefficient. The Prandtl number was not properly initialized and was defined as a value of zero. This body of work allowed this error to be discovered, fixed, and the programming changes will be updated in the next revision of Kestrel.
- In the sensitivity convergence study, there was a problem identified in the adaptive grid/mesh refinement upon initialization. As an initial refinement level of the Cartesian grid was generated by Kestrel/SAMAir, it caused issues in the domain connectivity between the Cartesian grid and the ramp and ellipsoid no-slip boundary conditions, as the cell size gradient was too large for some of the computations with higher resolution. Several measures were employed to mitigate this issue. The initial refinement iteration was increased and the timestep was reduced. Although this did allow for the simulation to initialize,

the computation remained unstable and eventually terminated. CREATE-AV quality assurance team members believe this to be an error in SAMAir, leaving this an area for further investigation.

## 6.2 Academic and Technical Contributions

This body of work contributed to the field of hypersonic aerodynamics by:

- Developing case studies for applications concerning store separation and involuntary debris detachment from leading edges in hypersonic flight,
- Evaluating and characterizing trends in the separation behavior of a body in hypersonic flight, and
- Improving the DoD's prediction capabilities for NBOB flow problems by validating numerical simulations with data generated by experimental results.

## 6.3 Recommendation for Future Work

The work presented herein built off a previous body of work, and the same notion is considered moving forward. Possible areas of future work are detailed as follows:

- As the pitch variable was introduced in this study, future work could potentially study geometries that introduce yaw and/or roll. This will provide a more realistic examination for case studies of debris detachment from leading edges as the geometry of debris is less likely to be dimensionally uniform in any plane,

- Heat transfer and thermal management will always be a main concern for leading edges in hypersonic flight. The examination of heat fluxes during the separation of a spherical or ellipsoidal body could provide greater insight into not only the flight dynamics but also the material survivability and structural integrity of a hypersonic vehicle, and
- Effects of the near-ramp boundary layer on the motion of an ellipsoid with direct entrainment trajectories should be further investigated.

# Appendices

## A1: Shadowgraph images of Ellipsoids Trajectories

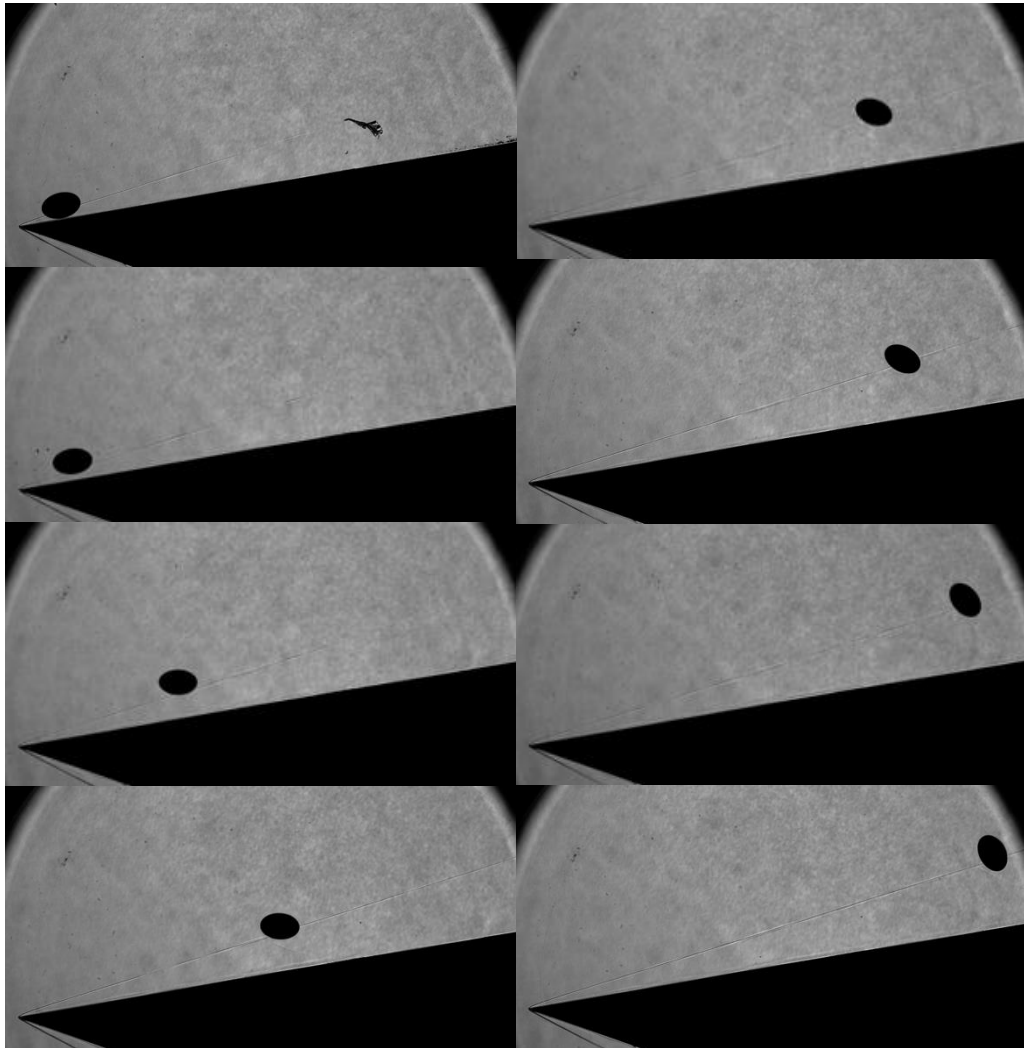


**Figure A1.1:** Shadowgraph images of Configuration D1

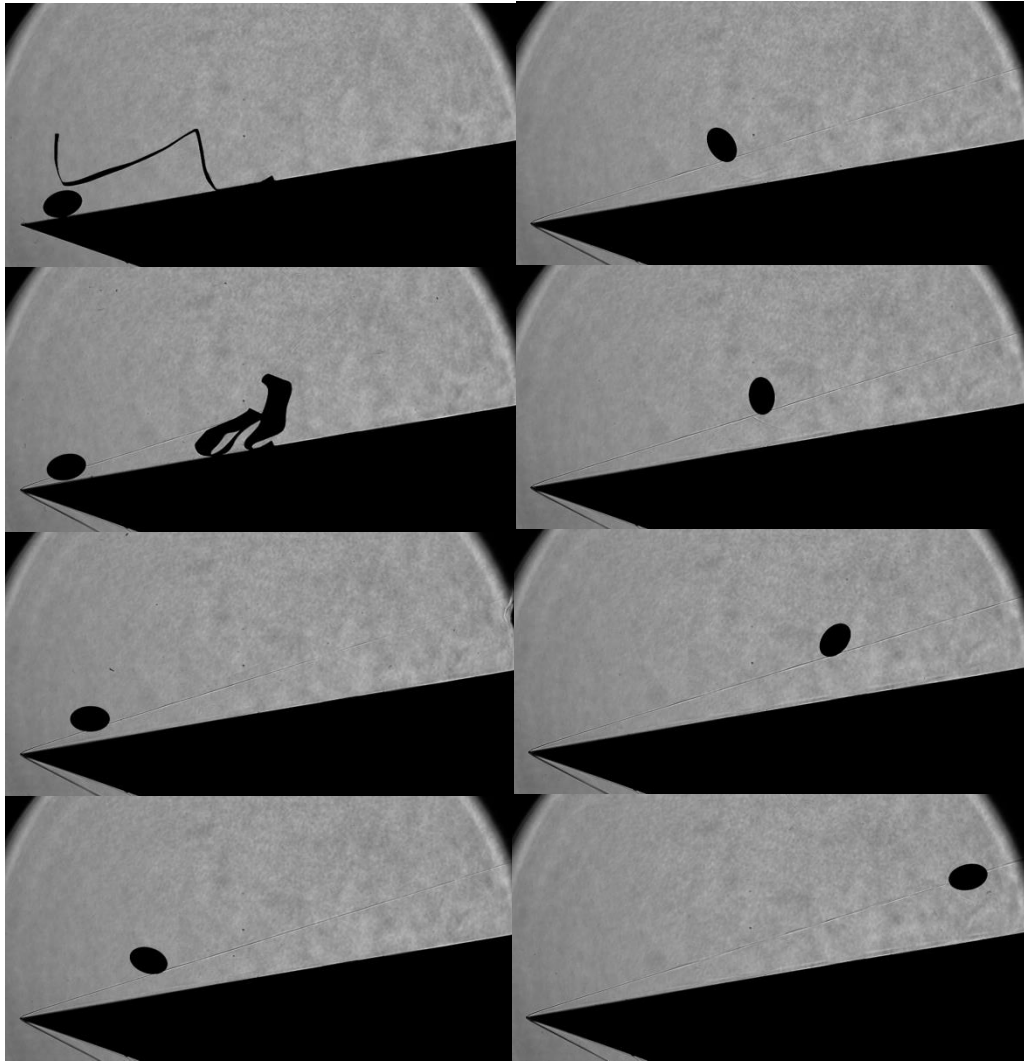


**Figure A1.2:** Shadowgraph images of Configuration D2

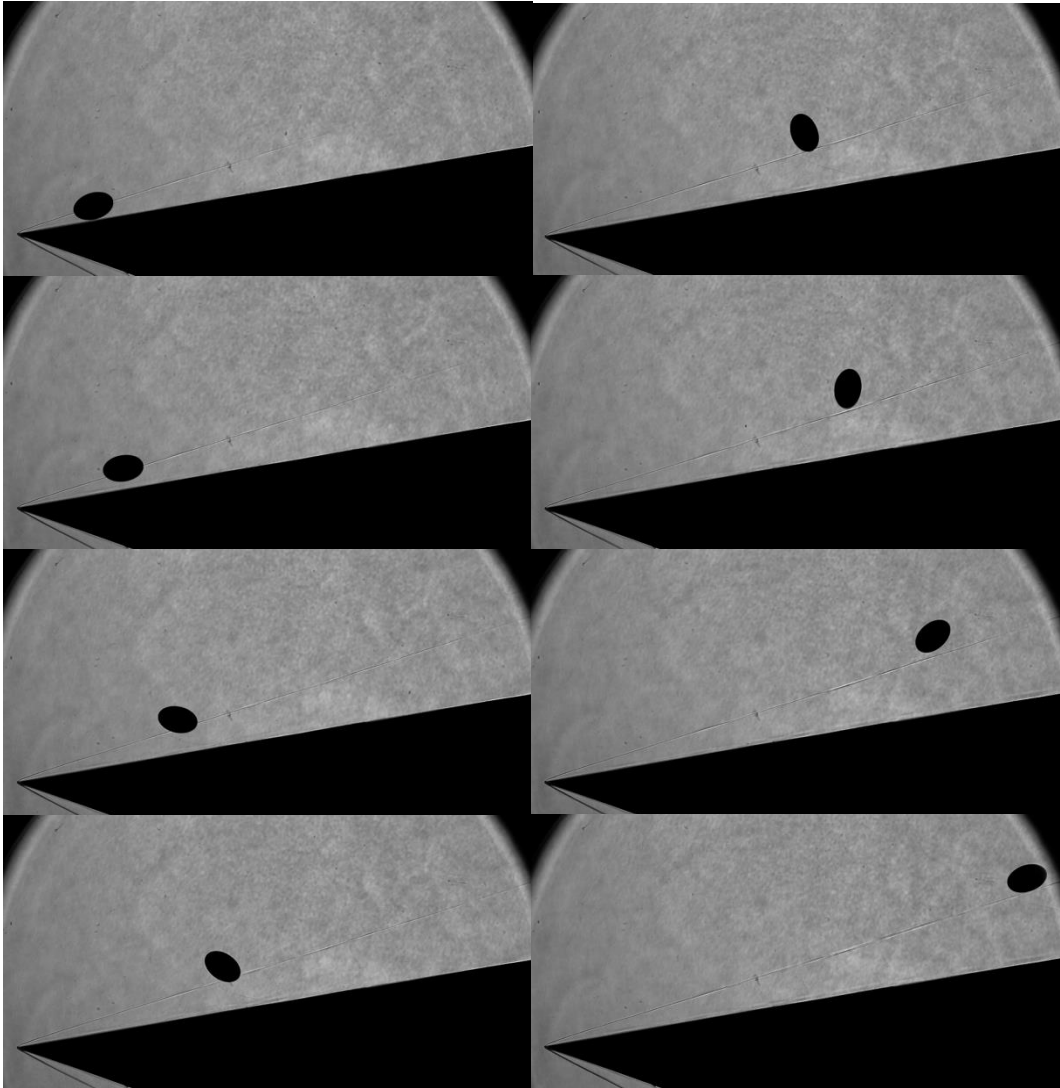


**Figure A1.3:** Shadowgraph images of Configuration D3

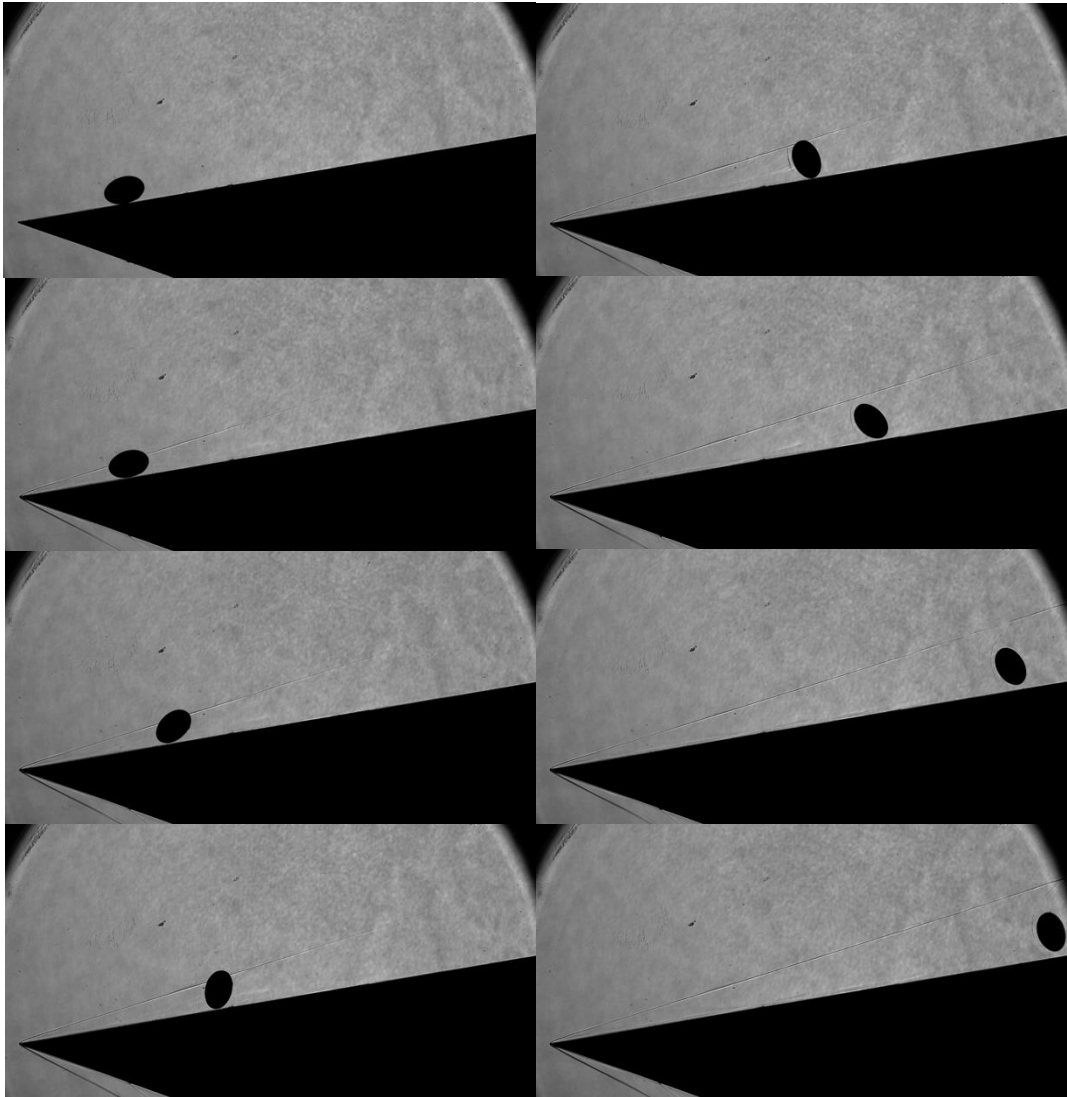


**Figure A1.4:** Shadowgraph images of Configuration D4

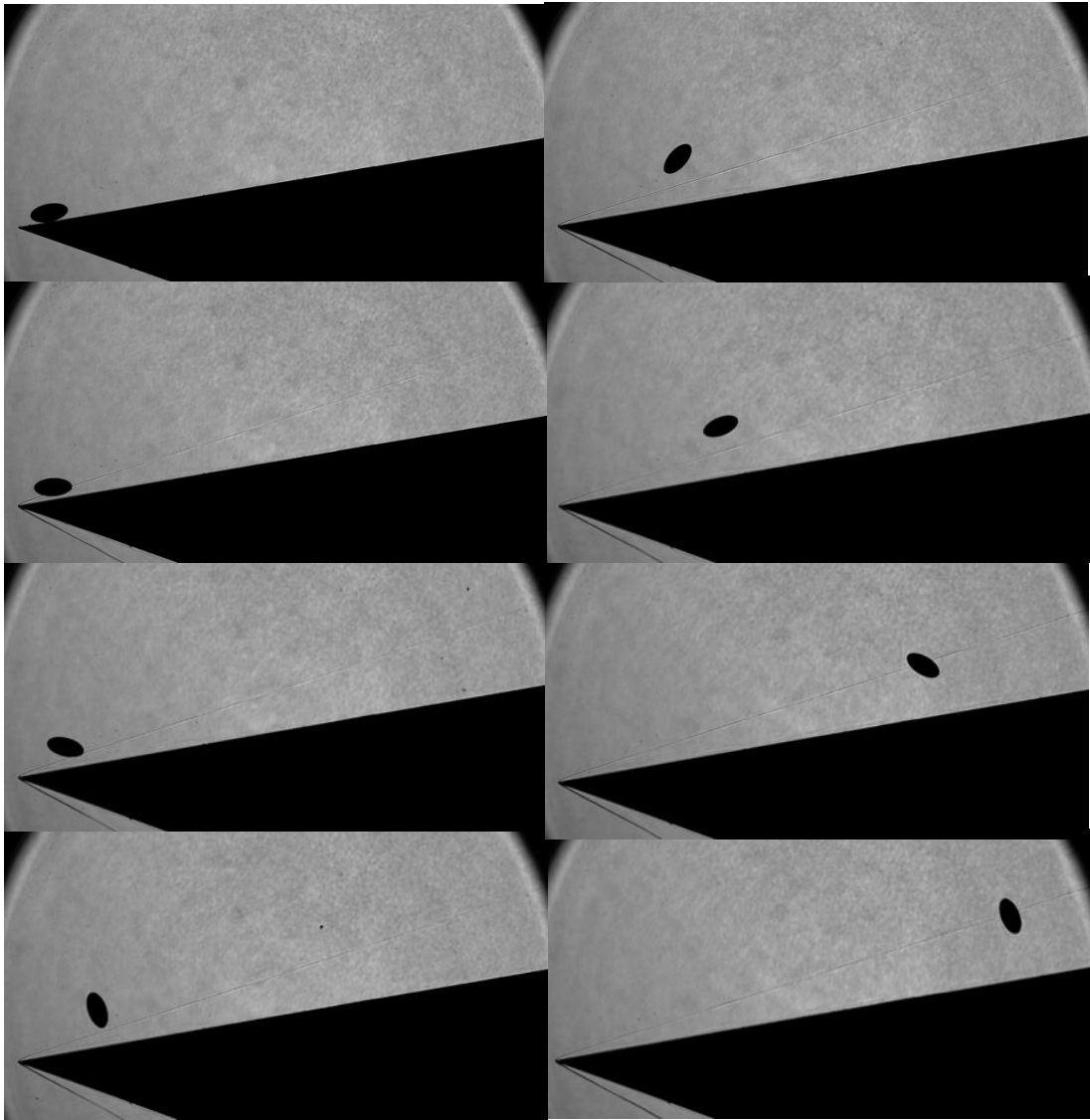


**Figure A1.5:** Shadowgraph images of Configuration E1

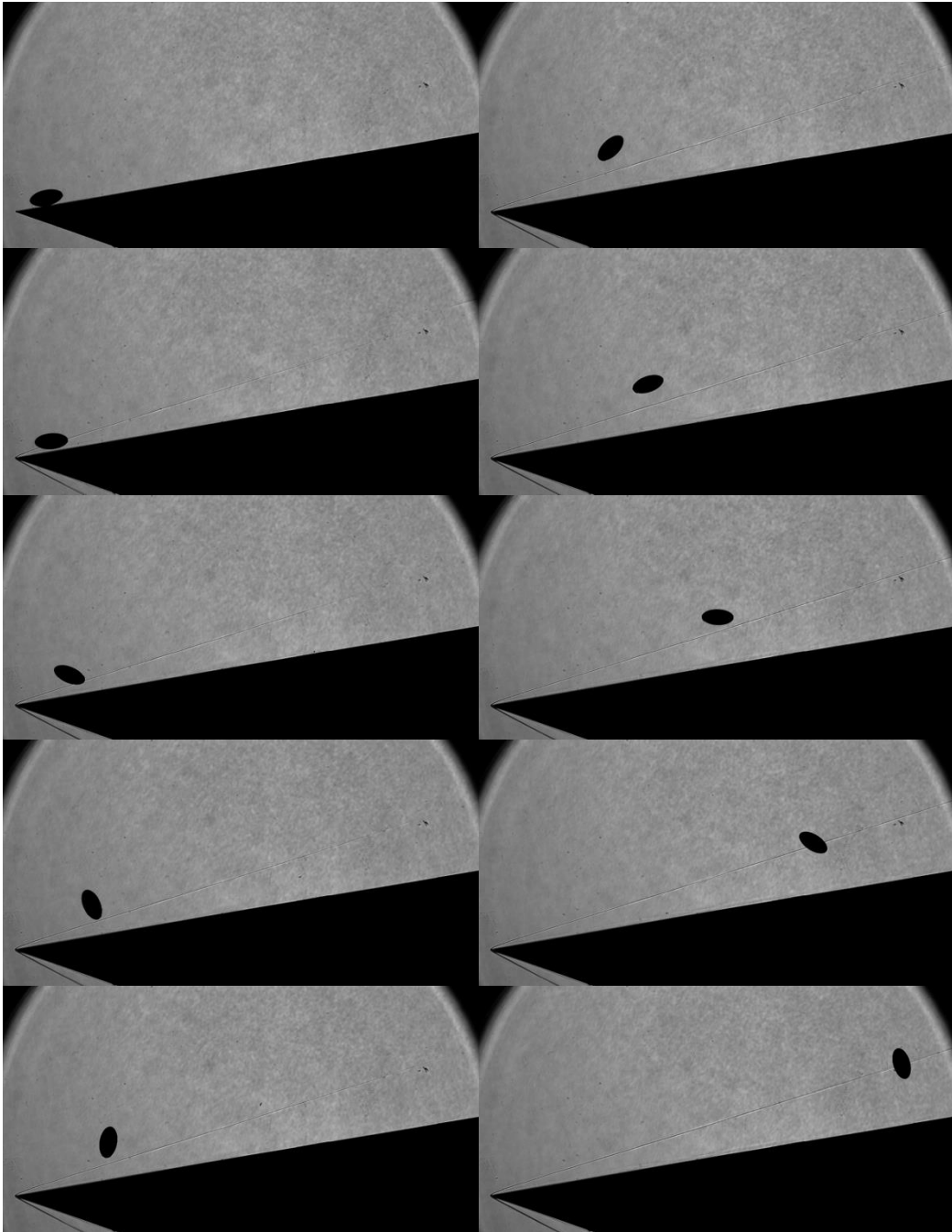


**Figure A1.6:** Shadowgraph images of Configuration E2

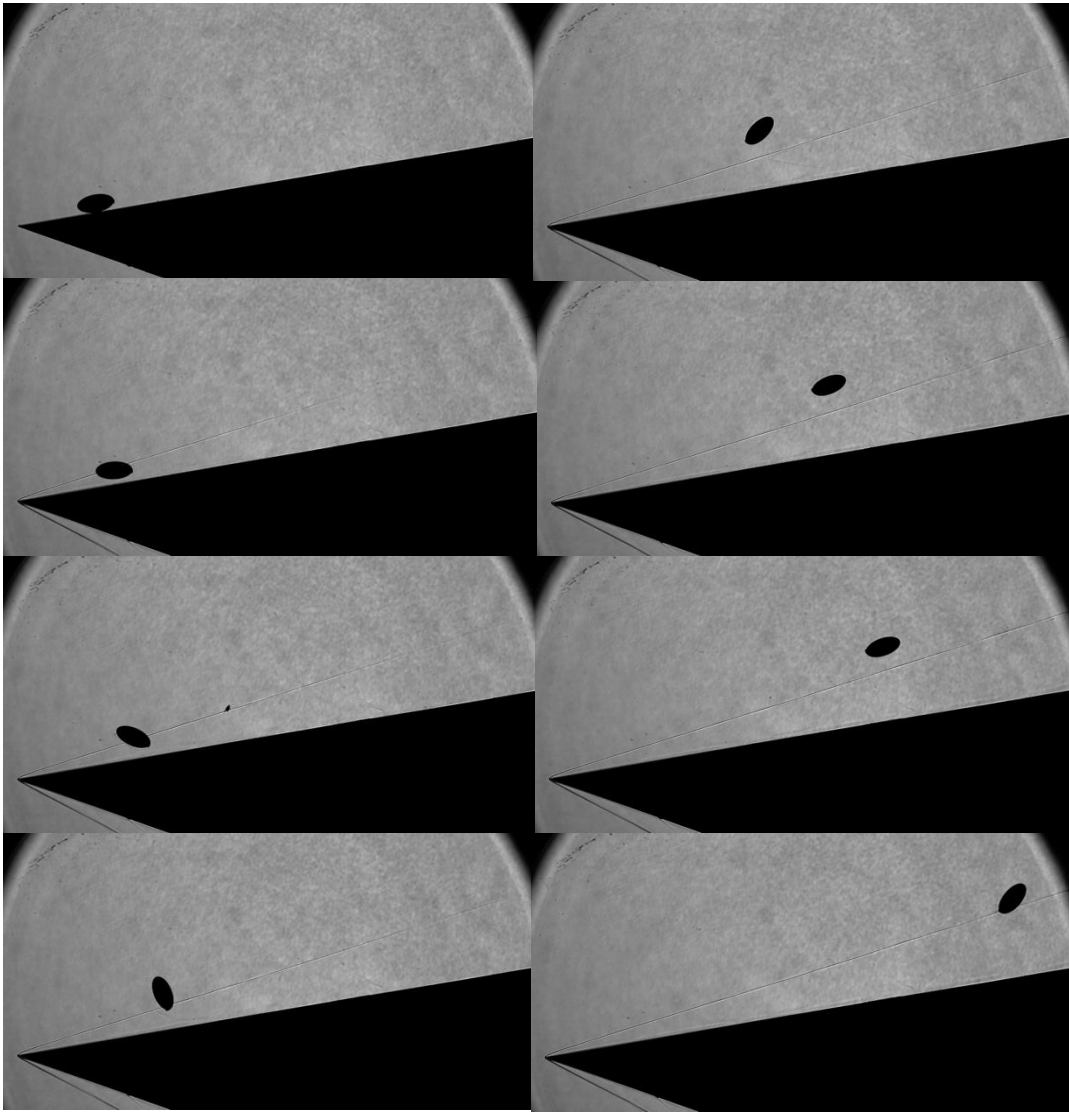


**Figure A1.7:** Shadowgraph images of Configuration E3

## A2: Displacement Analysis of Experimental Results

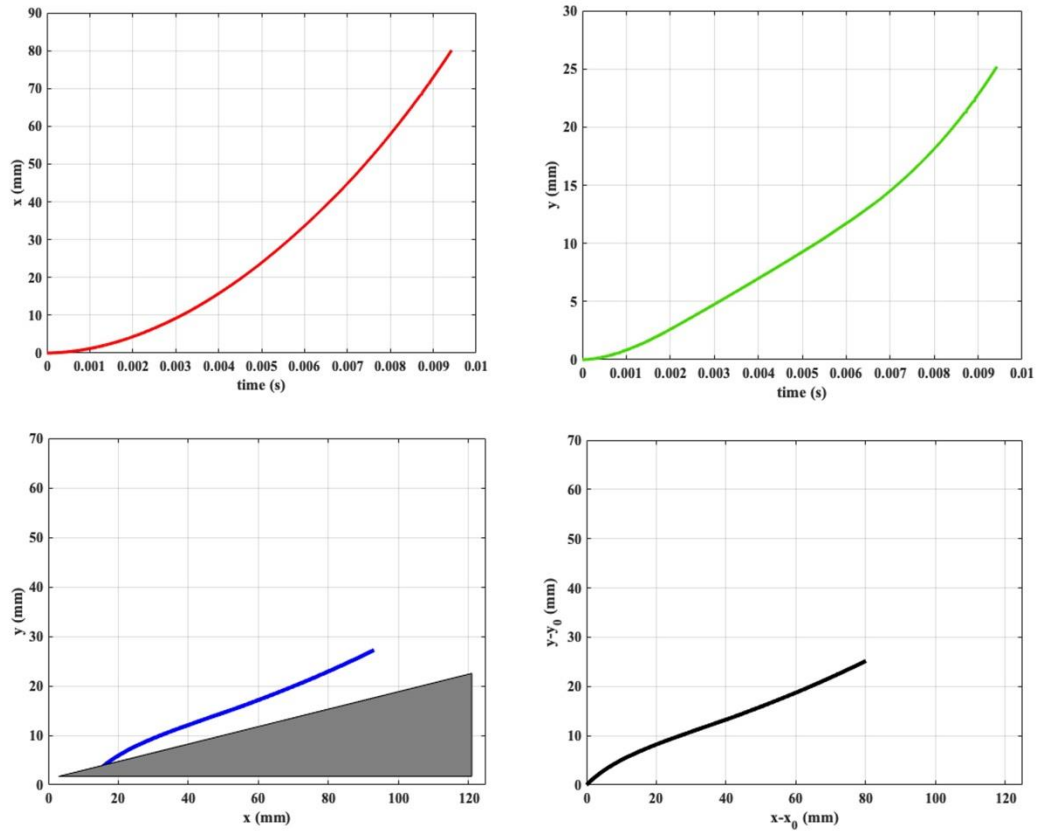


**Figure A2.1:** Horizontal Displacement (top left), Vertical Displacement (top right) of Configuration D1. Absolute (bottom left) and relative (bottom right)  $x$  versus  $y$  displacement of Configuration D1.

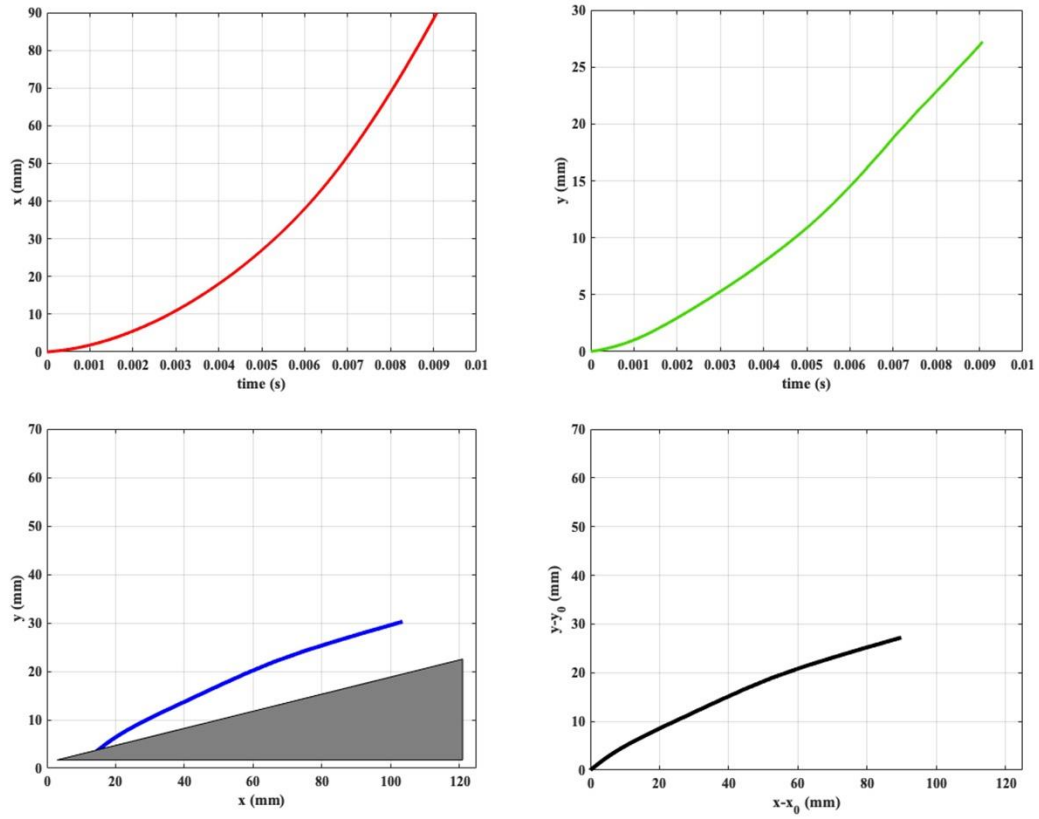


**Figure A2.2:** Horizontal Displacement (top left), Vertical Displacement (top right) of Configuration D2. Absolute (bottom left) and relative (bottom right)  $x$  versus  $y$  displacement of Configuration D2.

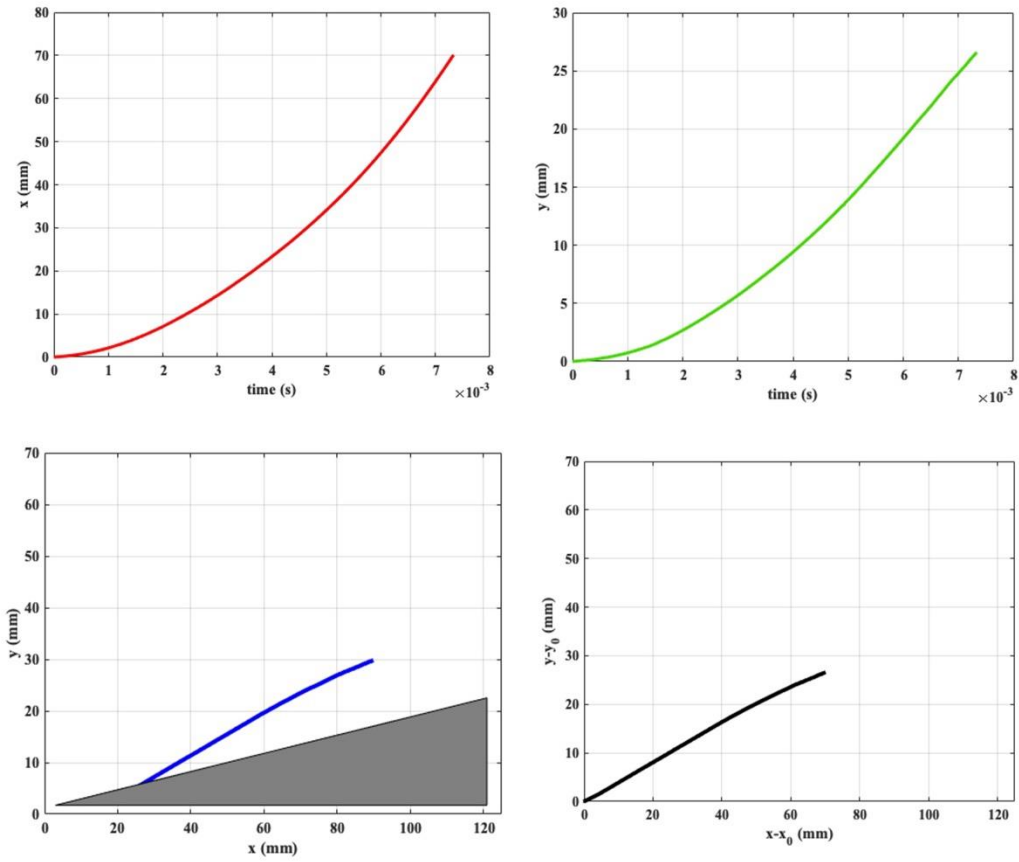


**Figure A2.3:** Horizontal Displacement (top left), Vertical Displacement (top right) of Configuration D3. Absolute (bottom left) and relative (bottom right)  $x$  versus  $y$  displacement of Configuration D3.

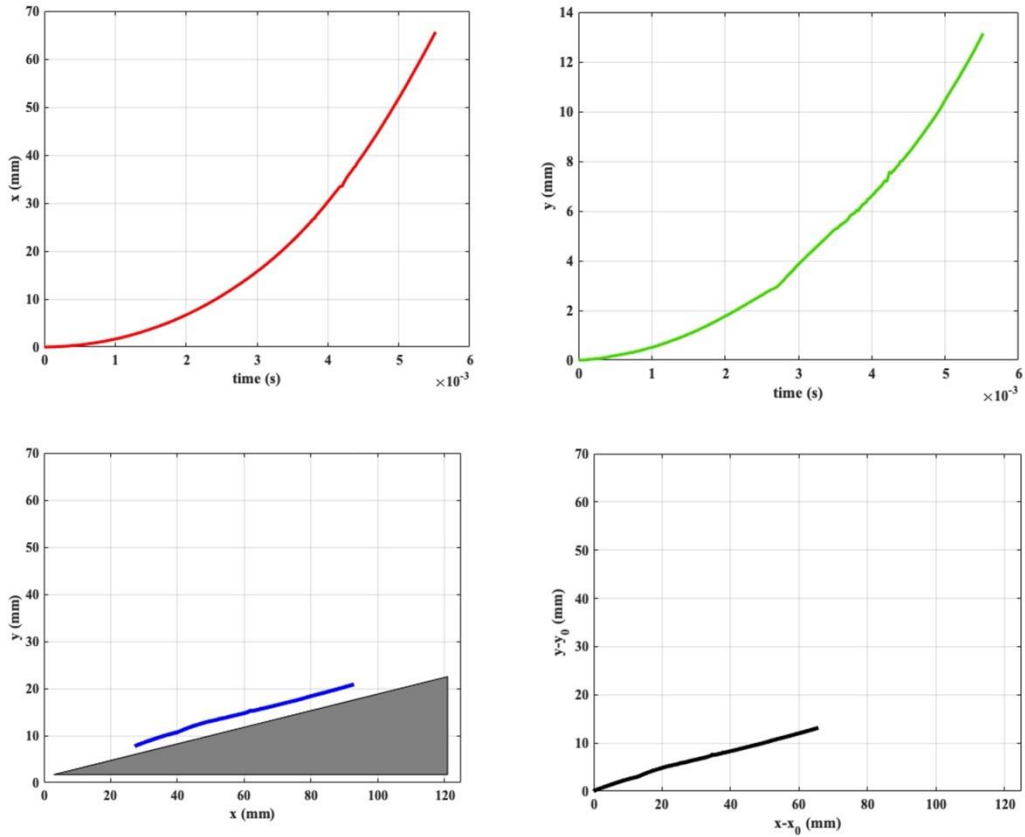


**Figure A2.4:** Horizontal Displacement (top left), Vertical Displacement (top right) of Configuration D4. Absolute (bottom left) and relative (bottom right)  $x$  versus  $y$  displacement of Configuration D4.

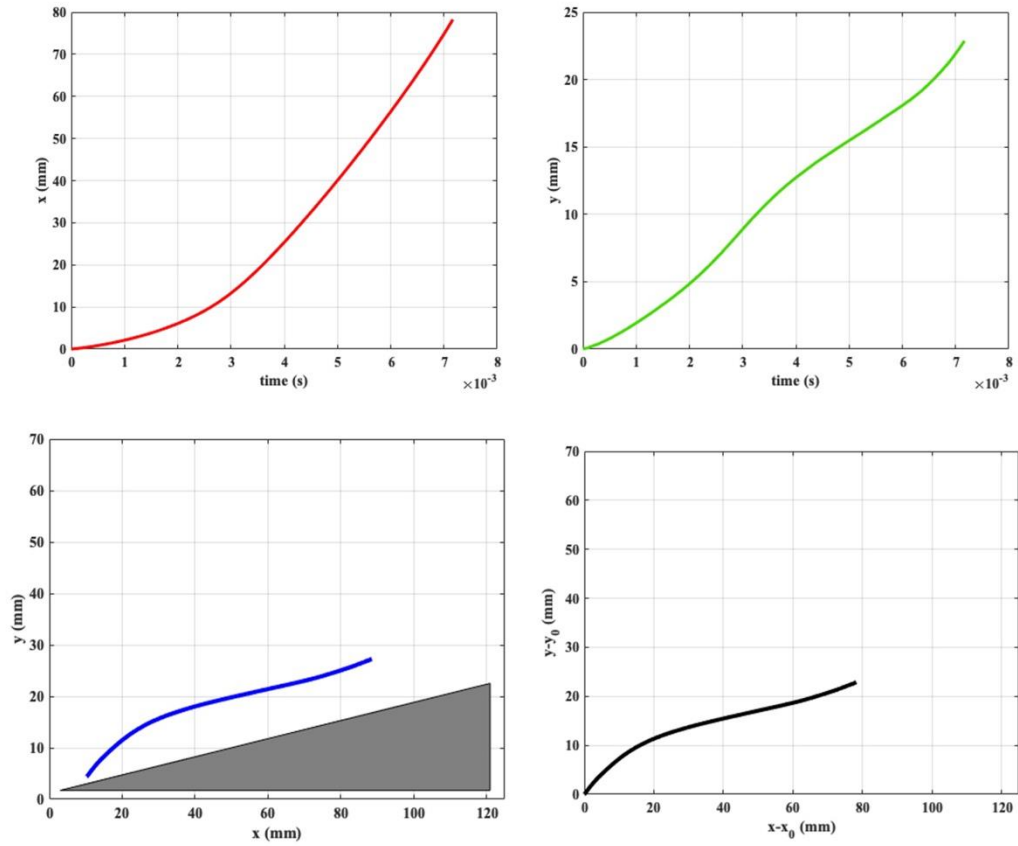


**Figure A2.5:** Horizontal Displacement (top left), Vertical Displacement (top right) of Configuration E1. Absolute (bottom left) and relative (bottom right)  $x$  versus  $y$  displacement of Configuration E1.

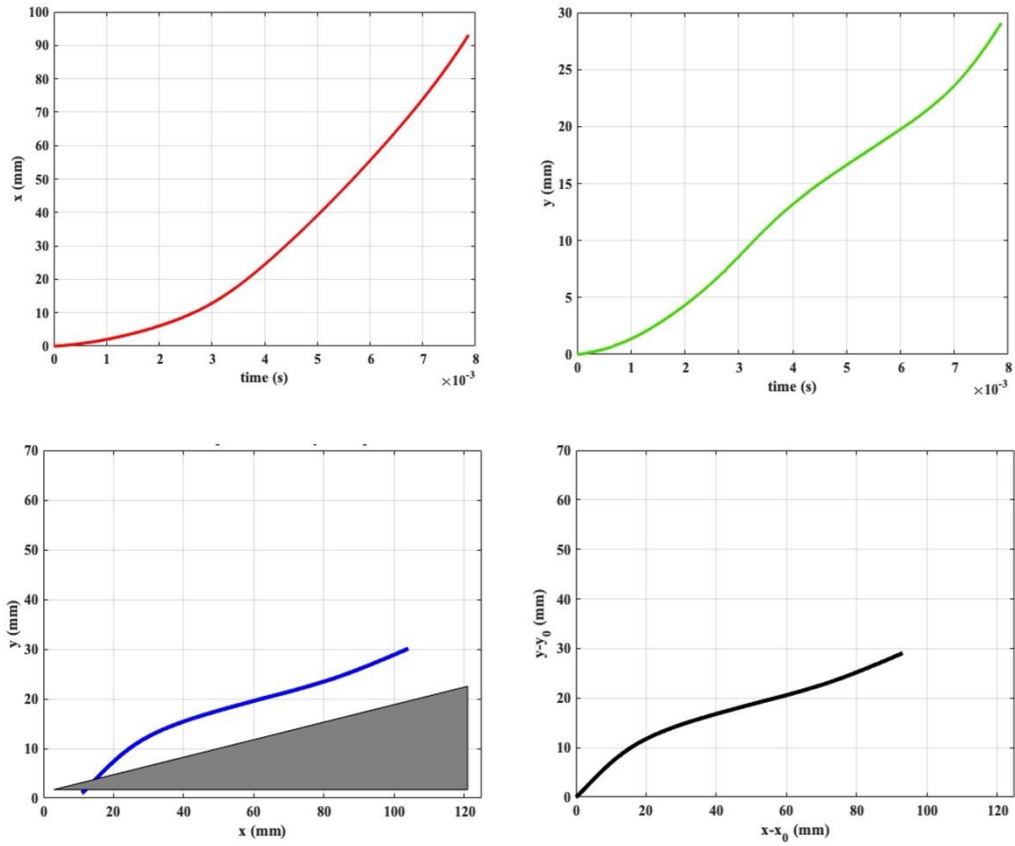


**Figure A2.6:** Horizontal Displacement (top left), Vertical Displacement (top right) of Configuration E2. Absolute (bottom left) and relative (bottom right)  $x$  versus  $y$  displacement of Configuration E2.

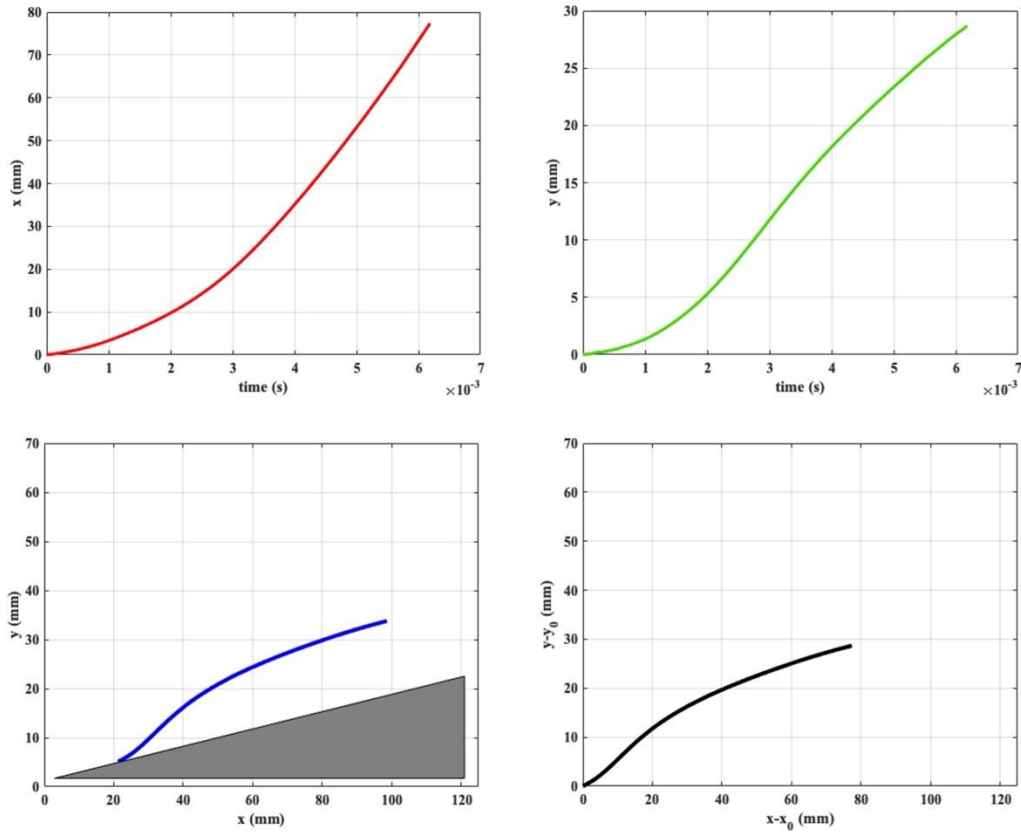


**Figure A2.7:** Horizontal Displacement (top left), Vertical Displacement (top right) of Configuration E3. Absolute (bottom left) and relative (bottom right)  $x$  versus  $y$  displacement of Configuration E3.

### A3: Hadamard Regularization Analysis of Velocity and Acceleration

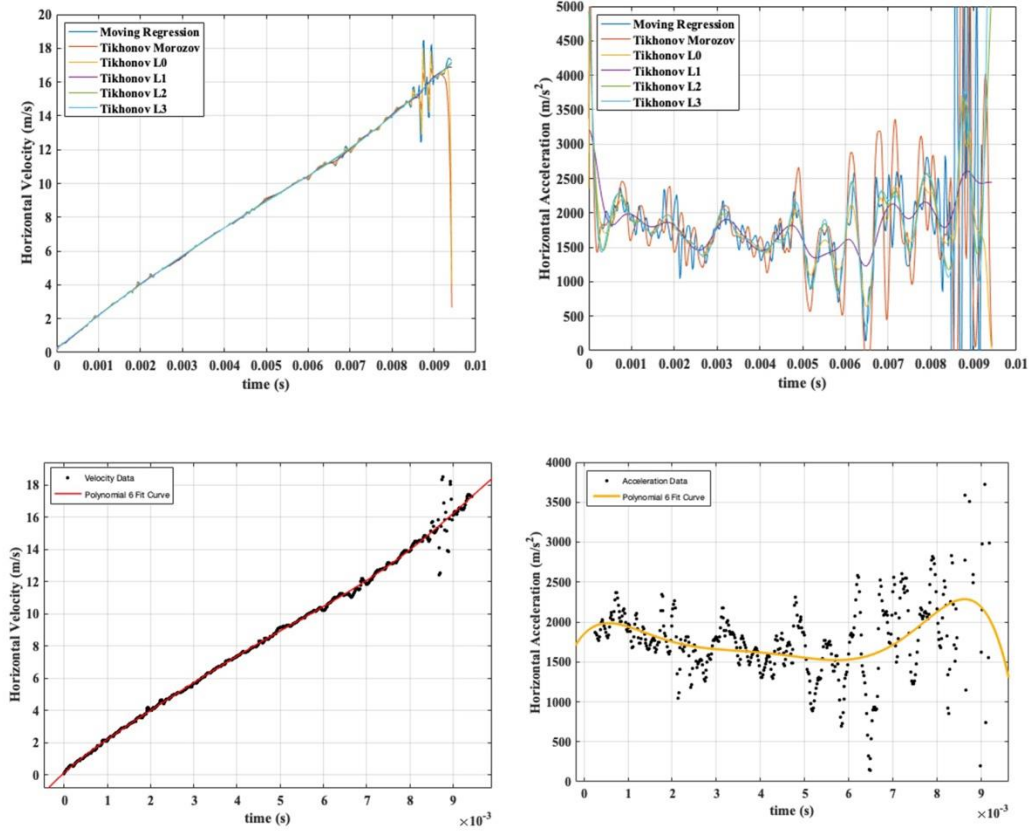


**Figure A3.1:** Horizontal Velocity (top left) and Horizontal Acceleration (top right) derived from Hadamard Regularization methods for Configuration D1. Polynomial 6 Fit Curve of Velocity (bottom left) and Acceleration (bottom right) data derived from Hadamard Regularization methods for Configuration D1.

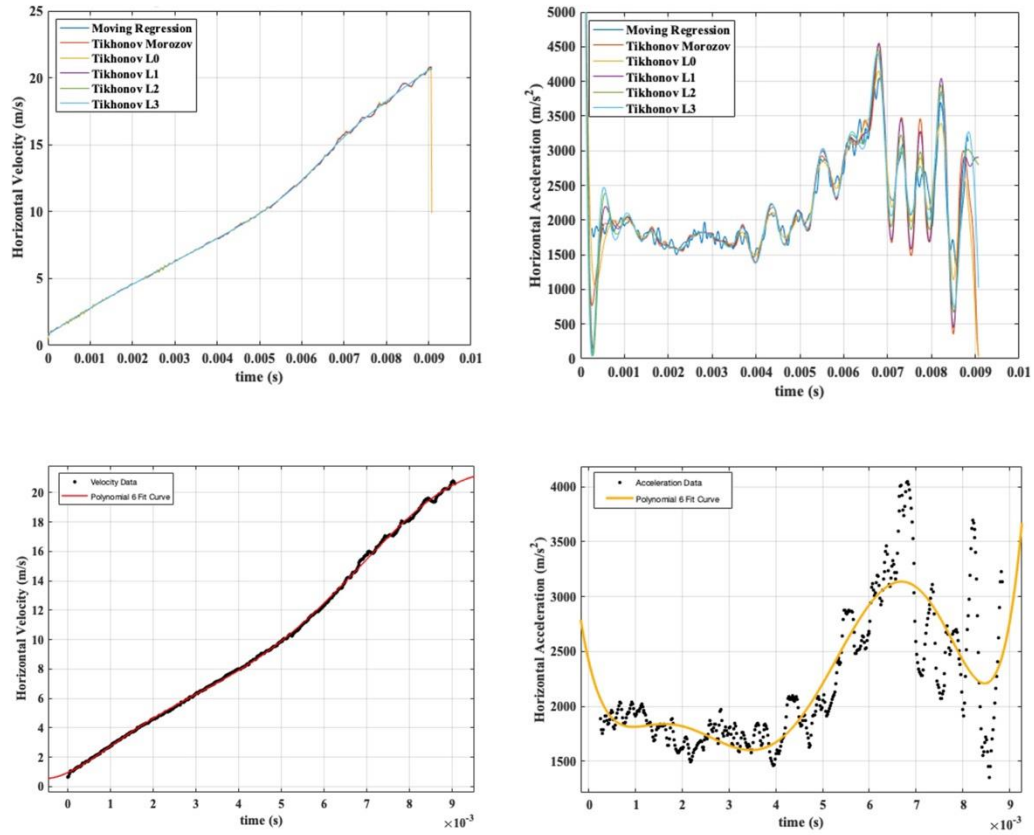


**Figure A3.2:** Horizontal Velocity (top left) and Horizontal Acceleration (top right) derived from Hadamard Regularization methods for Configuration D2. Polynomial 6 Fit Curve of Velocity (bottom left) and Acceleration (bottom right) data derived from Hadamard Regularization methods for Configuration D2.

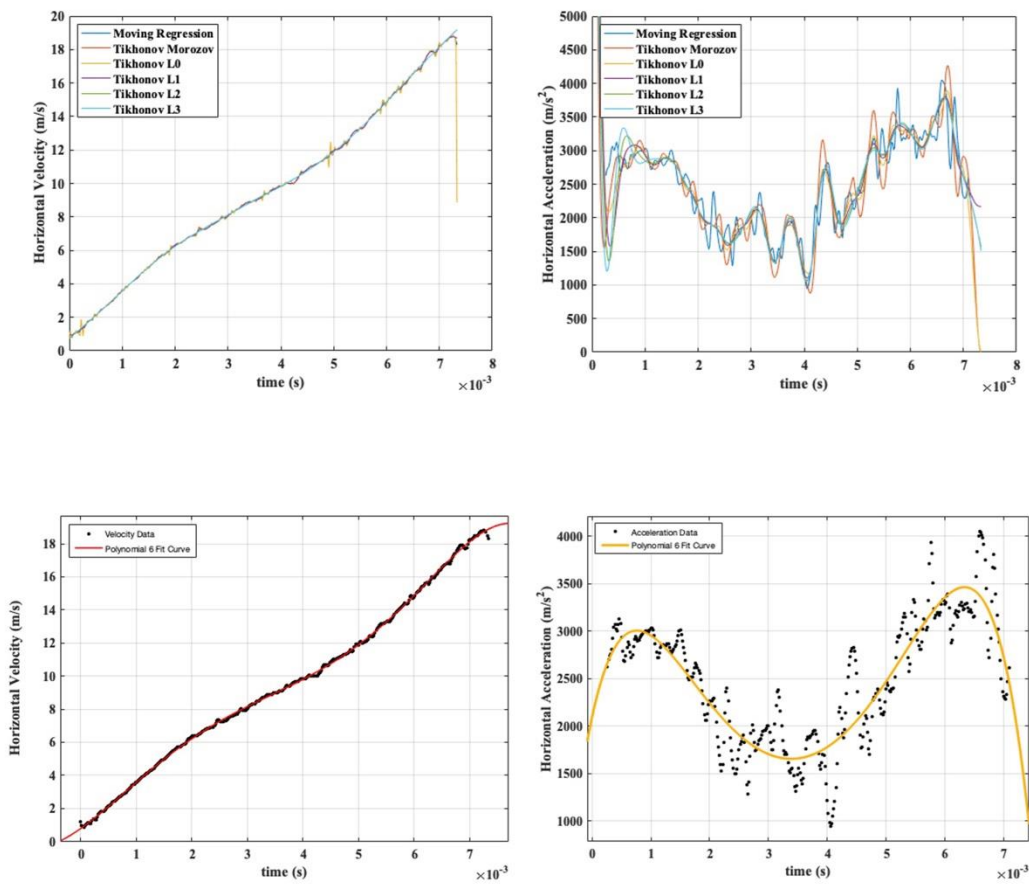


**Figure A3.3:** Horizontal Velocity (top left) and Horizontal Acceleration (top right) derived from Hadamard Regularization methods for Configuration D3. Polynomial 6 Fit Curve of Velocity (bottom left) and Acceleration (bottom right) data derived from Hadamard Regularization methods for Configuration D3.

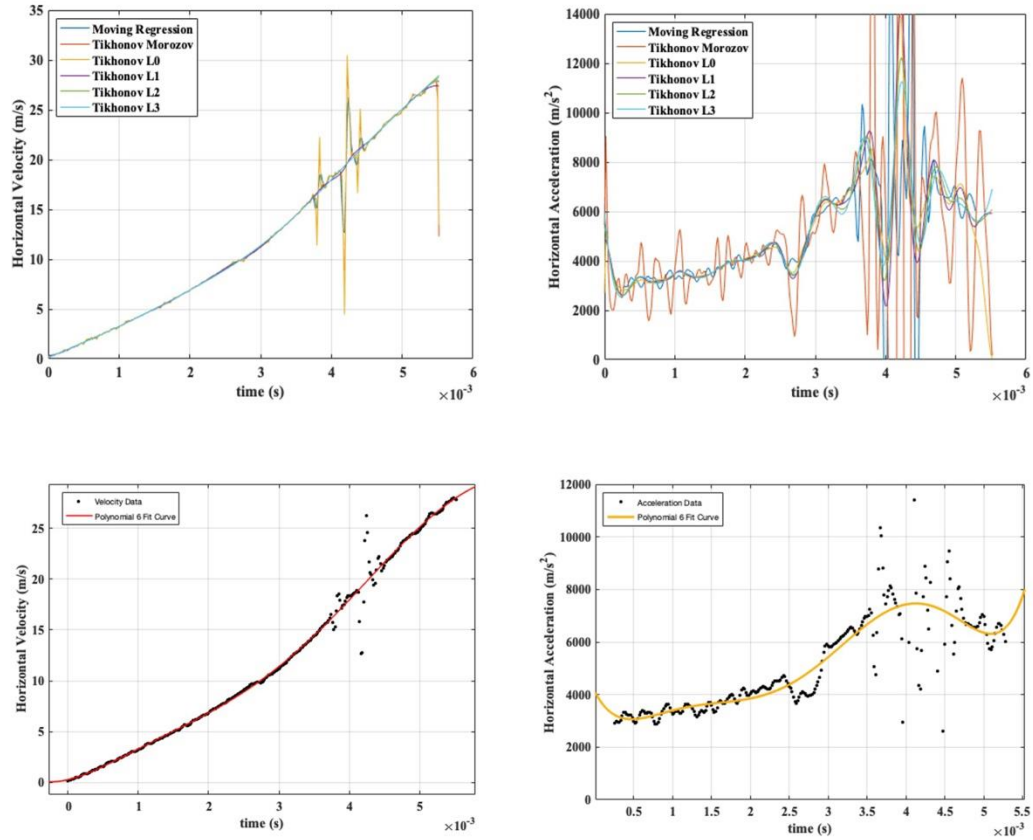


**Figure A3.4:** Horizontal Velocity (top left) and Horizontal Acceleration (top right) derived from Hadamard Regularization methods for Configuration D4. Polynomial 6 Fit Curve of Velocity (bottom left) and Acceleration (bottom right) data derived from Hadamard Regularization methods for Configuration D4.

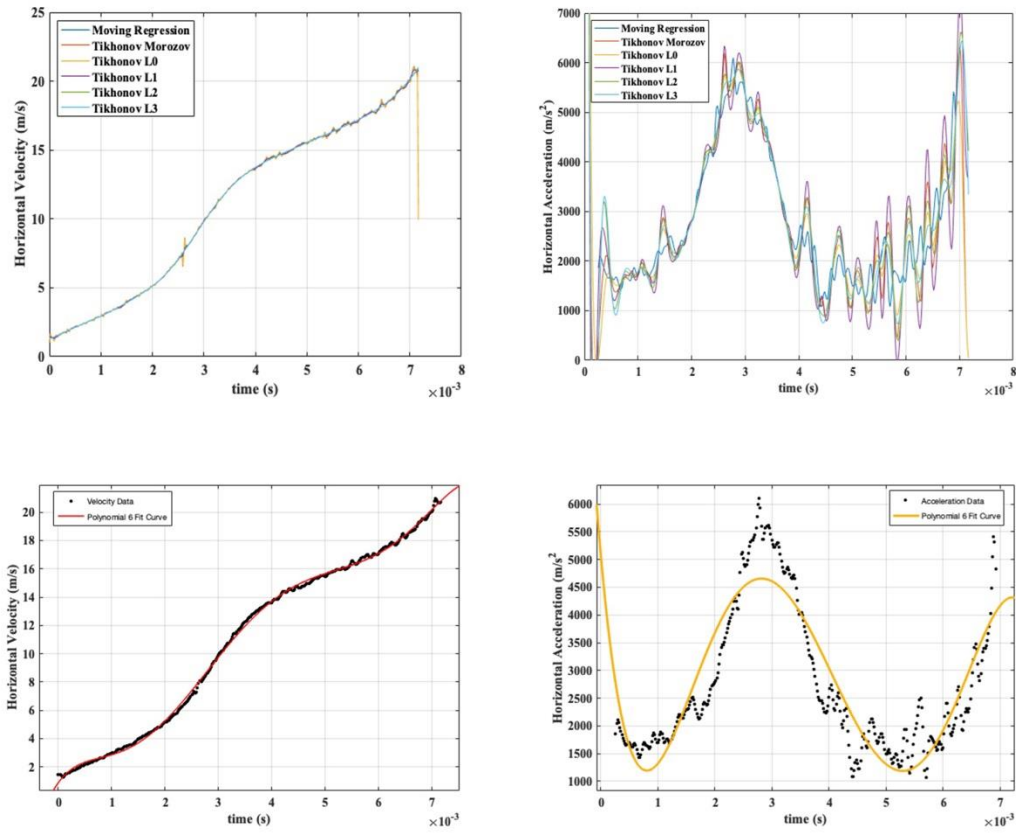


**Figure A3.5:** Horizontal Velocity (top left) and Horizontal Acceleration (top right) derived from Hadamard Regularization methods for Configuration E1. Polynomial 6 Fit Curve of Velocity (bottom left) and Acceleration (bottom right) data derived from Hadamard Regularization methods for Configuration E1.

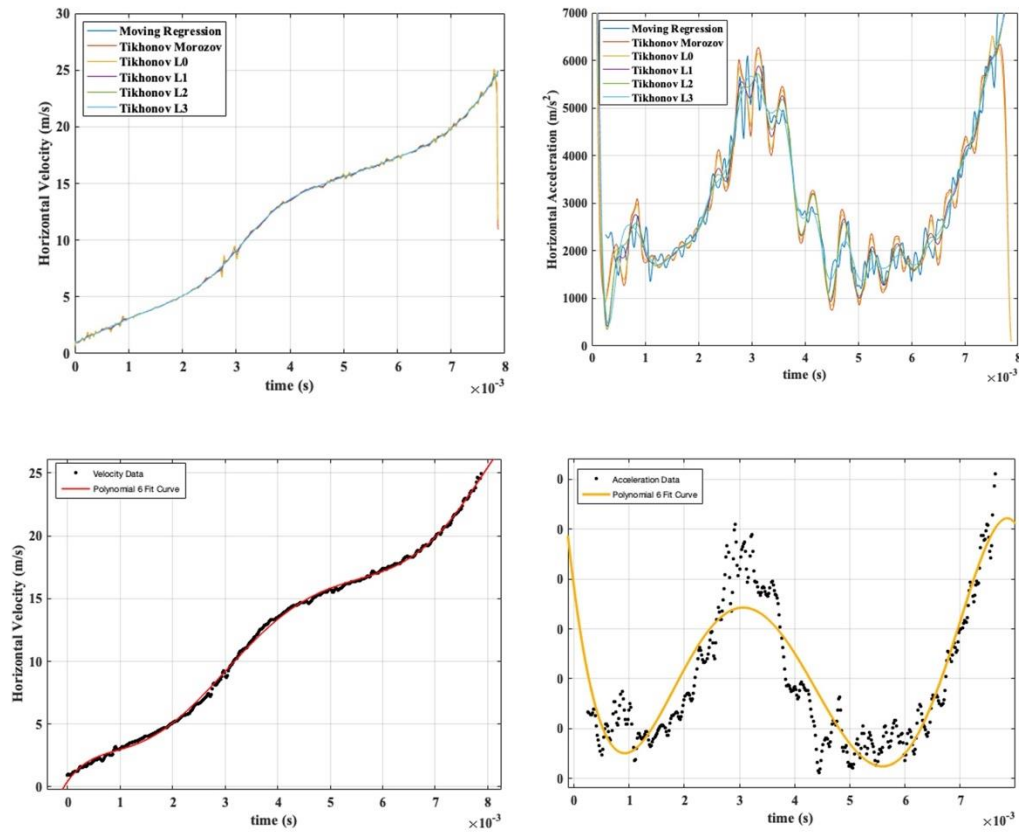


**Figure A3.6:** Horizontal Velocity (top left) and Horizontal Acceleration (top right) derived from Hadamard Regularization methods for Configuration E2. Polynomial 6 Fit Curve of Velocity (bottom left) and Acceleration (bottom right) data derived from Hadamard Regularization methods for Configuration E2.

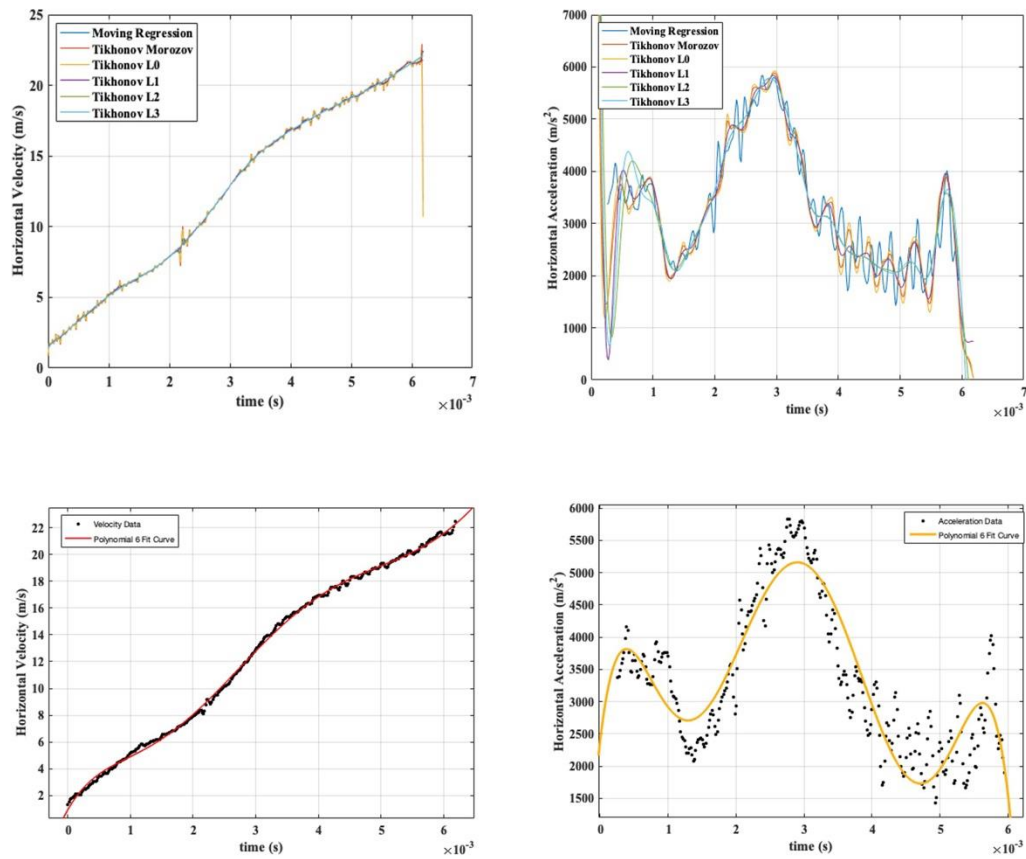


**Figure A3.7:** Horizontal Velocity (top left) and Horizontal Acceleration (top right) derived from Hadamard Regularization methods for Configuration E3. Polynomial 6 Fit Curve of Velocity (bottom left) and Acceleration (bottom right) data derived from Hadamard Regularization methods for Configuration E3.

## A4: Dynamics Results of Various Grid Level Refinement

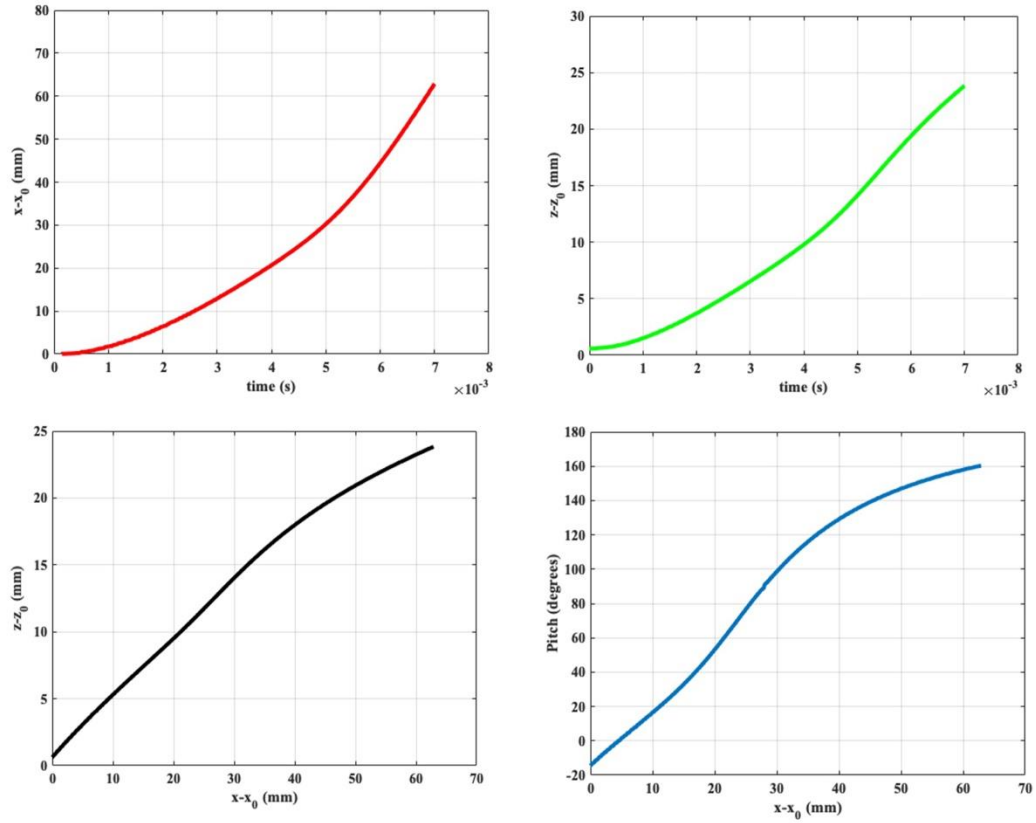


**Figure A4.1:** Computational data for Extra Coarse grid with 72000 iterations and a timestep of 1E-07. Relative horizontal displacement (top left) and Relative vertical displacement (top right). X vs Z displacement (bottom left) and Pitch (bottom right).

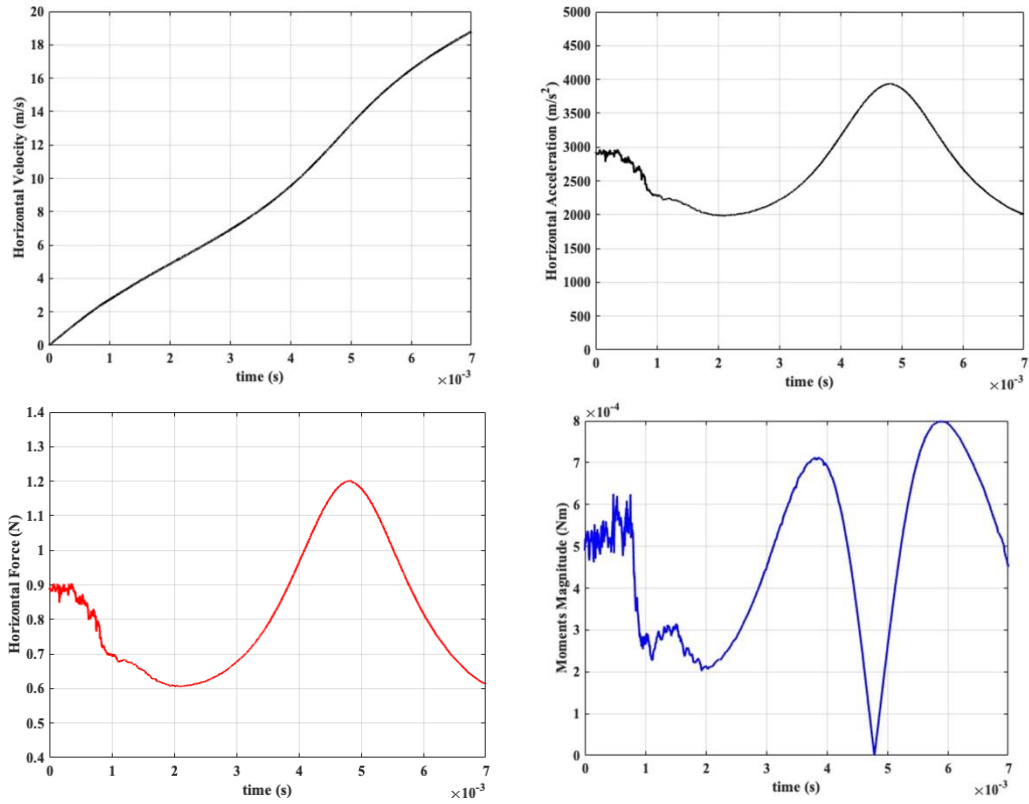


**Figure A4.2:** Computational data for Extra Coarse grid with 72000 iterations and a timestep of 1E-07. Horizontal velocity (top left) and horizontal acceleration (top right). Horizontal Forces (bottom left) and Moments magnitude (bottom right).

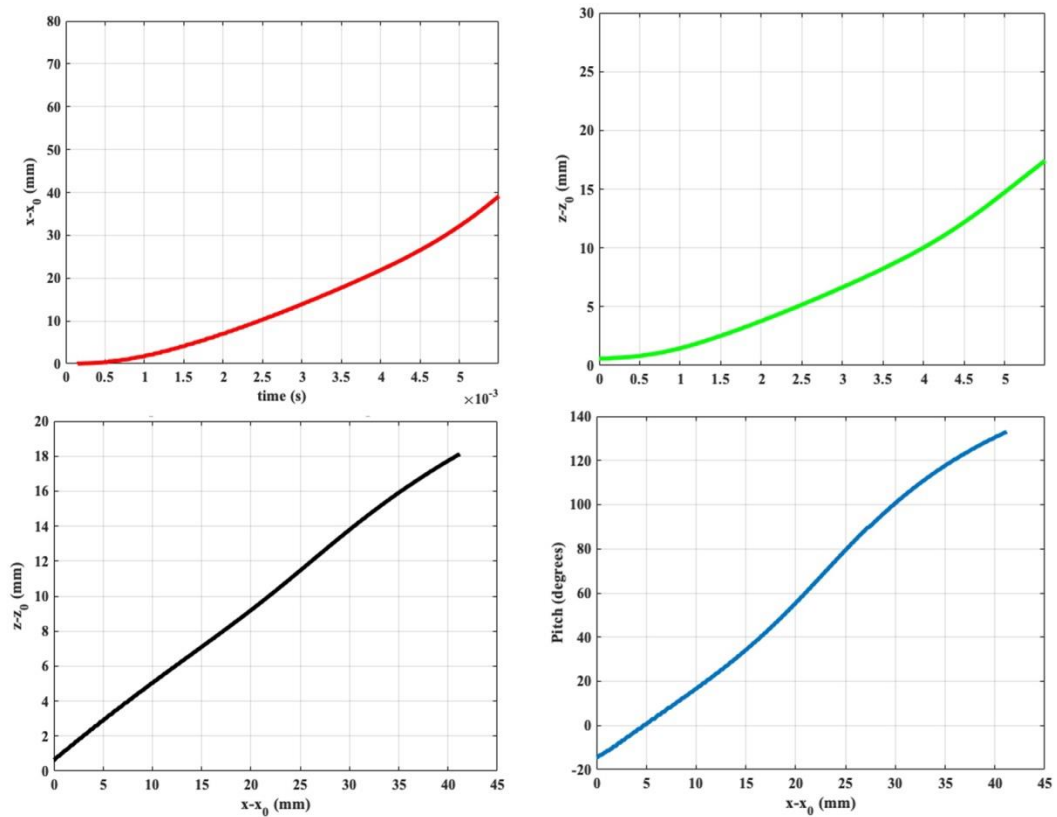


**Figure A4.3:** Computational data for Coarse grid with 53809 iterations and a timestep of 1E-07. Relative horizontal displacement (top left) and Relative vertical displacement (top right). X vs Z displacement (bottom left) and Pitch (bottom right).

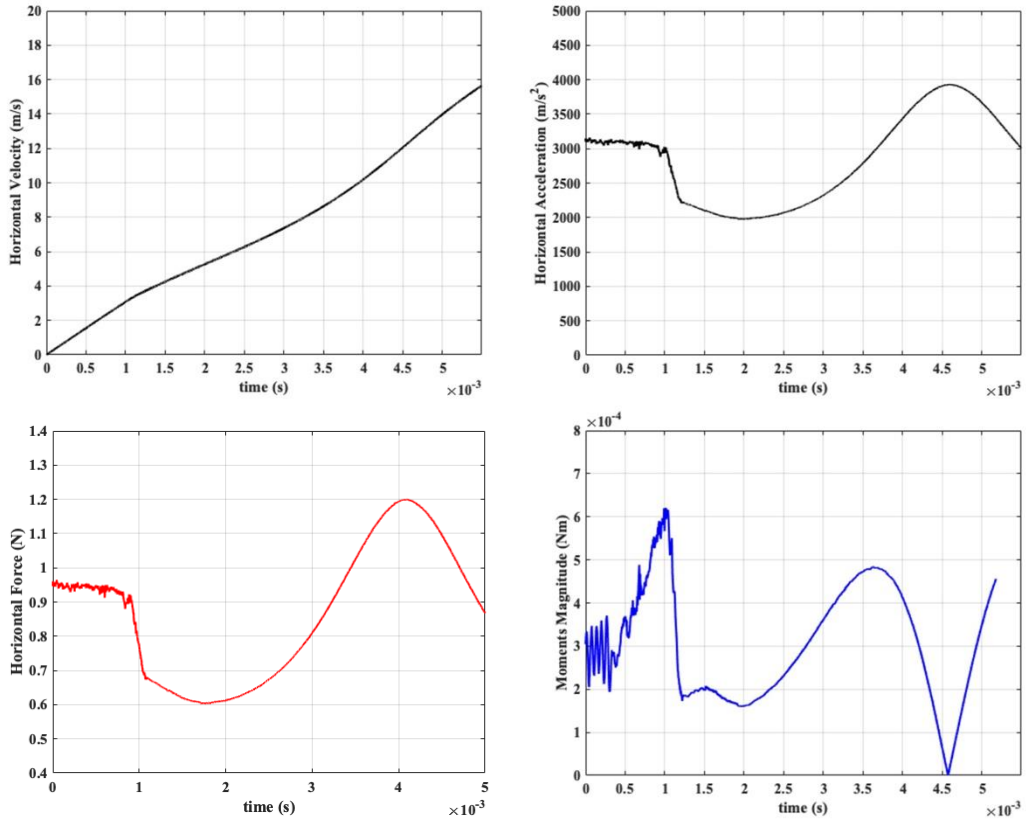


**Figure A4.4:** Computational data for Coarse grid with 53809 iterations and a timestep of 1E-07. Horizontal velocity (top left) and horizontal acceleration (top right). Horizontal Forces (bottom left) and Moments magnitude (bottom right).

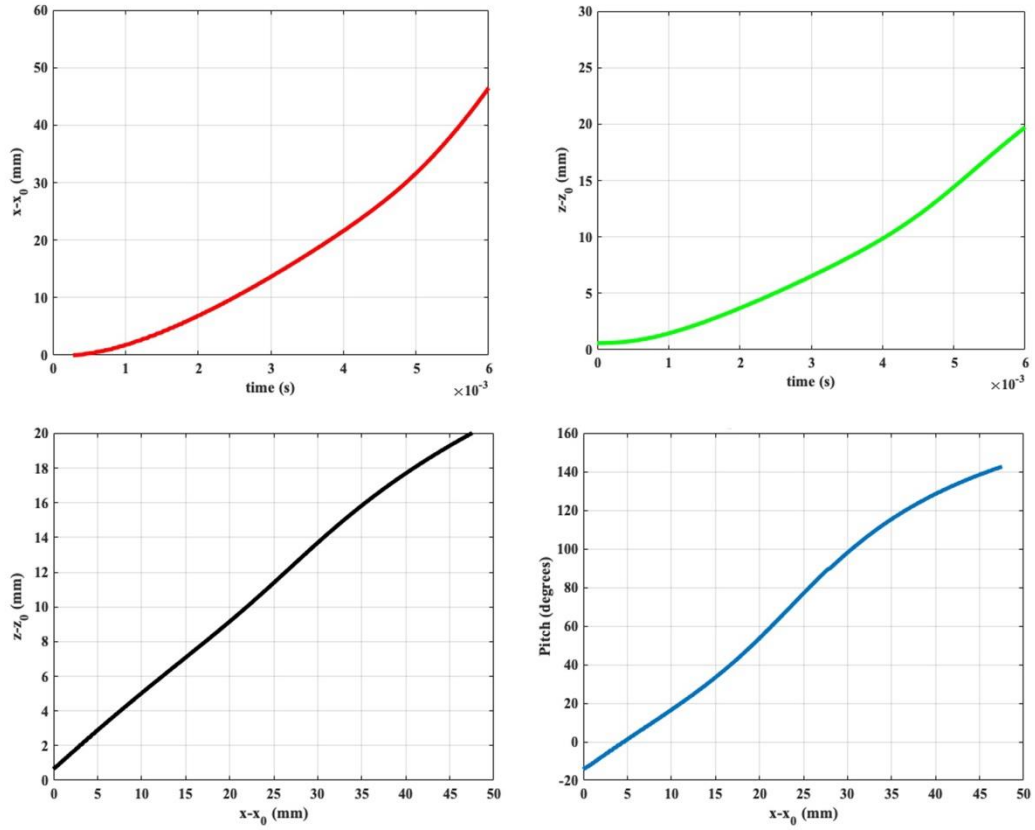


**Figure A4.5:** Computational data for Medium grid with 123294 iterations and a timestep of 5E-08. Relative horizontal displacement (top left) and Relative vertical displacement (top right). X vs Z displacement (bottom left) and Pitch (bottom right).

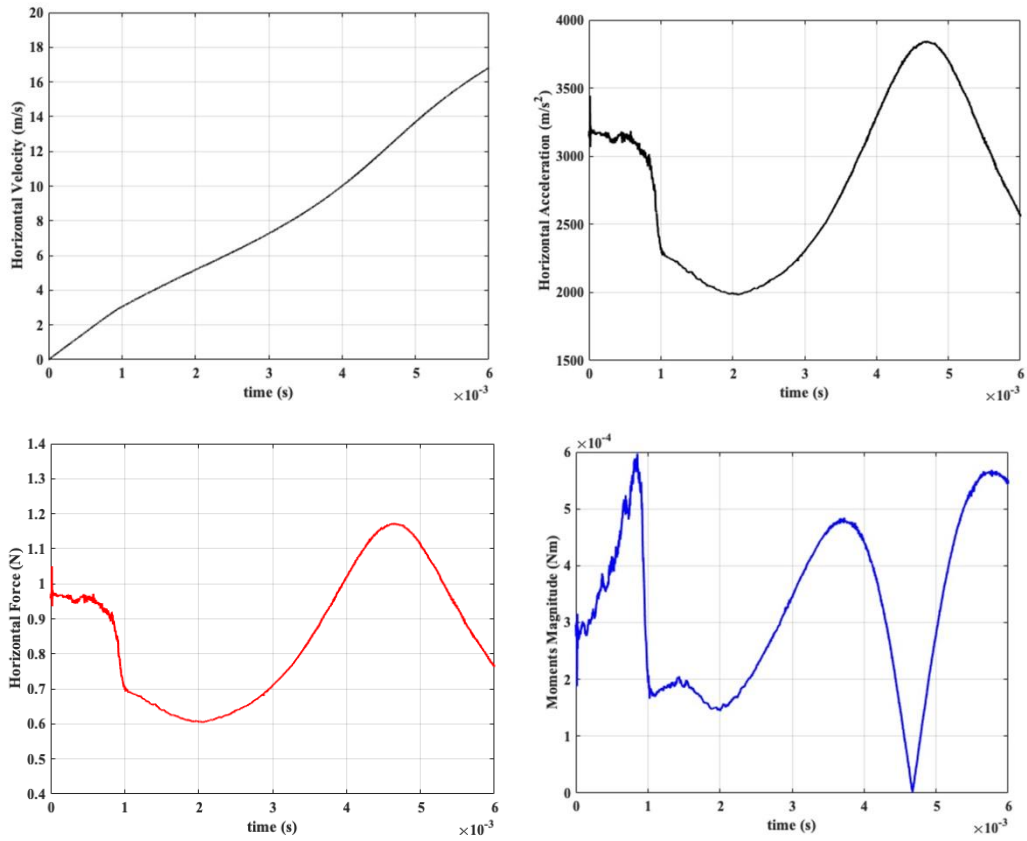


**Figure A4.6:** Computational data for Medium grid with 123294 iterations and a timestep of 5E-08. Horizontal velocity (top left) and horizontal acceleration (top right). Horizontal Forces (bottom left) and Moments magnitude (bottom right).

A5: Calculation of normalization variable  $r$

$$r = r_e \times S_A$$

Configuration	$r_e$ (mm)	$S_A$ (pixel/mm)	$r$ (pixels)
D1	7.5	7.5062	56.2965
D2	7.5	7.4533	55.8998
D3	7.5	7.4446	55.8345
D4	7.5	7.5257	55.4428
E1	6	7.4235	44.451
E2	6	7.4971	44.9826
E3	6	7.5230	45.1380

## Bibliography

- [1] A. Cenko, “Store Separation Lessons Learned Over the Last 30 Years.” International congress of the aeronautical sciences, 2010.
- [2] A. H. Shapiro, *The dynamics of thermodynamics of compressible fluid flow*. New York, NY: J. Wiley, 1976.
- [3] B. E. Edney, “Effects of shock impingement on the heat transfer around blunt bodies.,” *AIAA Journal*, vol. 6, no. 1, pp. 15–21, 1968.
- [4] C. Butler and S. J. Laurence, “HyperTERP: A newly commissioned Hypersonic Shock Tunnel at the University of Maryland,” *AIAA Aviation 2019 Forum*, 2019.
- [5] C. E. Sousa, R. Deiterding, and S. J. Laurence, “Dynamics of a spherical body shedding from a hypersonic ramp. part 1. Inviscid Flow,” *Journal of Fluid Mechanics*, vol. 906, 2020.
- [6] C. S. Butler, T. J. Whalen, C. E. Sousa, and S. J. Laurence, “Dynamics of a spherical body shedding from a hypersonic ramp. part 2. Viscous Flow,” *Journal of Fluid Mechanics*, vol. 906, 2020.
- [7] “Columbia Crew Survival Investigation Report.” NASA, Houston.
- [8] “Create-FT,” *Department of Defense High Performance Computing Modernization Program*. [Online]. Available: <https://centers.hpc.mil/CREATE/CREATE-FT.html>. [Accessed: 15-Sep-2022].
- [9] D. J. Munk, D. Verstraete, and G. A. Vio, “Effect of fluid-thermal-structural interactions on the topology optimization of a hypersonic transport aircraft wing,” *Journal of Fluids and Structures*, vol. 75, pp. 45–76, 2017.
- [10] D. Jeyakumar, K. K. Biswas, and B. Nageswara Rao, “Stage separation dynamic analysis of upper stage of a multistage launch vehicle using Retro Rockets,” *Mathematical and Computer Modelling*, vol. 41, no. 8-9, pp. 849–866, 2005.
- [11] E. Camarena, “Computational Fluid Dynamics Demonstration of Rigid Bodies in Motion.” NASA, 12-Aug-2011.
- [12] F. M. White, *Viscous Fluid Flow*. New York, NY: McGraw-Hill, 2006.
- [13] G. S. Settles, “Shadowgraph techniques,” *Schlieren and Shadowgraph Techniques*, pp. 143–163, 2001.
- [14] HPCMP CREATE-AV, “Capstone Geometry Creation,” 2022.
- [15] HPCMP CREATE-AV, “Capstone Meshing Practice,” 2022.

- [16] HPCMP CREATE-AV, “Capstone Overview,” 2022.
- [17] HPCMP CREATE-AV, “Kestrel Single Body Near-Body/Off-Body.” 2022.
- [18] HPCMP CREATE-AV, “Kestrel Store Separation Near-Body/Off-Body,” 2022.
- [19] HPCMP CREATE-AV, “Kestrel User Guide.” Department of Defense, Lorton, 2021.
- [20] J. Baeder, “CFD II Gridding Concepts and Transformation of Curvilinear Coordinates,” 2021.
- [21] J. Baeder, “CFD II Gridding Introduction,” 2021.
- [22] J. D. Anderson, *Fundamentals of aerodynamics*. New York, NY: McGraw-Hill, 2016.
- [23] J. D. Anderson, *Hypersonic and high-temperature gas dynamics*. Reston, VA: American Institute of Aeronautics and Astronautics, Inc., 2019.
- [24] J. D. Anderson, *Modern compressible flow: With historical perspective*. New York, NY: McGraw Hill, 2021.
- [25] J. Canny, “A Computational Approach to Edge Detection,” *Readings in Computer Vision*, pp. 184–203, 1987.
- [26] M. J. Robinson, D. J. Mee, and A. Paull, “Scramjet lift, thrust and pitching-moment characteristics measured in a shock tunnel,” *Journal of Propulsion and Power*, vol. 22, no. 1, pp. 85–95, 2006.
- [27] Q. R. Passey and H. J. Melosh, “Effects of Atmospheric Breakup on Crater Field Formation,” *Icarus*, vol. 42, no. 2, pp. 211–233, 1980.
- [28] R. Borker, D. Huang, S. Grimberg, C. Farhat, P. Avery, and J. Rabinovitch, “Mesh Adaptation Framework for embedded boundary methods for computational fluid dynamics and fluid-structure interaction,” *International Journal for Numerical Methods in Fluids*, vol. 90, no. 8, pp. 389–424, 2019.
- [29] R. Deiterding, “block-structured adaptive mesh refinement - theory, implementation and application,” *ESAIM: Proceedings*, vol. 34, pp. 97–150, 2011.
- [30] S. J. Laurence and H. G. Hornung, “Image-based force and moment measurement in hypersonic facilities,” *Experiments in Fluids*, vol. 46, no. 2, pp. 343–353, 2008.

- [31] S. J. Laurence and R. Deiterding, “Shock-wave surfing,” *Journal of Fluid Mechanics*, vol. 676, pp. 396–431, 2011.
- [32] S. J. Laurence and S. Karl, “An improved visualization-based force-measurement technique for short-duration hypersonic facilities,” *Experiments in Fluids*, vol. 48, no. 6, pp. 949–965, 2009.
- [33] S. J. Laurence, C. Sousa, C. Butler, and R. Deiterding, “Separation dynamics of a spherical particle detaching from a two-dimensional ramp in hypersonic flow,” *AIAA Aviation 2019 Forum*, 2019.
- [34] S. J. Laurence, N. J. Parziale, and R. Deiterding, “Dynamical separation of spherical bodies in supersonic flow,” *Journal of Fluid Mechanics*, vol. 713, pp. 159–182, 2012.
- [35] S. J. Laurence, “On tracking the motion of rigid bodies through edge detection and least-squares fitting,” *Experiments in Fluids*, vol. 52, no. 2, pp. 387–401, 2011.
- [36] S. J. Laurence, R. Deiterding, and G. Hornung, “Proximal bodies in hypersonic flow,” *Journal of Fluid Mechanics*, vol. 590, pp. 209–237, 2007.
- [37] T. J. Whalen and S. J. Laurence, “Experiments on the separation of sphere clusters in hypersonic flow,” *Experiments in Fluids*, vol. 62, no. 4, 2021.
- [38] T. J. Whalen, “Aerodynamic Separation of Fragmented Bodies in High-Speed flow,” dissertation, University of Maryland, College Park, MD, 2021.
- [39] W. C. Starshak and S. J. Laurence, “Computer-Graphics-based optical tracking for hypersonic free-flight experiments,” *AIAA Journal*, vol. 59, no. 12, pp. 4955–4968, 2021.
- [40] W. C. Starshak and S. J. Laurence, “Optical free-flight measurements using GPU-Accelerated Computer Graphics,” *22nd AIAA International Space Planes and Hypersonics Systems and Technologies Conference*, 2018.
- [41] W. Zhu and S. Laurence, “Evaluation of Methods for Recovering Unsteady Forces from Free-Flight Optical Measurements in Hypersonic Facilities,” 2022.